Draft version December 7, 2017
Preprint typeset using LaTeX style AASTeX6 v. 1.0

PULSAR ROTATION MEASURES AND LARGE-SCALE MAGNETIC FIELD REVERSALS IN THE GALACTIC DISK

J. L. Han[1], R. N. Manchester[2], W. van Straten[3], and P. Demorest[4]

[1]National Astronomical Observatories, Chinese Academy of Sciences, Jia 20 DaTun Road, Beijing 100012, China. Email: hjl@bao.ac.cn
[2]CSIRO Astronomy and Space Science, PO Box 76, Epping, NSW 1710, Australia. Email: dick.manchester@csiro.au
[3]Institute for Radio Astronomy and Space Research, Auckland University of Technology, PB 92006, Auckland 1142, New Zealand
[4]National Radio Astronomy Observatory, PO Box O, Socorro, NM 87801, USA

ABSTRACT

We present the measurements of Faraday rotation for 477 pulsars observed by the Parkes 64-m radio telescope and the Green Bank 100-m radio telescope. Using these results along with previous measurements for pulsars and extra-galactic sources, we analyse the structure of the large-scale magnetic field in the Galactic disk. Comparison of rotation measures of pulsars in the disk at different distances as well as with rotation measures of background radio sources beyond the disk reveals large-scale reversals of the field directions between spiral arms and interarm regions. We develop a model for the disk magnetic field, which can reproduce not only these reversals but also the distribution of observed rotation measures of background sources.

1. INTRODUCTION

Interstellar magnetic fields of our Galaxy have long been known to play fundamental roles in astrophysics and astroparticle physics, and their properties have been investigated for many years. A Galactic magnetic field was proposed by Fermi (1949) as the agent for transport of cosmic rays through interstellar space and, shortly afterward, Kiepenheuer (1950) proposed a synchrotron origin for the Galactic background of radio emission. Remarkably, both Fermi and Kiepenheuer calculated the strength of the interstellar field to be of order a few μG, very close to current estimates. Magnetic fields contribute significantly to the interstellar hydrodynamic pressure (Boulares & Cox 1990) and may even be dynamically important in the outer parts of some galaxies (Battaner & Florido 2007). The strong magnetic fields found in molecular clouds are key to understanding the star-formation process (Rees 1987). Understanding the structure of the Galactic magnetic field is also important to understanding the origin and maintenance of magnetic fields in other galaxies and in intergalactic space (Beck et al. 1996). For a recent review of Galactic and extragalactic magnetic field observations see Han (2017).

Several tracers have been used to investigate interstellar magnetic fields, including starlight polarization (e.g., Heiles 1996; Clemens et al. 2012), Zeeman splitting of spectral lines of HI and various molecules (e.g., Crutcher 1999; Vlemmings 2008), background synchrotron radiation from our Galaxy (e.g., Beuermann et al. 1985; Bennett et al. 2013; Planck Collaboration et al. 2016a), polarized thermal emission from dust grains in molecular clouds (e.g., Novak et al. 2003; Planck Collaboration et al. 2016b) and Faraday rotation of extragalactic radio sources (EGRS) (Simard-Normandin & Kronberg 1980; Taylor et al. 2009) and of pulsars (Manchester 1972; Rand & Lyne 1994; Han et al. 1999; Han et al. 2006; Noutsos et al. 2008). These and similar observations have shown that the large-scale magnetic field in galactic disks is largely toroidal and aligned with spiral arm structures, whereas halo fields probably have azimuthal fields with reversed directions above and below the Galactic plane (Han et al. 1997; Han et al. 1999) though the field scale-height and scale-radius are not yet known. Polarisation observations of synchrotron emission from nearby galaxies suggest that large-scale magnetic fields in galactic disks are predominantly spiral with roughly the same pitch angle both within spiral arms and in interarm regions (e.g. Beck 2015).

Pulsars are very effective probes of the magnetic field of our Galaxy (Manchester 1974; Lyne & Smith 1989; Rand & Kulkarni 1989; Weisberg et al. 2004; Han et al. 2006). They are highly polarized, have no intrinsic Faraday rotation and are widely distributed throughout the Galaxy at approximately known distances, allowing a three-dimensional tomographic analysis of the field structure. Furthermore, the pulse dispersion gives a unique calibration

of the integrated electron density along the line of sight, allowing a direct estimate of the strength of the field:

$$\langle B_{||} \rangle = \frac{\int_0^D n_e \mathbf{B}.d\mathbf{l}}{\int_0^D n_e dl} = 1.232 \frac{\mathrm{RM}}{\mathrm{DM}}, \quad (1)$$

where $\langle B_{||} \rangle$ is the mean line-of-sight magnetic field component in μG, weighted by the local electron density n_e, D is the pulsar distance and RM and DM are respectively the pulsar rotation measure and dispersion measure in their usual units (rad m^{-2} and cm^{-3} pc). By using pairs of pulsars that are close together on the sky and at distances D_1 and D_2 respectively, the mean line-of-sight field component between D_1 and D_2 can be obtained from:

$$\langle B_{||} \rangle_{D_2 - D_1} = 1.232 \frac{\mathrm{RM}_2 - \mathrm{RM}_1}{\mathrm{DM}_2 - \mathrm{DM}_1}. \quad (2)$$

This relation allows analysis of changes in the magnetic field along a given line of sight and hence full tomographic mapping of the Galactic magnetic field. Beck et al. (2003) argued that correlated or anti-correlated electron density with field strength will strongly bias estimates of $B_{||}$, but detailed simulations by Wu et al. (2009, 2015) show this not to be a problem, although the uncertainty of estimated mean field strengths depends on the Mach number of the interstellar medium.

In addition to the field strength, the field directions and their reversals are crucial to the understanding of the structure of Galactic large-scale magnetic fields. Many authors have proposed models for the large-scale structure of the Galactic magnetic field. Based on the RMs of 38 relatively nearby pulsars, Manchester (1974) concluded that the local Galactic magnetic field is basically azimuthal and directed toward longitude $l \sim 90°$, that is, clockwise when viewed from the Galactic North Pole. Thomson & Nelson (1980) analyzed RMs of 48 pulsars and found evidence for a field reversal in the inner Carina-Sagittarius arm. After a large number of pulsar RMs were obtained by Hamilton & Lyne (1987), Lyne & Smith (1989) confirmed the first inner reversal and suggested another reversal in the outer Galaxy. Rand & Kulkarni (1989) and Rand & Lyne (1994) fitted concentric ring models to the pulsar RM data with alternating field directions in each ring. Based on more than 350 pulsar RMs, Vallée (2005) revised the ring model to have a dominant clockwise ring field with just one ring of counter-clockwise field in the Galactocentric radius range 5 – 7 kpc. Earlier, both an axisymmetric spiral (ASS) model (Vallée 1996) and a bisymmetric spiral (BSS) model in which alternate arms have oppositely directed fields (Han & Qiao 1994; Indrani & Deshpande 1999; Han et al. 1999) for the global disk magnetic field were suggested, but more recent pulsar RM data do not favour this interpretation (Men et al. 2008). Noutsos et al. (2008) attempted to fit more complex bisymmetric three-dimensional models to pulsar RM data, but the results were inconclusive with none of the tested models giving a good fit to the data.

Radio continuum surveys have enabled measurement of RMs for thousands of EGRS (Taylor et al. 2009), and many authors have used these RMs to constrain models for the large-scale structure of the Galactic magnetic field. Some modelling (Simard-Normandin & Kronberg 1980; Sofue & Fujimoto 1983; Pshirkov et al. 2011) favoured a bisymmetric model for the disk field but with only one or two identified field reversals. Most recent models (Brown et al. 2007; Sun et al. 2008; Sun & Reich 2010; Van Eck et al. 2011; Jansson & Farrar 2012) with the benefit of a larger sample of EGRS RMs (Brown et al. 2003; Van Eck et al. 2011) are dominated by a general clockwise field but with counterclockwise fields in the Sagittarius/Scutum – Crux spiral zone. Recently, Ordog et al. (2017) used both EGRS and Galactic continuum background data to suggest that the outer boundary of this spiral zone is not perpendicular to the Galactic plane but is sloping toward later longitudes at positive latitudes and earlier longitudes at negative latitudes.

RMs for EGRS are of course integrated along the entire ray path through the Galaxy. They are therefore less sensitive to reversals in the Galactic field direction than pulsars which are distributed throughout the Galaxy. Also EGRS have an intrinsic RM component from Faraday rotation in the host galaxy and also a possible intergalactic component. In analyses of EGRS RMs, these components are generally assumed to be random, just adding to the fluctuations from small-scale variations in the Galactic magnetic field.

Using pulsar RMs, Han et al. (2006) concluded that the data were best represented by a model in which spiral arms have a counter-clockwise field and interarm regions have a clockwise field. This is similar to the BSS models, but with twice as many reversals. This idea has received support from Nota & Katgert (2010) who found evidence from both pulsar and EGRS RMs for a clockwise interarm field between counter-clockwise fields in the Norma and Crux spiral arms.

In the last decade the NE2001 Galactic electron density model (Cordes & Lazio 2002) has been widely adopted to estimate pulsar distances and also used in modelling of the Galactic magnetic field from EGRS RMs. In this paper, we use the new YMW16 Galactic electron density model (Yao et al. 2017) to estimate pulsar distances from DMs because

this model is believed to give more reliable estimates in general (see Table 6 of Yao et al. 2017). Even so, estimated distances to some pulsars can be in error by a factor of two or even more.

Currently there are 732 published pulsar RMs (see Manchester et al. 2005)[1] of which two are for pulsars in the Small Magellanic Clouds, so we have 730 previously published Galactic RMs. There are nearly 2600 Galactic pulsars in the ATNF Catalogue, so there is much scope for new pulsar RM determinations. In this paper, we present measurements made using the Parkes 64-m radio telescope and the Robert C. Byrd Green Bank Telescope (GBT) in several sessions in 2006 and 2007. About 500 pulsars were observed at Parkes in the 20cm band (∼1400 MHz) and about 125 pulsars were observed using the GBT in the 35cm band (∼800 MHz). Analysis of these observations resulted in the determination of RMs for 477 pulsars, of which 441 are either new or more precise than previous measurements. We combine these new measurements with previously published pulsar RMs and with RMs of EGRS to investigate the large-scale structure of the magnetic field in the Galactic disk. Our observations and data reduction methods and the RM samples that we use are described in §2. Details of the analysis for large-scale magnetic fields in different zones of the Galactic disk are given in §3. In §4 we describe a simple model for the Galactic disk magnetic field that is consistent with the Galactic field structures including arm/interarm reversals that we find and with the distribution of EGRS RMs. We conclude the paper in §5 with a brief summary of the main results and the prospects for future work.

2. OBSERVATIONS, DATA PROCESSING METHODS AND THE RM SAMPLES

2.1. *Pulsar observations*

We used the Parkes 64-m and the Green Bank 100-m telescopes to observe pulsars that had no previously measured rotation measure (RM) but were sufficiently strong to have a reasonable prospect of measuring a significant RM in one hour or less for Parkes or 15 minutes or less for the Green Bank Telescope (GBT). A few strong pulsars with well-known RMs were also observed at the start of each session as system checks.

The Parkes observations were made in seven sessions between 2006 August 2006 and 2008 February. All observations were in the 20-cm band and, except for one session (2007 March), all used the central beam of the 13-beam multibeam receiver (Staveley-Smith et al. 1996) with a central frequency of 1369 MHz and an observed bandwidth of 256 MHz. For the 2007 March observations the "H-OH" receiver was used with the same bandwidth but at a central frequency of 1433 MHz. Both systems receive orthogonal linear polarisations and have a pulsed calibration signal injected at 45° to the two feed probes. The system-equivalent flux densities for the two receivers were about 35 Jy and 42 Jy respectively, determined using calibration observations on and off the strong radio source Hydra A, assumed to have a flux density of 43 Jy at 1400 MHz and a spectral index of −0.91 (Baars et al. 1977). Multibeam observations were made with half the total observing time at each of two feed angles, ±45°, to reduce the effect of feed cross-coupling on the results. This was not necessary for the H-OH receiver. In the 2006 and 2007 sessions, data were recorded using the PDFB1 signal-processing system; for the two 2008 sessions the PDFB2 system was used. Both systems used a polyphase filterbank and produced mean pulse profiles in 1-minute sub-integrations with full polarisation data in each of 512 frequency channels and with either 512 or 1024 bins across the pulse period. A brief description of these systems is given by Manchester et al. (2013). Data were stored for subsequent analysis as PSRFITS files (Hotan et al. 2004).

The GBT observations were made in 2007 November using the 800 MHz prime focus receiver (see Han et al. 2009, for details) which has a system-equivalent flux density on cold sky of approximately 15 Jy. The Green Bank Astronomy Signal Processor (GASP) pulsar observing system (Demorest 2007; Ferdman et al. 2004) was used with a central frequency of 774 MHz and a bandwidth of 96 MHz. Flux density calibration was via 3C286 and 3C295, with assumed flux densities at 774 MHz of 19.44 Jy and 35.45 Jy respectively. A polyphase filterbank was used to divide the signal into 4-MHz sub-bands which were distributed to a 16-node computer cluster for real-time coherent dedispersion and additional frequency division to a final resolution of 0.25 MHz. Dedispersed data in each sub-band were then folded in real-time into 1024 pulse phase bins for 30-s sub-integrations and stored using the PSRFITS data format. A 1-min pulsed calibration observation and two 4-min observations at orthogonal feed angles were made for each pulsar.

2.2. *Analysis methods for rotation measures*

Off-line data analysis including polarimetric calibration and RM determination (see section 2 of Han et al. 2009, for details for GBT observations) was performed using the PSRCHIVE pulsar data processing system (Hotan et al. 2004). First, the frequency-time data were examined for radio frequency interference and affected data were excised. Next the data were calibrated to compensate for instrumental gain and phase variations across the band, converted to Stokes

[1] http://www.atnf.csiro.au/research/pulsar/psrcat, V1.56

parameters and placed on a flux density scale. Where applicable, the two observations at orthogonal feed angles were then summed and the whole observation summed in time. From the resulting multi-frequency polarisation profiles, the RM of each pulsar was obtained as follows. A first guess at the RM was found by searching the range of ±2000 rad m^{-2} for a peak in the total linear polarisation $L = (Q^2 + U^2)^{1/2}$ summed across all on-pulse phase bins and across the band, where Q and U are the linear Stokes parameters. This value was then iteratively refined by taking the current best estimate of the RM and summing the data separately in the two halves of the band. A correction to the RM was then obtained from a weighted mean position-angle difference across the pulse profile. Taking the weighted mean difference makes the process relatively immune to orthogonal mode transitions (cf. Ramachandran et al. 2004). The final RM value was then obtained by subtracting the ionospheric RM contribution to give the RM along the path from the top of the ionosphere to the pulsar. The ionospheric RM was computed using a model for the geomagnetic field and the International Reference Ionosphere 2007 (Bilitza & Reinisch 2008). It was typically between 0.4 to 3.5 rad m^{-2} for GBT observations and −0.2 to −2.0 rad m^{-2} for Parkes observations, with a largely diurnal variation.

Table 1. Observed rotation measures for 477 pulsars

PSR Name	Period (s)	DM (cm^{-3})	Gal. l (°)	Gal. b (°)	Dist. (kpc)	RM (rad m^{-2})	$\sigma_{\rm RM}$ (rad m^{-2})	Telescope	Obs. Date
J0014+4746	1.2407	30.85	116.50	−14.63	1.78	−15.3	0.7	GBT	071119
J0030+0451	0.0049	4.33	113.14	−57.61	0.36	16.8	15.9	PKS	080112
J0034−0534	0.0019	13.76	111.49	−68.07	1.35	−38.1	17.5	PKS	080113
J0034−0721	0.9430	11.38	110.42	−69.81	1.03	3.9	10.4	PKS	080215
J0055+5117	2.1152	44.12	123.62	−11.58	1.94	−66.6	1.5	GBT	071118
J0113−7220	0.3259	125.49	300.62	−44.69	59.70	87.0	28.7	PKS	080111
J0117+5914	0.1014	49.42	126.28	−3.46	1.77	−8.1	6.7	GBT	071118

NOTE—Table 1 is published in its entirety in the machine-readable format. A portion is shown here for guidance regarding its form and content.

Table 2. Weighted mean rotation measures

PSR Name	RM	$\sigma_{\rm RM}$	PSR Name	RM	$\sigma_{\rm RM}$
J0437−4715	0.4	0.2	J1730−2304	−4.9	1.8
J0656−2228	83.0	5.4	J1759−2302	1574.7	13.0
J0815+0939	53.1	5.0	J1812−2102	322.6	4.2
J0842−4851	145.1	11.3	J1816−1729	82.9	4.1
J0900−3144	82.0	1.3	J1843−0355	239.7	9.8
J0902−6325	−59.2	2.1	J1852+0305	263.9	14.6
J0942−5552	−63.2	1.4	J1915+0738	−6.8	1.5
J0952−3839	331.7	9.5	J1927+1856	74.4	5.8
J1032−5911	100.0	6.7	J1932+1059	−7.5	0.4
J1626−4537	111.9	11.2	J2053−7200	15.2	2.0
J1707−4053	−186.5	2.5			

2.3. *Rotation measure samples*

Table 1 lists 501 RM measurements for 477 pulsars; for 21 pulsars, repeated observations were made in different sessions, either as a system check or in an attempt to get a better RM measurement. Columns 1 – 6 list the pulsar J2000 name, period, dispersion measure, Galactic longitude, Galactic latitude and the estimated pulsar distance. Unless independent distance estimates are available, distances are based on the YMW16 electron-density model (Yao et al.

2017). The next two columns list the measured RM and its uncertainty, and the final two columns give the telescope and date of the observations. For the pulsars with repeated measurements, we formed weighted mean RMs for use in subsequent analysis. These are listed in Table 2.

The ATNF Pulsar Catalogue (V1.56) lists published RMs for 732 pulsars, of which two are for pulsars that lie in the Small Magellanic Cloud. A total of 91 pulsars in Table 1 have previously published RM measurements and so the total number of available Galactic RMs is 1116. We compare RM values with the previously published values in Table 3. The first two columns give the pulsar J2000 name and the B1950 name if one exists and the next two columns give our best RM measurement from Table 1 or Table 2. The following columns are grouped in sets of three, with the first two columns giving a previously published RM and its quoted uncertainty and the third column giving the reference key for the publication. More recent publications are listed first and reference keys are identified in the Table footnote. Where a reference key for an earlier paper is marked with an asterisk, the corresponding RM measurement is evidently the best available. This applies to 36 of the 91 pulsars and these values are used in subsequent analyses.

Table 3. Comparison of observed rotation measures with previously published values

PSR Name		RM	$\sigma_{\rm RM}$	$\rm RM_1$	$\sigma_{\rm RM_1}$	Ref. 1	$\rm RM_2$	$\sigma_{\rm RM_2}$	Ref. 2	$\rm RM_3$	$\sigma_{\rm RM_3}$	Ref. 3
J0014+4746	B0011+47	−15.3	0.7	−8.7	1.1	fdr15						
J0034−0721	B0031−07	3.9	10.4	9.89	0.07	nsk+15*	9.8	0.2	hl87	10.0	1.0	man74
J0437−4715	···	0.4	0.2	1.5	0.5	nms+97	0.0	0.4	ymv+11			
J0448−2749	···	−0.7	5.4	24.0	17.0	hml+06						
J0452−1759	B0450−18	12.7	0.9	11.1	0.3	jkk+07*	13.8	0.7	hl87	15.0	2.0	man74
J0536−7543	B0538−75	23.8	0.9	25.2	1.0	njkk08	28.0	2.0	hmq99	21.4	0.5	qmlg95
J0630−2834	B0628−28	45.4	0.7	46.5	0.1	jhv+05*	46.6	1.3	hml+06	45.7	0.5	vdhm97
J0656−2228	···	83.0	5.4	38.0	12.0	njkk08						
J0738−4042	B0736−40	9.3	0.9	12.1	0.6	njkk08*	14.5	0.7	vdhm97	12.5	0.6	jkk+07
J0831−4406	···	531.4	22.9	509.0	20.0	hml+06						
J0835−4510	B0833−45	29.9	0.6	31.38	0.01	jhv+05*	36.6	0.1	man74	38.2	0.1	hmm+77
J0838−2621	···	96.3	12.4	86.0	13.0	njkk08						
J0843−5022	···	189.5	15.9	155.0	23.0	njkk08						
J0846−3533	B0844−35	136.5	3.5	144.0	8.0	hl87	159.0	9.0	qmlg95			
J0942−5552	B0940−55	−62.8	1.8	−61.9	0.2	tml93*						
J0953+0755	B0950+08	6.1	1.6	−0.66	0.04	jhv+05*	2.0	2.0	hl87	1.8	0.5	man74
J1012+5307	···	1.0	1.4	2.98	0.06	nsk+15*						
J1017−5621	B1015−56	332.8	3.6	365.0	7.0	njkk08						
J1022+1001	···	8.6	9.5	1.39	0.05	nsk+15*	−0.6	0.5	ymv+11			
J1024−0719	···	−5.8	3.5	−8.2	0.8	ymv+11*						
J1045−4509	···	90.5	3.5	92.0	1.0	ymv+11*	82.0	18.0	mh04			
J1047−3032	···	−26.2	6.2	−36.0	23.0	njkk08						
J1052−5954	···	−269.7	11.7	−280.0	24.0	wj08						
J1054−5943	···	150.6	30.1	46.0	34.0	hml+06						
J1115−6052	···	251.6	4.6	257.0	18.0	wj08						
J1156−5707	···	228.0	6.3	238.0	19.0	wj08						
J1237−6725	···	72.5	21.8	24.0	14.0	tjb+13*						
J1240−4124	B1237−41	17.3	10.4	15.0	13.0	njkk08						
J1300+1240	B1257+12	2.3	3.5	7.91	0.06	nsk+15*						
J1312−6400	···	−12.9	9.1	40.0	30.0	hml+06						
J1320−3512	···	−4.7	3.6	−7.8	2.0	njkk08*						
J1321+8323	B1322+83	−27.5	1.4	−23.1	1.1	fdr15*						
J1340−6456	B1336−64	−2.1	20.8	−37.0	23.0	njkk08						
J1352−6803	···	20.4	2.4	30.0	7.0	njkk08						
J1403−7646	···	63.4	17.3	94.0	16.0	njkk08*						
J1514−4834	B1510−48	13.8	18.2	18.0	14.0	njkk08*						

Table 3 continued on next page

Table 3 *(continued)*

PSR Name		RM	$\sigma_{\rm RM}$	$\rm RM_1$	$\sigma_{\rm RM_1}$	Ref. 1	$\rm RM_2$	$\sigma_{\rm RM_2}$	Ref. 2	$\rm RM_3$	$\sigma_{\rm RM_3}$	Ref. 3
J1524−5625	···	185.8	3.3	180.0	20.0	wj08						
J1524−5706	···	−475.5	5.0	−470.0	20.0	wj08						
J1534−5405	B1530−53	−86.8	6.0	−69.0	12.0	njkk08						
J1600−3053	···	−11.9	3.7	−15.5	1.0	ymv+11*						
J1614−3937	···	84.0	13.7	133.0	16.0	njkk08						
J1615−5537	B1611−55	10.2	14.8	−54.0	16.0	njkk08						
J1623−4256	B1620−42	109.6	5.7	−15.0	8.0	hml+06						
J1628−4804	···	−447.0	15.5	−431.0	43.0	hml+06						
J1644−4559	B1641−45	−626.9	0.8	−617.0	1.0	hml+06	−611.0	2.0	vdhm97			
J1650−1654	···	16.1	5.6	7.0	14.0	njkk08						
J1651−4246	B1648−42	−167.4	1.1	−154.0	5.0	hml+06						
J1702−4128	···	−165.5	4.7	−160.0	20.0	wj08						
J1705−3950	···	−98.8	1.9	−106.0	14.0	wj08						
J1707−4053	B1703−40	−183.7	3.4	168.0	4.0	njkk08	−207.0	25.0	qmlg95			
J1709−4429	B1706−44	−3.5	0.8	0.70	0.07	jhv+05*	−7.0	4.0	qmlg95			
J1713+0747	···	7.0	7.6	8.4	0.6	ymv+11*						
J1717−4054	B1713−40	−811.4	4.1	−800.0	100.0	khs+14						
J1721−3532	B1718−35	148.1	5.9	159.0	4.0	njkk08*	205.0	75.0	qmlg95			
J1730−2304	···	−4.9	1.8	−7.2	2.2	ymv+11						
J1737−3137	···	449.6	5.1	448.0	17.0	wj08						
J1737−3555	B1734−35	68.6	9.8	50.0	4.0	njkk08*						
J1744−1134	···	6.0	2.1	−1.6	0.7	ymv+11*						
J1818−1422	B1815−14	1173.9	7.3	1168.0	13.0	hml+06						
J1822−4209	···	40.7	10.6	−13.0	9.0	hml+06						
J1828−1101	···	59.4	2.5	45.0	20.0	wj08						
J1835−0643	B1832−06	44.1	14.6	62.0	38.0	hml+06						
J1835−1106	···	42.9	2.1	42.0	3.0	njkk08						
J1836−1008	B1834−10	826.6	4.5	−1000.0	99.0	hl87						
J1837−0045	···	131.6	6.7	130.0	17.0	njkk08						
J1837−0604	···	320.8	4.2	450.0	25.0	wj08						
J1837−1837	···	137.2	9.0	138.0	8.0	njkk08*						
J1841−0345	···	450.5	2.6	447.0	15.0	wj08						
J1845−0743	···	448.4	1.8	440.0	12.0	wj08						
J1853−0004	···	648.7	4.7	647.0	16.0	wj08						
J1900−2600	B1857−26	−9.3	0.2	−2.3	0.8	jhv+05	−7.3	0.8	hl87			
J1900−7951	B1851−79	18.6	5.4	43.0	12.0	qmlg95						
J1901−1740	···	−20.0	8.7	63.0	33.0	njkk08						
J1903+0135	B1900+01	68.4	2.4	72.3	1.0	hl87*						
J1915+1606	B1913+16	364.5	5.0	430.0	73.0	hml+06						
J1917+2224	B1915+22	168.2	23.5	192.0	49.0	wck+04						
J1919+0134	···	44.8	18.2	47.0	4.0	njkk08*						
J1921+1419	B1919+14	164.8	3.1	275.0	60.0	hr10						
J1926+0431	B1923+04	−39.5	8.1	0.0	11.0	hl87						
J1932+1059	B1929+10	−8.2	0.8	−6.87	0.02	jhv+05*	−7.0	2.0	hl87	−8.6	1.8	man74
J1932−3655	···	3.8	4.7	−8.0	3.0	njkk08*	−6.0	3.0	hmq99			
J1935+1616	B1933+16	−2.3	0.5	−10.2	0.3	jhv+05	−2.0	2.0	hl87	−1.9	0.4	man74
J1943−1237	B1940−12	−75.4	6.2	−10.0	8.0	hl87						
J1949−2524	B1946−25	−51.9	13.8	−13.0	8.0	hmq99						
J2038−3816	···	20.5	9.5	38.0	14.0	njkk08	68.0	18.0	hml+06			

Table 3 continued on next page

Table 3 *(continued)*

PSR Name		RM	σ_{RM}	RM_1	σ_{RM_1}	Ref. 1	RM_2	σ_{RM_2}	Ref. 2	RM_3	σ_{RM_3}	Ref. 3
J2048−1616	B2045−16	−9.7	1.7	−10.0	0.3	jkk+07*	−9.0	2.0	hl87	−10.8	0.4	man74
J2053−7200	B2048−72	15.0	2.0	17.0	1.0	qmlg95*						
J2108−3429	···	93.1	8.9	39.0	12.0	njkk08	50.0	20.0	hmq99			
J2155−3118	B2152−31	33.8	14.4	21.0	3.0	hl87*						
J2324−6054	B2321−61	15.6	2.0	−11.0	8.0	hml+06	39.0	6.0	qmlg95			

All RM values and their uncertainties are in units of rad m^{-2}.
References marked with * signify the best available RM values if not from the present work.
References: fdr15: Force et al. (2015); hl87: Hamilton & Lyne (1987); hml+06: Han et al. (2006); hmm+77: Hamilton et al. (1977); hmq99: Han et al. (1999); hr10: Hankins & Rankin (2010); jhv+05: Johnston et al. (2005); jkk+07: Johnston et al. (2007); khs+14: Kerr et al. (2014); man74: Manchester (1974); mh04: Manchester & Han (2004); njkk08: Noutsos et al. (2008); nms+97: Navarro et al. (1997); nsk+15: Noutsos et al. (2015); qmlg95: Qiao et al. (1995); tjb+13: Tiburzi et al. (2013); tml93: Taylor et al. (1993); vdhm97: van Ommen et al. (1997); wck+04: Weisberg et al. (2004); wj08: Weltevrede & Johnston (2008); ymv+11: Yan et al. (2011)

Most of the new measurements are in good agreement with previously published values with only ten cases where the RM difference exceeds five times the combined uncertainty. Some of the smaller differences are likely to result from temporal variations of the RM as seen in, for example, the Vela pulsar (Hamilton et al. 1985). Four of the measurements are discrepant by more than 10σ. The largest of these discrepencies is for PSR J1707−4053 where our measured RM is -183.7 ± 3.4 rad m^{-2} compared to $+168.0 \pm 4.0$ rad m^{-2} from Noutsos et al. (2008). Our measurement agrees well with a more recent measurement by Force et al. (2015) and with an older measurement by Qiao et al. (1995) and so it appears that the Noutsos et al. (2008) measurement is incorrect. The other three cases are PSRs J1623−4256, J1836−1008 and J1935+1616. Previous observations for PSR J1623−4256 (Han et al. 2006) unfortunately were processed with an incorrect DM; re-analysis of these data with the correct DM gives an RM consistent with that presented here. For PSR J1836−1008, the new RM in Table 1 is confirmed by analysis of more recent data. For PSR J1935+1616, the new measurement agrees with two previous determinations, so it appears that the Johnston et al. (2005) result is discrepant. Among the 1116 Galactic pulsars with RMs, 787 are at low Galactic latitudes ($|b| < 8°$) and hence most relevant to the present work.

We also make use of 3933 RMs of extragalactic radio sources (EGRS) with Galactic latitude $|b| < 8°$ (Xu & Han 2014).[2] Of these, 2942 are from the analysis of NVSS data by Taylor et al. (2009), 283 from Brown et al. (2003), 184 from Van Eck et al. (2011), and 104 from Brown et al. (2007). The remaining 298 RMs are from a variety of papers.

3. LARGE-SCALE FIELD STRUCTURE IN THE GALACTIC DISK

Figure 1 shows the overall RM distribution for both pulsars and EGRS within 8° of the Galactic plane. In general terms, there is predominance of positive RMs in the first and third Galactic quadrants (i.e., $0° < l < 90°$ and $180° < l < 270°$) and of negative RMs in the other two quadrants. Since positive RMs indicate fields directed toward us, overall these results suggest clockwise fields in the outer Galaxy and counterclockwise fields inside the Sun viewed from the north Galactic pole. At least in the first and fourth quadrants, there is a tendency for more distant pulsars to have larger RMs, indicating the large scale of the counter-clockwise fields in the inner Galaxy.

Closer examination of Figure 1 shows however that this counter-clockwise field in the inner Galaxy is predominantly confined to the spiral arms. This is most clearly revealed by increasingly negative RMs in the vicinity of spiral-arm tangential points, for example, the Crux tangential region near Galactic longitude $l \sim 310°$ and the Norma tangential region near Galactic longitude $l \sim 330°$. In contrast, in the interarm tangential regions, for example, in the Norma-Crux interarm region near $l \sim 320°$ and the Crux-Carina interarm region ($l \sim 300°$), RMs are positive, indicating a clockwise field similar to the local interarm region. Furthermore, EGRS RMs in the direction around the Crux-Carina interarm region ($l \sim 300°$) are nearly all large and positive, confirming the large-scale clockwise field. In the first quadrant, the counter-clockwise fields in the spiral arms are generally clear, but it is difficult to identify the direction of the interarm fields since the spiral arms are much closer and less well defined in this quadrant.

In the following sub-sections, we quantify these RM trends by fitting the observed variations of RM with DM and distance over specified distance ranges and directions and comparing these fits with the mean EGRS RM in the same

[2] http://zmtt.bao.ac.cn/RM/

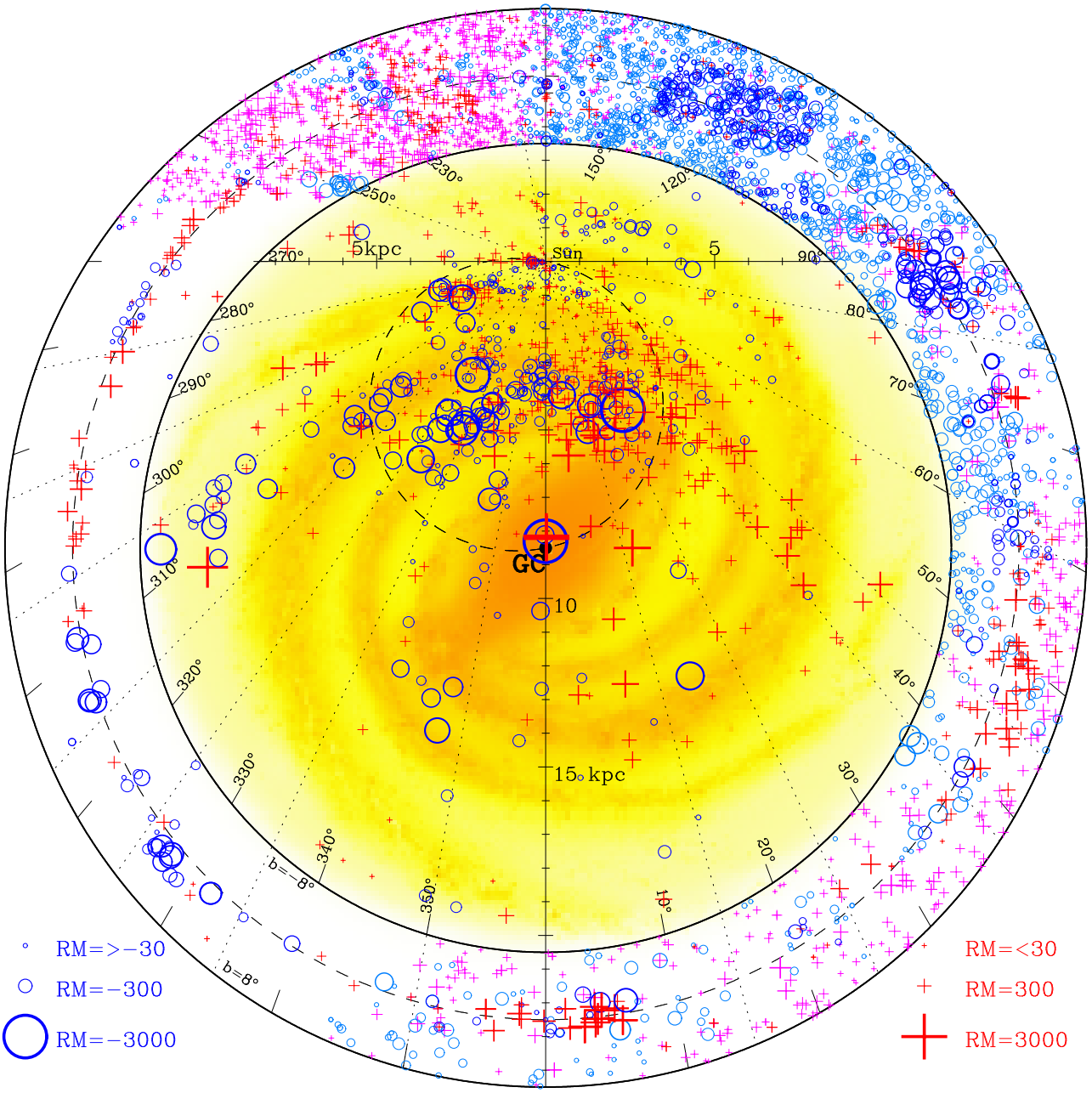

Figure 1. Distribution of pulsars and EGRS with measured RMs in Galactic coordinates. The central part of the figure shows RMs for pulsars with Galactic latitude $|b| < 8°$ projected on to the Galactic disk and the outer ring shows the distribution of RMs for EGRS with $|b| < 8°$. Radial distance in the outer ring is linearly proportional to Galactic latitude. The light blue and pink symbols indicate the RMs derived from NVSS data (Taylor et al. 2009). Blue circles and red + signs in both central part and the outer ring indicate negative and positive RMs respectively and the symbol size is proportional to $|RM|^{1/2}$. The background in the central part of the figure is an artist's impression of the Galactic structure modified from a NASA/JPL image (Credit: R. Hurt) according to updated spiral arms of Hou & Han (2014). The dashed circle gives the locus of tangent points assuming a spiral pitch angle of 11° and the dotted lines give the longitude boundaries of the approximately tangential spiral-arm or interarm zones and anti-center zones used for the RM analyses in this paper.

direction. As discussed in §1, we can use Equation 2 to give the mean line-of-sight component of the interstellar magnetic field, weighted by the local n_e, over different distance intervals along the line of sight to pulsars in similar directions. Distances to individual pulsars derived from Galactic n_e models are subject to unpredictable errors. Therefore, rather than fitting to pulsar pairs individually, we fit linear trend lines to plots of RM vs distance over specified distance intervals and to plots of RM vs DM over DM intervals that match the distance range as closely as possible. The averaging over groups of pulsars minimises the effects of small-scale B-field fluctuations and distance

errors. We emphasize that the derived B-field estimates are derived solely from the RM – DM fits.

In order to improve the reliability of the B-field estimates, we omitted RMs of 15 pulsars with an uncertainty larger than 35 rad m^{-2} and used the Maximum Likelihood Robust Estimate routine from Press et al. (1996, see pp.694-700) to fit a line by minimizing absolute deviation (i.e. the MEDFIT subroutine). This "robust" fitting is necessary so that outliers resulting from HII regions, other unmodelled electron-density fluctuations or magnetic-field fluctuations along the path do not unduly influence the slope of the fitted line. We take as the uncertainty of the slope the mean absolute deviation of RMs from the fitted line divided by the DM range for the fitting. Generally, the scatter around the fitted lines in the RM – DM plots is dominated by real fluctuations in the line-of-sight magnetic field components, not RM measurement errors which are very small compared to the data scatter. Positive slopes of RM vs DM correspond to magnetic fields directed toward us, i.e., to clockwise fields in the Galactic Quadrant 4 and counter-clockwise fields in the Galactic Quadrant 1.

The regions for which we have analysed the RMs are listed in Table 4. The arm and interarm designations are guided by the 4-arm spiral model of Hou & Han (2014, i.e. the background images of Fig. 1), and the ranges for the Galactic longitude l are chosen accordingly. For the inner Galactic quadrants, the fitted regions are guided by the tangential zones since spiral fields have a small angle to our line of sight and distance errors have less effect there. However, where clear trends in RM versus DM or distance exist, the fitted region has been adjusted to encompass these. For the outer Galactic regions, the fitted regions are determined by the RM trends. The fifth column of Table 4 gives the number of pulsars in the fitted region or the number of EGRS for each longitude range. The next two columns give estimates of $B_{||}$ and field direction from the RM – DM fits in the vicinity of tangential regions of Quadrants 1 and 4. Comparison of the RMs of background EGRS with the RMs of the most distant pulsars in each zone gives a good indication of the magnetic field orientation beyond the pulsars, but it is not possible to reliably estimate field strengths in these cases because of the uncertain DM contribution.

Table 4. Galactic disk zones and their magnetic fields

Region	l–Range (°)	D–Range (kpc)	DM–Range (cm^{-3} pc)	No. PSRs or EGRS	$B_{||}$ (μG)	B-field Direction	Arrow l (°)	Arrow D (kpc)
Quadrant 1								
Near 3-kpc	15 – 25	3.5 – 6.5	350 – 850	25	$+4.0 \pm 0.7$	ccw	20	5.5
Near 3-kpc – EGRS	15 – 25	6.5 – E	850 – E	71		cw	20	11.0
Scutum	25 – 38	4.0 – 8.0	200 – 800	46	$+0.4 \pm 0.4$	ccw	32	7.0
Scutum – EGRS	25 – 38	9.5 – E	900 – E	78		–	– –	– –
Scutum – Sgr	38 – 45	4.0 – 12.0	200 – 500	25	$+3.3 \pm 0.9$	ccw	42	8.5
Scutum-Sgr – EGRS	38 – 45	12.0 – E	500 – E	37		cw	42	13.0
Sagittarius	45 – 60	3.0 – 8.5	100 – 300	30	$+1.4 \pm 1.0$	ccw	50	5.0
Sagittarius – EGRS	45 – 60	8.5 – E	300 – E	176		cw	50	8.5
Local – Perseus	60 – 80	3.5 – 8.0	70 – 250	14	$+0.7 \pm 0.7$	ccw	73	7.0
Local–Perseus – EGRS	60 – 80	8.0 – E	250 – E	225		cw	73	10.5
Outer Zones for the local region and the Perseus arm								
Local Q1-Q2	80 – 120	1.0 – 5.0	10 – 200	18	-1.4 ± 0.6	cw	105	2.5
Local Q1-Q2 – EGRS	80 – 120	5.0 – E	200 – E	576		ccw	105	4.0
Outer Q2	120 – 190	–	–			–	– –	– –
Outer Q3	190 – 250	0.0 – 3.5	0 – 130	13	$+1.3 \pm 0.4$	cw	235	2
Outer Q3 – EGRS	190 – 250	3.5 – E	130 – E	841		ccw	230	3.5
Local Q3-Q4	250 – 270	0.0 – 6.0	30 – 280	20	$+1.1 \pm 0.5$	cw	260	4.0
Local Q3-Q4 – EGRS	250 – 270	6.0 – E	280 – E	138		ccw	260	6.5
Outer Carina	270 – 282	0.1 – 1.1	50 – 250	23	$+0.8 \pm 0.5$	cw	276	0.7
Outer Carina – EGRS	270 – 282	–	250 – E	26		ccw	276	9.0
Quadrant 4								
Carina	282 – 294	2.0 – 4.0	250 – 550	22	-1.2 ± 1.0	ccw	288	3.0

Table 4 continued on next page

Table 4 *(continued)*

Region	l–Range (°)	D–Range (kpc)	DM–Range (cm^{-3} pc)	No. PSRs or EGRS	$B_{\|\|}$ (μG)	B-field Direction	Arrow l (°)	Arrow D (kpc)
Carina – EGRS	282 – 294	4.0 – E	550 – E	8		cw	288	11.0
Carina – Crux	294 – 304	2.0 – 10.0	100 – 600	21	$+1.9 \pm 0.3$	cw	299	7.0
Carina–Crux – EGRS	294 – 304	10.0 – E	600 – E	13		ccw	299	12.0
Crux	304 – 316	4.0 – 13.0	200 – 800	38	-1.6 ± 0.5	ccw	310	7.5
Crux – EGRS	304 – 316	13.0 – E	800 – E	13		cw	310	13.0
Crux – Norma	316 – 325	3.0 – 11.0	250 – 700	9	$+1.3 \pm 0.3$	cw	320	6.0
Crux-Norma – EGRS	316 – 325	11.0 – E	700 – E	6		ccw	320	12.0
Norma	325 – 335	4.0 – 6.5	300 – 800	15	-3.7 ± 0.6	ccw	330	6.5
Norma – EGRS	325 – 335	10.0 – E	900 – E	20		cw	330	12.5
Far 3-kpc	335 – 350	8.0 – 13.5	400 – 700	23	-3.1 ± 1.1	ccw	343	12.5
Far 3-kpc – EGRS	335 – 350	13.5 – E	700 – E	23		cw	343	15.5

3.1. *Fourth Galactic Quadrant*

We discuss Quadrant 4 first since, as viewed from the Earth, the Galactic spiral arm and interarm regions are more clearly separated than they are in Quadrant 1. Figure 2 shows the Quadrant 4 pulsar RMs as functions of distance and DM and EGRS RMs as a function of Galactic latitude or longitude for the longitude ranges given in Table 4.

From the top subpanels down, Figure 2 shows alternating interarm and arm regions (cf. Table 4). It is striking that the field directions alternate in the tangential regions, that is, the RM – DM slope is generally negative in arm regions, corresponding to counter-clockwise field directions, but positive in interarm regions, corresponding to clockwise field directions.

Despite the fact that there are few known pulsars beyond the tangential zones, comparison of RMs for distant pulsars with EGRS RMs (Figure 2) clearly shows that for all of these longitude zones there are field reversals beyond the tangential regions. For example, at the far end of the Norma tangential region ($325° < l < 335°$) pulsar RMs are very negative (as much as ~ -1500 rad m^{-2}) whereas RMs of EGRS in this direction have a much smaller median RM of about -200 rad m^{-2}. This implies at least one field reversal along this line of sight.

Similar distant reversals are seen for most of the other arm and interarm regions. It is not possible to say exactly where these reversals occur because of large uncertainties in the pulsar distances, although they definitely occur beyond the fitted regions. Since both the magnetic field strength and the electron density have a general decline with increasing Galactocentric radius and, at least in Quadrants 1 & 4, the field makes a greater angle with the line of sight beyond the tangential point, it is reasonable to assume that the most significant zone affecting the gradient in the RMs of Galactic – EGRS is centered on the extension of the next outer arm/interarm region. For example, the Norma – EGRS reversed field probably results from the extension of the clockwise fields found in the tangential zone of the Crux – Norma interarm region ($316° < l < 325°$). The Crux – Norma interarm zone itself appears to show a reversal between the end of the tangential region and the edge of the Galaxy, probably due to counter-clockwise fields in the distant Crux arm. Similar considerations apply to the 3-kpc, Crux, Carina – Crux and Carina zones although the evidence is generally somewhat weaker compared to the Norma – Crux zones. Table 4 lists the derived field strengths and directions, quantifying these field reversals.

These reversals are further illustrated by Figure 3 which shows the RM distributions for pulsars in the tangential zones and for the EGRS. The pulsar RMs (second panel) show a clear alternating structure between arm and interarm regions at least up to the Carina region ($l < 294°$) with arm regions (Crux, $l \sim 310°$ and Norma, $l \sim 330°$) predominently negative (corresponding to counter-clockwise fields) and interarm regions predominently positive (clockwise fields). The RMs of EGRS do not show these alternative reversals as clearly as pulsar RMs, especially in the interarm regions.

The derived field strengths and directions are illustrated in Figure 4 where the arrows are placed at the approximate mean distance for the relevant RM – DM fit for the pulsars and near the next spiral feature for the pulsar – EGRS fields as listed in Table 4. As discussed above, there is substantial distance uncertainty in both cases, but in general, the derived field directions are consistent with reversals between the arm and interarm regions. Arrow locations are

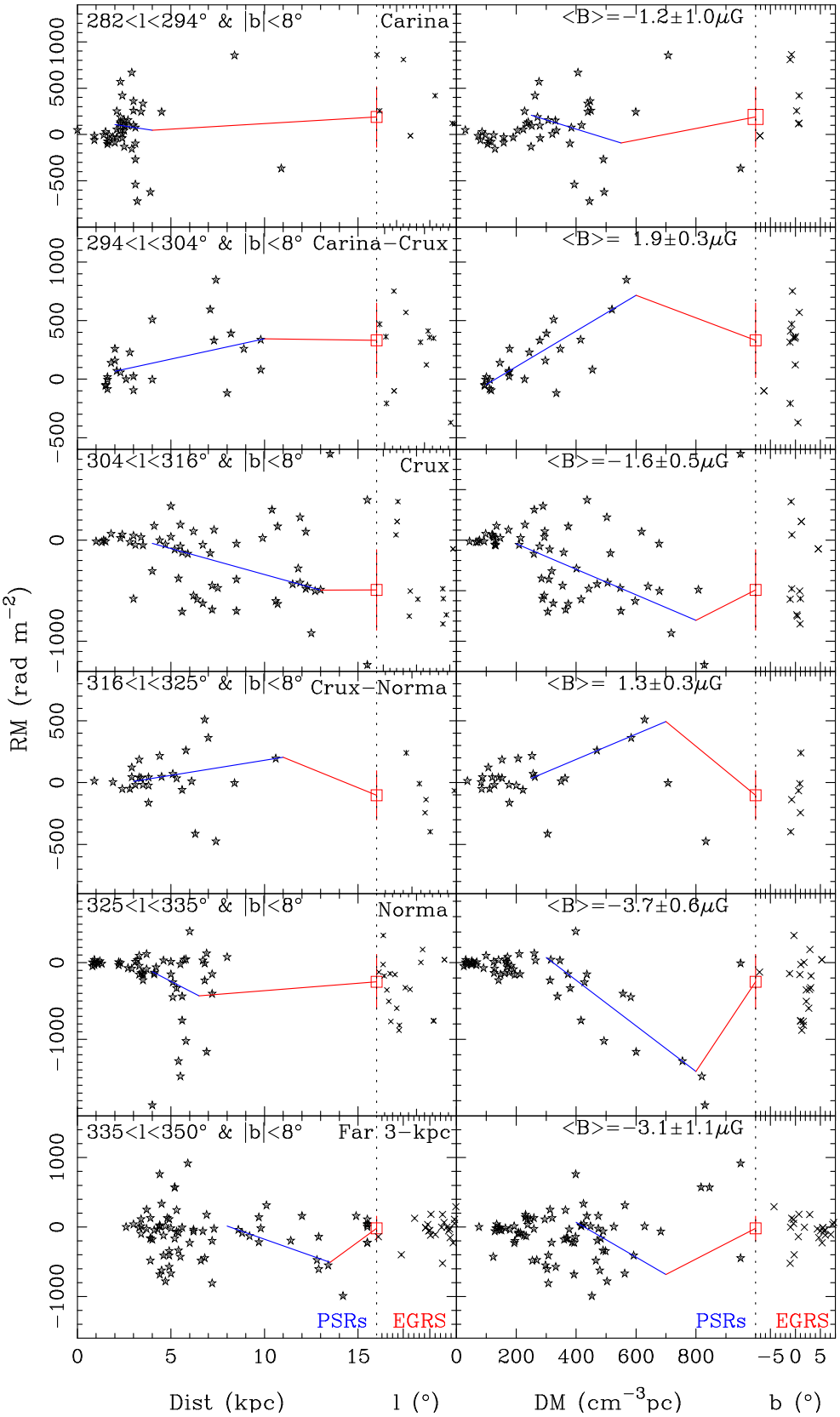

Figure 2. RMs for pulsars versus pulsar distance and DM and RMs for EGRS versus Galactic longitude (left panels, scale ticks are given but not labelled) and Galactic latitude (right panels) for arm and interarm regions in the fourth Galactic quadrant. The blue lines represent linear fits to the pulsar RM gradients, primarily in the tangential regions. For the RM – DM case, the slope of this line gives the mean interstellar line-of-sight magnetic field in the region with positive slopes corresponding to clockwise fields. The red square and error bar represent the median and rms deviation from the median of the RMs of EGRS in the region. Uncertainties in the measured RMs are plotted but are generally smaller than the plotted symbol size.

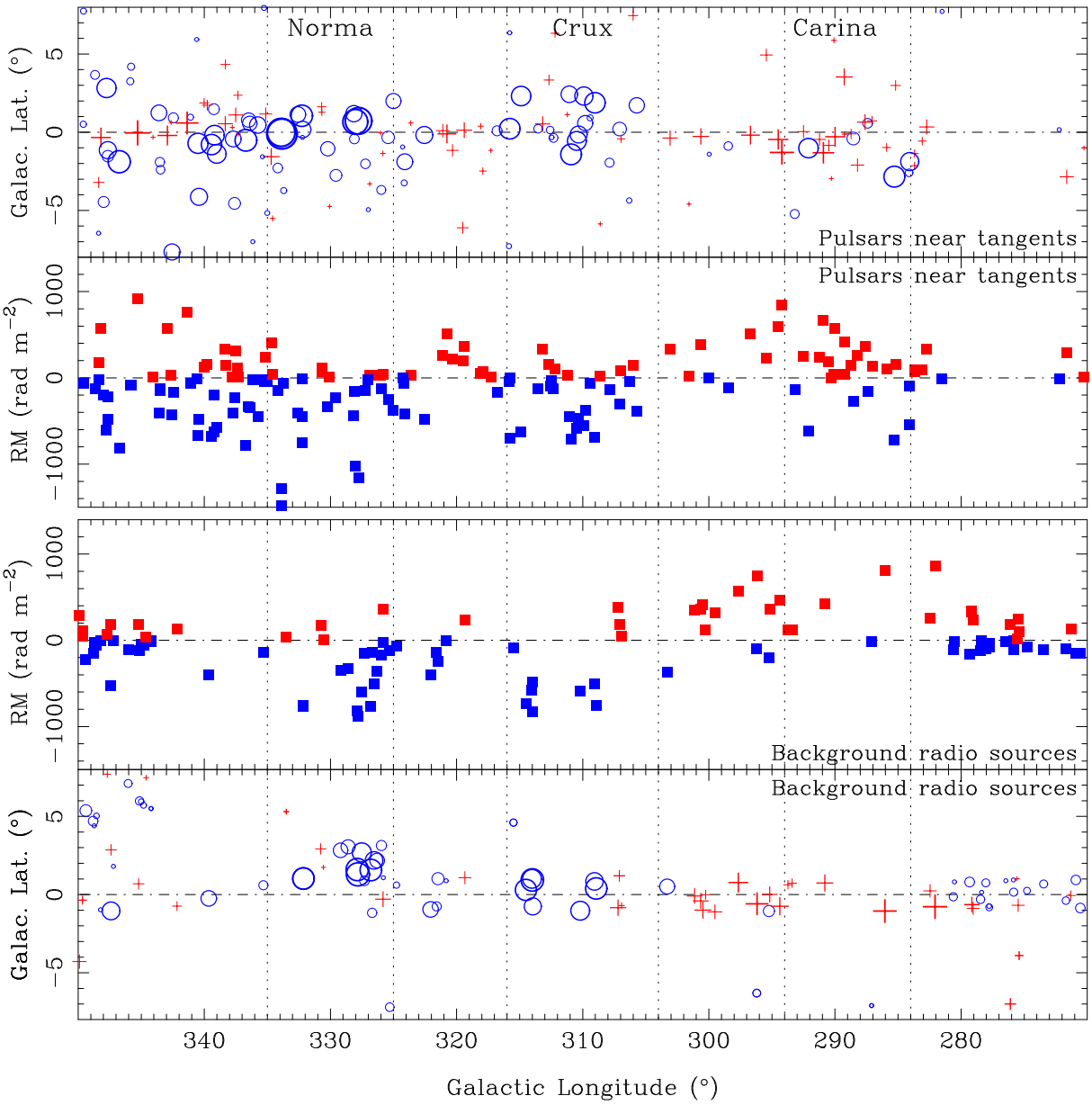

Figure 3. RMs for pulsars in the tangential zone (±50% from the tangent trajectory, considering the large uncertainty of pulsar distances) and RMs for EGRS versus Galactic longitude in the fourth Galactic quadrant. The top and bottom panels show their distribution in Galactic latitude of the pulsars and the EGRS respectively with the symbol size proportional to $RM^{1/2}$.

listed in the final two columns of Table 4.

3.2. *First Galactic Quadrant*

RMs in Quadrant 1 are generally positive (see Figure 1) and there is a much less clear delineation between the arm and interarm regions compared to Quadrant 4. Many authors have described the positive and increasing RMs in the Sagittarius arm, implying a counter-clockwise field in this arm (e.g., Lyne & Smith 1989; Rand & Lyne 1994; Han & Qiao 1994; Indrani & Deshpande 1999; Weisberg et al. 2004). Figure 5 shows positive RMs increasing with distance and DM in Sagittarius tangential region ($45° < l < 60°$). The Sagittarius arm becomes the Carina arm in Quadrant 4, supporting the idea that Carina fields conform to the counter-clockwise pattern.

However, fields in the nominal Scutum – Sagittarius interarm region ($38° < l < 45°$) show an even clearer positive and increasing pattern, implying counter-clockwise fields in this region also. A possible explanation for this is that these fields originate in more distant parts (up to 12 kpc, including both the Sagittarius arm and the Perseus arm). However, the RMs of EGRS are much smaller on average, indicating the field reversals beyond these spiral arms.

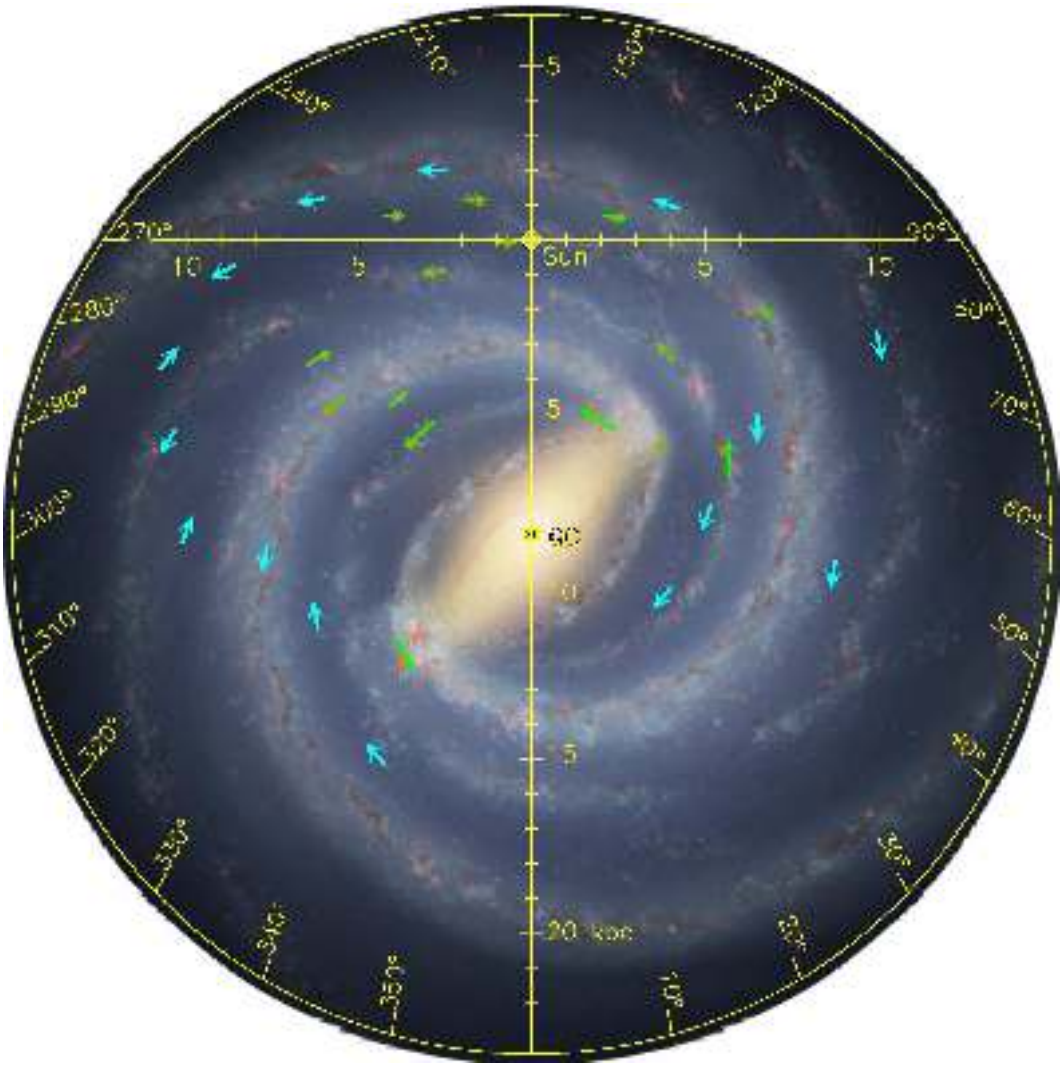

Figure 4. Large-scale magnetic field directions in the Galactic disk, derived from the fitted gradients of pulsar RMs with DM/distance and the comparison of RMs of EGRS with RMs of distant pulsars. The orange arrows give the derived line-of-sight magnetic field components and the green arrows show the inferred spiral field. For both of these, the arrow length is proportional to the square root of the field strength. The blue arrows, which are all of the same length, give the inferred spiral field direction derived from the comparison of RMs for EGRS with RMs for distant pulsars and are placed at the distance of the central axis of the next outer spiral feature (arm or interarm). The background image shows an artist's impression of the structure of our Galaxy from a NASA/JPL image (Credit: R. Hurt) modified according to the spiral structure of Hou & Han (2014).

Positive and increasing RMs are also seen in the Near 3-kpc region ($15° < l < 25°$) which could result from the inner part of the Norma arm.

Beyond the interarm region with clockwise magnetic fields, the RM change to positive for distant pulsars ($D > 5$ kpc) in the longitude range of $60° < l < 80°$in Figure 5 shows some evidence for counter-clockwise fields in the Perseus arm. The small RMs of EGRS in this direction indicate another field reversal beyond the Perseus arm. The counter-clockwise field in the Perseus arm is echoed by the RM difference of pulsars in the outer Galaxy nearer than or within the arm and the RMs of EGRS, as we will see below.

As in Quadrant 4, there is evidence for reversals beyond the tangential regions based on the mean RMs of EGRS, at least for the Scutum – Sagittarius interarm region and the Near 3-kpc region. As discussed above, we do not know exactly where these reversals occur because of the large DM/distance ranges for RM changes, but it is reasonable to assume that they occur in the next arm/interarm region. As for Quadrant 4, these field strengths and directions are listed in Table 4 and illustrated in Figure 4.

3.3. *Outer Galactic Zones for the local interarm region and the Perseus arm*

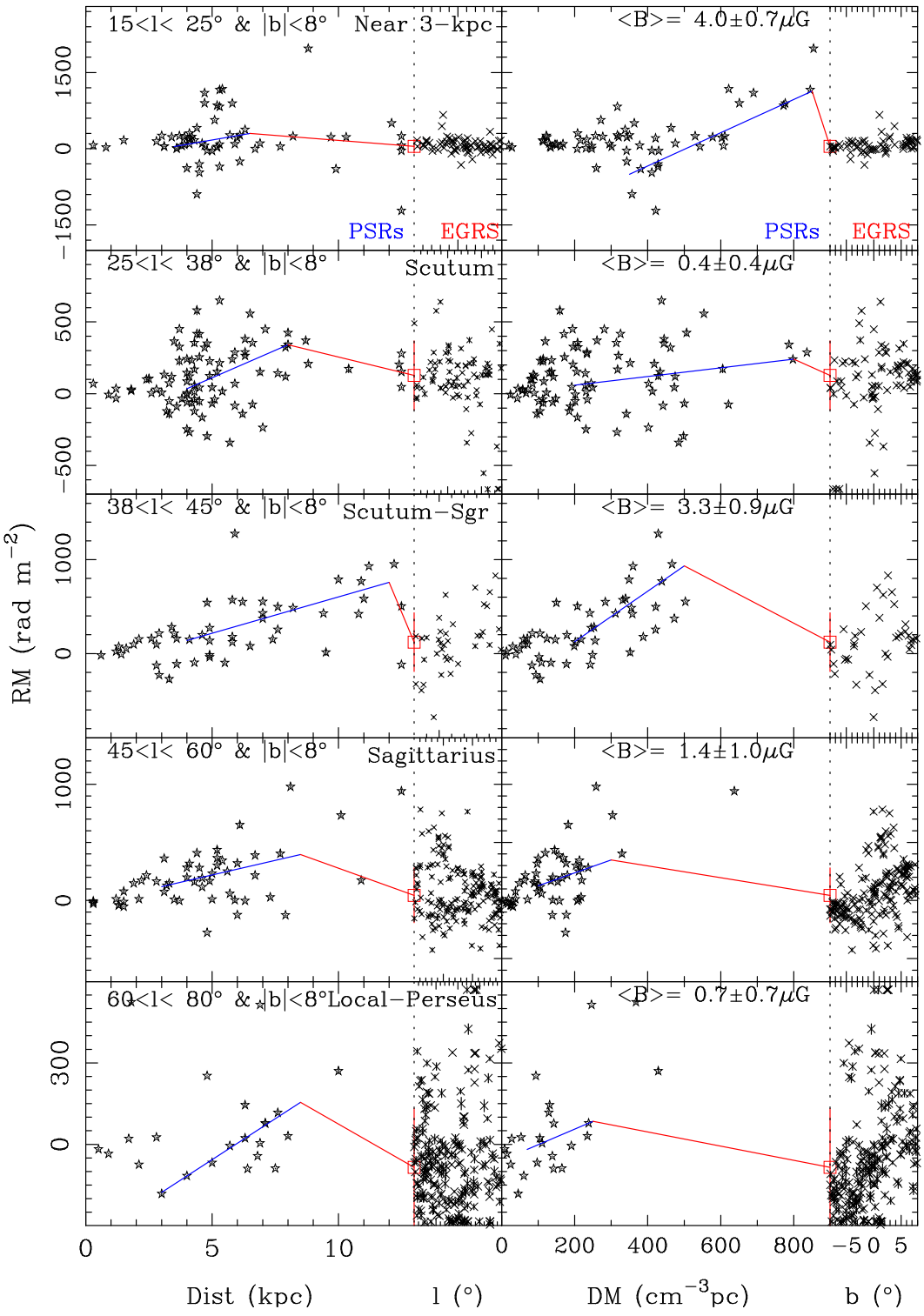

Figure 5. Same as Fig. 2 but for RMs for pulsars and EGRS in the first Galactic quadrant. Positive slopes in the RM – DM plots indicate counter-clockwise fields.

It is well established that the Galactic magnetic field in the local region is clockwise (Manchester 1974; Thomson & Nelson 1980; Lyne & Smith 1989; Han & Qiao 1994; Rand & Lyne 1994; Weisberg et al. 2004), implying a reversal between the local interarm region and the Carina – Sagittarius arm. This local clockwise field is confirmed by the decreasing RMs of pulsars with distance and DM in the subplot in Figure 6 for the region of $80° < l < 120°$ and the increasing RMs in the subplots for the regions of $190° < l < 250°$ and $250° < l < 270°$, that is, Local Q1–Q2, Local Q3–Q4 and also Outer-Q3, where pulsars are nearer than or just within the Perseus arm (see Figure 1). We therefore conclude

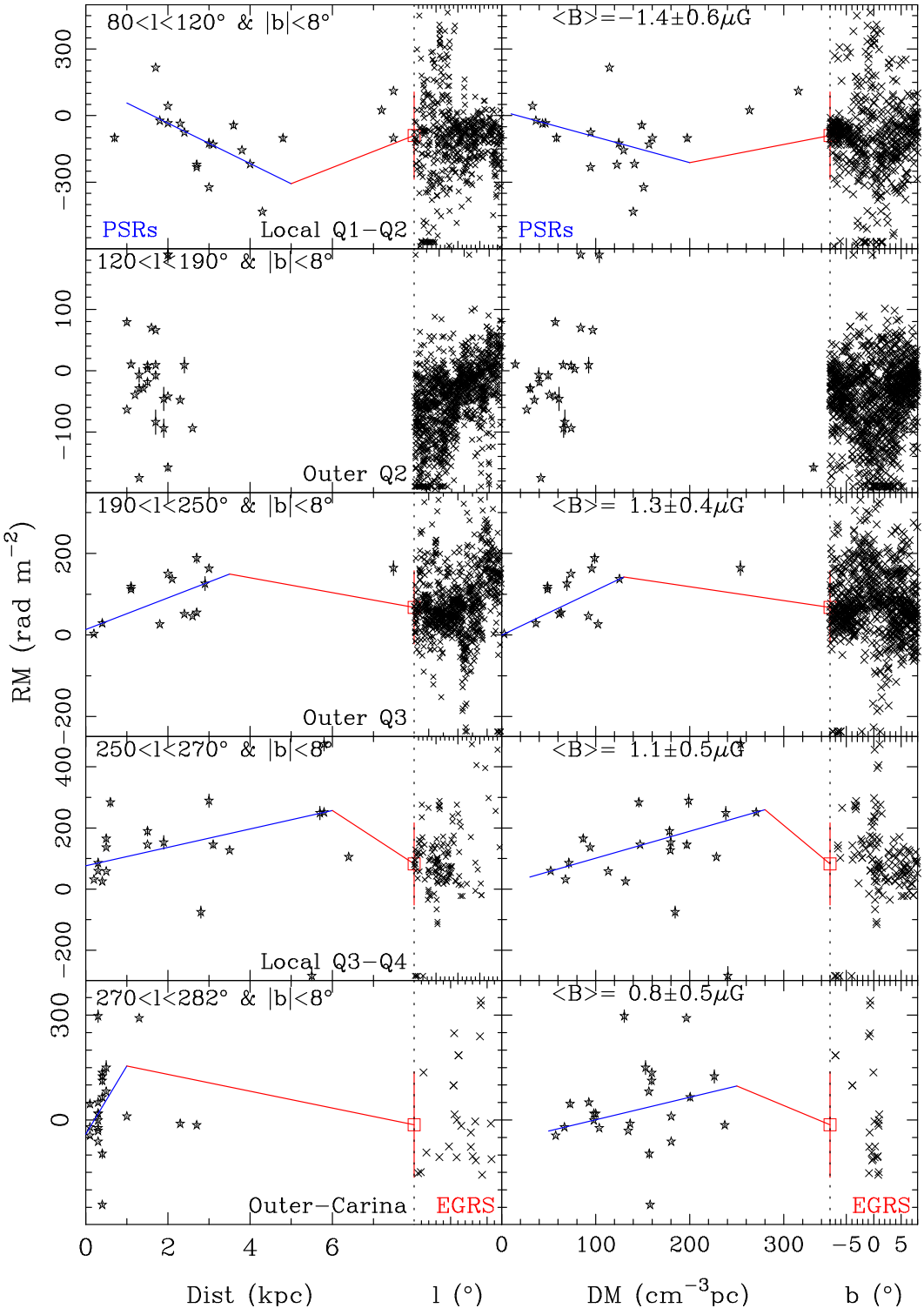

Figure 6. Same as Fig. 2 but for RMs for pulsars and EGRS in the outer Galactic zone. For this figure, the blue lines represent linear fits to the change in RM for most of the known pulsars in each zone. Postive slopes in the RM – DM plots indicate counter-clockwise fields for $l < 180°$ and clockwise fields for $l > 180°$.

that the clockwise fields are dominant in the Carina – Perseus interarm zone, including the Local Arm region.

Comparison of RMs of pulsars and EGRS gives some evidence for counter-clockwise fields probably associated with the Perseus arm. First of all, as seen in Figure 6, in the region of $80° < l < 120°$, pulsars show a systematic trend for RM decreasing. If there is no field reversal in the Perseus arm or outside, the RMs of EGRS are expected to be more negative. However, the data show that this is not the case. More positive RMs are observed for not only three

distant pulsars ($D > 6$ kpc) but also EGRS on average. A field reversal is also indicated by comparing the otherwise unexpected smaller RMs of EGRS in the outer regions of $190° < l < 250°$ and $250° < l < 270°$ with the increasing RMs of pulsars.

In the longitude region of $270° < l < 282°$, random but predominantly positive RMs are observed for the local pulsars within 1 kpc, but RMs of EGRS are mostly negative which is probably an indication of counterclockwise fields in the Perseus arm implying a reversal from the local interarm field. If there were no field reversal and the Perseus-arm fields were clockwise, the RMs of distant pulsars and EGRS would be dominated by these clockwise fields and should be positive and increasing with distance. We do not have RMs of more distant pulsars, but the RMs of EGRS are consistent with reversed fields in the Perseus arm.

It is difficult to probe the large-scale structure of the magnetic field in the anti-center region of our Galaxy (e.g. in the region of $120° < l < 190°$) using Faraday rotation since the uniform field tends to be perpendicular to the line of sight so that irregular field fluctuations can significantly influence the measured $B_{||}$. The RMs of pulsars in the Outer Q2 region are therefore more or less random.

Within the limitations imposed by uncertain distances, especially for the pulsar – EGRS regions, the field pattern illustrated in Figure 4 is consistent with our main conclusion, viz., that Galactic disk magnetic fields are predominantly counter-clockwise in spiral arms and clockwise in interarm regions, implying field reversals at each arm-interarm boundary. As is discussed further in the next section, this contrasts with the field patterns derived solely from EGRS RMs which generally have just one major region of clockwise field encompassing the whole Carina – Perseus region.

4. MODELING THE GALACTIC DISK MAGNETIC FIELD

Figure 4 shows the derived field directions listed in Table 1. In general according to the analysis above, counter-clockwise fields exist in the spiral arms and clockwise fields in the interarm regions. Comparison of extra-galactic RMs with distant pulsar RMs often indicate further reversals of field direction in the outer Galaxy. Because of the uncertain electron density, it is not possible to obtain quantitative estimates of $B_{||}$ in the regions beyond pulsars.

For the many applications where the strength and form of the Galactic magnetic field is important, it is useful to construct a simple model that can reflect the field reversals we discussed above for the Galactic disk and be used to estimate the large-scale field at a given Galactic location. Since we have only analysed the low-latitude RMs in this paper, our model just describes the structure of the Galactic disk field. A full three-dimensional model is left for future work.

Our model for the Galactic disk field assumes logarithmic spiral fields of pitch angle $\psi = 11°$ (Hou & Han 2014) with a radial and z dependence given by:

$$B(R, z) = B_0 \exp(-R_G/A) \exp(-|z|/H) \tag{3}$$

where R_G is the Galactocentric radial distance, A is the disk radial scale and H is the disk scale height. The field strength $B_0 = B_s(i)$ for $R_s(i) < R_0 < R_s(i+1)$, where $R_s(i)$ and $B_s(i)$ are given in Table 5 and R_0 is defined by

$$R_0 = R_G \exp(-\psi \tan\theta) \tag{4}$$

where θ is the azimuth angle measured counterclockwise from the $+y$ axis, which points from the Galactic center to the Sun. For $R_G < R_s(1)$ and $R_G > 15$ kpc, we set $B_0 = 0$.

Table 5. Radial zones for the model spiral disk field. Positive values of B_s correspond to counter-clockwise fields and negative values to clockwise fields, as viewed from the north Galactic pole.

Index i	1	2	3	4	5	6	7
$R_s(i)$ (kpc)	3.0	4.1	4.9	6.1	7.5	8.5	10.5
$B_s(i)$ (μG)	4.5	−3.0	6.3	−4.7	3.3	−8.7	–

This field structure matches most of the field reversals we observe, and the values of $B_s(i)$ are generally consistent with the $\langle B \rangle$ values obtained from the gradients of the RM – DM fits in Figures 2 – 6, taking into account the location

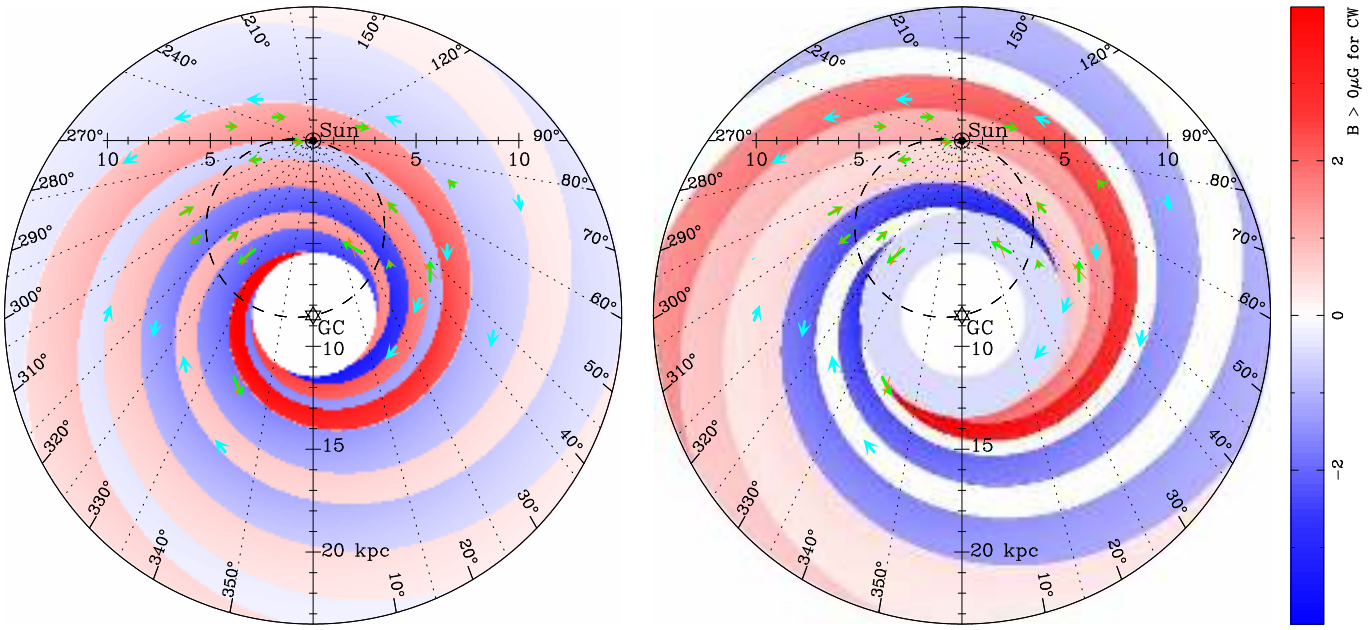

Figure 7. Left panel: Model for large-scale magnetic fields in the Galactic disk. Blue shading represents counter-clockwise fields and pink shading represents clockwise fields according to the bar on the right side of the figure. The arrows represent the inferred spiral field directions as shown in Figure 4. Right panel: The model of JF12 for large-scale magnetic fields in the Galactic disk based on RMs of EGRS and the Galactic synchrotron emission. The arrows are the same as in the left panel.

of the tangential point in Galactocentric radius and azimuth. The scale height of the disk field, H, was taken to be 0.4 kpc (cf., Jansson & Farrar 2012) and the radial scale, A, was taken to be 5.0 kpc. The model field is illustrated in the left panel of Figure 7. The right panel of Figure 7 shows the Galactic disk field model of Jansson & Farrar (2012) (JF12) which is primarily based on RMs of EGRS.

The new model, based on a combination of pulsar RMs and EGRS RMs, has between six and eight field reversals along a radial line from the Galactic Center, depending on the longitude. In contrast, the JF12 model of has clockwise disk fields across the whole Sagittarius – Carina region and no clockwise field in the Crux – Norma interarm region (tangential at $l = 320°$). As a consequence of this, there are only one or two reversals along radial lines from the Galactic Center. The clockwise field in the Crux – Norma tangential direction is clearly indicated by the positve pulsar RMs in this zone as shown in Figure 3. Similarly, the pulsar RMs shown in Figure 5 clearly show the presence of counter-clockwise fields in the Sagittarius tangential region as discussed above in §3.2.

To compare how well these two models "predict" the EGRS RMs, we compute the RM of each EGRS source in Figure 1 using both the NE2001 electron density model (Cordes & Lazio 2002), as used by JF12, and the more recent YMW16 model (Yao et al. 2017). In Figure 8 we show the distribution of observed EGRS RMs in Galactic latitude and longitude, along with the RMs computed using our model for the disk field, which is based on both pulsar and EGRS RMs, and from the JF12 model which is based on just the EGRS RMs. The RM median values for every 5° of Galactic longitude are compared in the lower two sub-panels. This figure demonstrates that, despite its different structure and different basis, our model predicts RMs of EGRS more accurately than the JF12 model which is based primarily on them, for example, in the region $270° \geq l \geq 280°$. With the YMW16 electron density model (Yao et al. 2017), the weighted mean difference between the median observed RMs and median predicted RMs is smaller for our model in all quadrants. Even with the NE2001 model, our model is significantly better than predictions based on the JF12 model for the first and fourth quadrants (i.e., top panel of Figure 8).

However, the converse is not true. For example, as shown in the right panel of Figure 7, the EGRS-based model does not correctly model the clockwise fields in the Crux-Norma interarm region or the counter-clockwise fields in the Sagittarius-Carina arm. With their distribution through the Galactic disk at approximately known distances enabling tomographic mapping, pulsars are able to reveal reversals in the large-scale disk field that are concealed in the RMs of EGRS since they integrate across the entire disk. Despite the large number of EGRS RMs in the outer regions of our Galaxy (i.e. within $l = 180° \pm 90°$), the field structure is not well constrained without comparison with the RMs of foreground pulsars. Even though the number of pulsar RMs is relatively small compared to that of EGRS RMs, the pulsar RMs are a very powerful tool in investigations of the large-scale Galactic magnetic field.

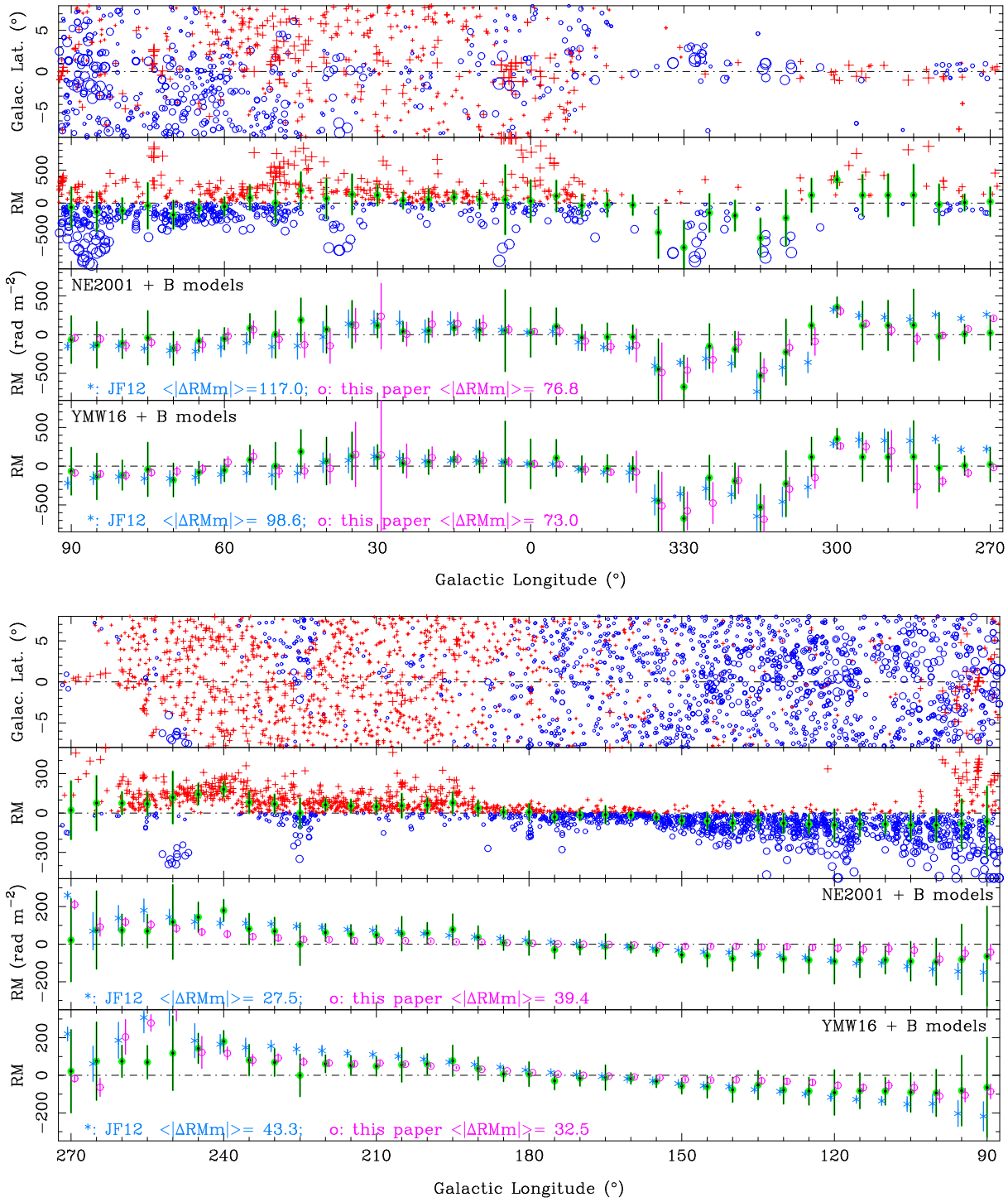

Figure 8. Distribution of RMs of EGRS with Galactic longitude, within $l = 0° \pm 90°$ in the upper panel and $l = 180° \pm 90°$ in the lower panel. For each panel, the top sub-panel shows the distribution of EGRS RMs in b, with blue circles representing RMs < 0 and red + signs representing RMs > 0, with the symbol size proportional to $|RM|^{1/2}$. The second sub-panel gives the RM magnitudes and their median values for every 5° of Galactic longitude, with error bars representing the standard deviation from the median in the 5° interval centered on the point. Where there were less than five RMs in the interval (primarily in Quadrant 4), the interval was extended (by steps of 2°) to encompass more than five points to give a realistic median and deviation. In the lower two sub-panels, the green points with error bars are as in the second panel, the pink circles and bars are the median values of the RMs computed for each source using the model for the disk field presented in this paper and the blue asterisks and bars are those computed using the JF12 model, for the NE2001 electron density model (Cordes & Lazio 2002) and the YMW16 model (Yao et al. 2017), respectively. The model points and bars are slightly offset for clarity. Mean absolute differences between the median observed RMs and median predicted RMs weighted by the rms deviation of the observed RMs, $\langle|\Delta RM_m|\rangle$, is given for each field model and each electron density model in the lower sub-panels.

5. CONCLUSIONS

We have measured rotation measures for 477 pulsars of which 441 are either new or improved over previous measurements. By analyzing the distribution of pulsar RMs and comparing RMs for pulsars and extra-galactic radio sources (EGRS) lying within 8° of the Galactic Plane, we show that the large-scale disk field in the inner Galaxy probably has a bisymmetric form with reversals between spiral arm and interarm regions. Compared to the analysis in Han et al. (2006), we have a larger sample of pulsar RMs and have combined pulsar and EGRS data to show the reversals in the Galactic disk large-scale field more clearly. Most of these reversals are not apparent in EGRS RM measurements since these average over the whole path inside our Galaxy. Furthermore, pulsar RM and DM data can give direct measurements of the mean magnetic field strength in selected regions of the Galaxy, for example, zones around tangential points.

Based on these results, we present a quantitative model for the large-scale magnetic field in the Galactic disk, which not only models the spiral magnetic field reversals between arm and interarm regions, but also can reproduce the RM distribution of EGRS better than a recent model based on EGRS data alone.

In the future, more pulsar RMs and improved pulsar distances will become available, allowing the large-scale structure of the Galactic magnetic fields to be better constrained. More RMs of EGRS, particularly in the longitude zone from 260° to 350° can help to determine the magnetic field structure beyond the pulsars. Observations of higher-latitude RMs for both pulsars and EGRS may in future allow construction of a complete three-dimensional model of the large-scale Galactic magnetic field, which is a proposed project for the SKA (see e.g., Han et al. 2015).

ACKNOWLEDGMENTS

We sincerely thank Dr. Jun Xu for help on construction of the models for the disk magnetic field, and Dr. LiGang Hou for help on the background spiral images. JLH is supported by the Key Research Program of the Chinese Academy of Sciences (Grant No. QYZDJ-SSW-SLH021) and the National Natural Science Foundation (No. 11473034). The Parkes radio telescope is part of the Australia Telescope which is funded by the Commonwealth Government for operation as a National Facility managed by the Commonwealth Scientific and Industrial Research Organisation. The National Radio Astronomy Observatory is a facility of the National Science Foundation operated under cooperative agreement by Associated Universities, Inc.

REFERENCES

Baars, J. W. M., Genzel, R., Pauliny-Toth, I. I. K., & Witzel, A. 1977, A&A, 61, 99
Battaner, E., & Florido, E. 2007, Astronomische Nachrichten, 328, 92
Beck, R. 2015, A&A, 578, A93
Beck, R., Brandenburg, A., Moss, D., Shukurov, A., & Sokoloff, D. 1996, ARA&A, 34, 155
Beck, R., Shukurov, A., Sokoloff, D., & Wielebinski, R. 2003, A&A, 411, 99
Bennett, C. L., Larson, D., Weiland, J. L., et al. 2013, ApJS, 208, 20
Beuermann, K., Kanbach, G., & Berkhuijsen, E. M. 1985, A&A, 153, 17
Bilitza, D., & Reinisch, B. W. 2008, Adv. Space Res., 42, 599
Boulares, A., & Cox, D. P. 1990, ApJ, 365, 544
Brown, J. C., Haverkorn, M., Gaensler, B. M., et al. 2007, ApJ, 663, 258
Brown, J. C., Taylor, A. R., & Jackel, B. J. 2003, ApJS, 145, 213
Clemens, D. P., Pinnick, A. F., Pavel, M. D., & Taylor, B. W. 2012, ApJS, 200, 19
Cordes, J. M., & Lazio, T. J. W. 2002, ArXiv:astro-ph/0207156, arXiv:astro-ph/0207156
Crutcher, R. M. 1999, ApJ, 520, 706
Demorest, P. B. 2007, PhD thesis, University of California, Berkeley
Ferdman, R. D., Stairs, I. H., Backer, D. C., et al. 2004, AAS Abstracts, 205, 111.01
Fermi, E. 1949, Phys. Rev., 75, 1169
Force, M. M., Demorest, P., & Rankin, J. M. 2015, MNRAS, 453, 4485
Hamilton, P. A., Hall, P. J., & Costa, M. E. 1985, MNRAS, 214, 5P
Hamilton, P. A., & Lyne, A. G. 1987, MNRAS, 224, 1073
Hamilton, P. A., McCulloch, P. M., Manchester, R. N., Ables, J. G., & Komesaroff, M. M. 1977, Nature, 265, 224
Han, J. L. 2017, Ann. Rev. Astr. Ap., 55, 111
Han, J. L., Demorest, P. B., van Straten, W., & Lyne, A. G. 2009, ApJS, 181, 557
Han, J. L., Manchester, R. N., Berkhuijsen, E. M., & Beck, R. 1997, A&A, 322, 98
Han, J. L., Manchester, R. N., Lyne, A. G., Qiao, G. J., & van Straten, W. 2006, ApJ, 642, 868
Han, J. L., Manchester, R. N., & Qiao, G. J. 1999, MNRAS, 306, 371
Han, J. L., & Qiao, G. J. 1994, A&A, 288, 759
Han, J. L., van Straten, W., Lazio, T. J. W., et al. 2015, Advancing Astrophysics with the Square Kilometre Array (AASKA14), 41
Hankins, T. H., & Rankin, J. M. 2010, AJ, 139, 168
Heiles, C. 1996, ApJ, 462, 316
Hotan, A. W., van Straten, W., & Manchester, R. N. 2004, PASA, 21, 302
Hou, L. G., & Han, J. L. 2014, A&A, 569, A125
Indrani, C., & Deshpande, A. A. 1999, New Astr., 4, 33
Jansson, R., & Farrar, G. R. 2012, ApJ, 757, 14
Johnston, S., Hobbs, G., Vigeland, S., et al. 2005, MNRAS, 364, 1397

Johnston, S., Kramer, M., Karastergiou, A., et al. 2007, MNRAS, 381, 1625
Kerr, M., Hobbs, G., Shannon, R. M., et al. 2014, MNRAS, 445, 320
Kiepenheuer, K. O. 1950, Physical Review, 79, 738
Lyne, A. G., & Smith, F. G. 1989, MNRAS, 237, 533
Manchester, R. N. 1972, ApJ, 172, 43
Manchester, R. N. 1974, ApJ, 188, 637
Manchester, R. N., & Han, J. L. 2004, ApJ, 609, 354
Manchester, R. N., Hobbs, G. B., Teoh, A., & Hobbs, M. 2005, AJ, 129, 1993
Manchester, R. N., Hobbs, G., Bailes, M., et al. 2013, PASA, 30, 17
Men, H., Ferrière, K., & Han, J. L. 2008, A&A, 486, 819
Navarro, J., Manchester, R. N., Sandhu, J. S., Kulkarni, S. R., & Bailes, M. 1997, ApJ, 486, 1019
Nota, T., & Katgert, P. 2010, A&A, 513, A65+
Noutsos, A., Johnston, S., Kramer, M., & Karastergiou, A. 2008, MNRAS, 386, 1881
Noutsos, A., Sobey, C., Kondratiev, V. I., et al. 2015, ArXiv e-prints, arXiv:ArXiv:1501.03312
Novak, G., Chuss, D. T., Renbarger, T., et al. 2003, ApJ, 583, L83
Ordog, A., Brown, J. C., Kothes, R., & Landecker, T. L. 2017, ArXiv:1704.08663, arXiv:1704.08663
Planck Collaboration, Adam, R., Ade, P. A. R., et al. 2016a, A&A, 594, A1
Planck Collaboration, Ade, P. A. R., Aghanim, N., et al. 2016b, A&A, 586, A138
Press, W. H., Teukolsky, S. A., Vetterling, W. T., & Flannery, B. P. 1996, Numerical Recipes in Fortran 77: The Art of Scientific Computing, 2^{nd} edition (Cambridge: Cambridge University Press)
Pshirkov, M. S., Tinyakov, P. G., Kronberg, P. P., & Newton-McGee, K. J. 2011, ApJ, 738, 192
Qiao, G. J., Manchester, R. N., Lyne, A. G., & Gould, D. M. 1995, MNRAS, 274, 572
Ramachandran, R., Backer, D. C., Rankin, J. M., Weisberg, J. M., & Devine, K. E. 2004, ApJ, 606, 1167
Rand, R. J., & Kulkarni, S. R. 1989, ApJ, 343, 760
Rand, R. J., & Lyne, A. G. 1994, MNRAS, 268, 497
Rees, M. J. 1987, QJRAS, 28, 197
Simard-Normandin, M., & Kronberg, P. P. 1980, ApJ, 242, 74
Sofue, Y., & Fujimoto, M. 1983, apj, 265, 722
Staveley-Smith, L., Wilson, W. E., Bird, T. S., et al. 1996, PASA, 13, 243
Sun, X.-H., & Reich, W. 2010, Res. Astron. Astrophys., 10, 1287
Sun, X. H., Reich, W., Waelkens, A., & Enßlin, T. A. 2008, A&A, 477, 573
Taylor, A. R., Stil, J. M., & Sunstrum, C. 2009, ApJ, 702, 1230
Taylor, J. H., Manchester, R. N., & Lyne, A. G. 1993, ApJS, 88, 529
Thomson, R. C., & Nelson, A. H. 1980, MNRAS, 191, 863
Tiburzi, C., Johnston, S., Bailes, M., et al. 2013, MNRAS, 436, 3557
Vallée, J. P. 1996, A&A, 308, 433
—. 2005, ApJ, 619, 297
Van Eck, C. L., Brown, J. C., Stil, J. M., et al. 2011, ApJ, 728, 97
van Ommen, T. D., D'Alesssandro, F. D., Hamilton, P. A., & McCulloch, P. M. 1997, MNRAS, 287, 307
Vlemmings, W. H. T. 2008, A&A, 484, 773
Weisberg, J. M., Cordes, J. M., Kuan, B., et al. 2004, ApJS, 150, 317
Weltevrede, P., & Johnston, S. 2008, MNRAS, 391, 1210
Wu, Q., Kim, J., & Ryu, D. 2015, New Astron., 34, 21
Wu, Q., Kim, J., Ryu, D., Cho, J., & Alexander, P. 2009, ApJ, 705, L86
Xu, J., & Han, J.-L. 2014, Res. Astron. Astrophys., 14, 942
Yan, W. M., Manchester, R. N., van Straten, W., et al. 2011, MNRAS, 414, 2087
Yao, J. M., Manchester, R. N., & Wang, N. 2017, ApJ, 835, 29

Draft version December 6, 2017
Preprint typeset using LaTeX style emulateapj v. 12/16/11

"RED" BUT NOT "DEAD": ACTIVELY STAR-FORMING BRIGHTEST CLUSTER GALAXIES AT LOW REDSHIFTS

James Runge[†] and Haojing Yan[‡]
Department of Physics and Astronomy, University of Missouri - Columbia
Draft version December 6, 2017

ABSTRACT

Brightest Cluster Galaxies (BCGs) are believed to have assembled most of their stars early in time and, therefore, should be passively evolving at low redshifts and appear "red-and-dead." However, there have been reports that a minority of low-redshift BCGs still have ongoing star formation rates (SFR) of a few to even $\sim$100 $M_\odot/yr$. Such BCGs are found in "cool-core" ("CC") clusters, and their star formation is thought to be fueled by "cooling flow." To further investigate the implications of low-redshift, star-forming BCGs, we perform a systematic search using the 22μm data ("W4" band) from the Wide-field Infrared Survey Explorer (WISE) on the GMBCG catalog, which contains 55,424 BCGs at $0.1 \lesssim z \lesssim 0.55$ identified in the Sloan Digital Sky Survey (SDSS). Our sample consists of 389 BCGs that are bright in W4 ("W4BCGs"), most being brighter than 5 mJy. While some ($\lesssim$ 20%) might host AGN, most W4BCGs should owe their strong mid-IR emissions to dust-enshrouded star formation. Their median total IR luminosity (L_{IR}) is $5 \times 10^{11} L_\odot$ (SFR $\sim$50 $M_\odot/yr$), and 27% of the whole sample has $L_{IR} > 10^{12} L_\odot$ (SFR >100 $M_\odot/yr$). Using ten W4BCGs that have *Chandra* X-ray data, we show that seven of them are possibly in CC clusters. However, in most cases (five out of seven) the mass deposition rate cannot account for the observed SFR. This casts doubt to the idea that cooling flows are the cause of the star formation in non-quiescent BCGs.

Keywords: galaxy clusters, brightest cluster galaxy, galaxy evolution

1. INTRODUCTION

A Brightest Cluster Galaxy (BCG), as the name implies, resides within a galaxy cluster and is its brightest member. BCGs are among the most luminous and the most massive galaxies in the low-redshift universe, usually have little ongoing star formation, and are dominated by old stellar populations (e.g., Dubinski 1998). It is believed that they have assembled most of their stellar masses before $z \sim 3$ (e.g., De Lucia et al. 2006), and have been passively evolving ever since. For this reason, they are among the so-called "red-and-dead" galaxy population.

BCGs being largely quiescent in the low-redshift universe is consistent with the general picture of "downsizing" galaxy evolution (Cowie et al. 1996), where the bulk of the star formation activities in the universe shift from high mass galaxies to low mass ones as the universe evolves. On the other hand, it has been known for over a decade that some BCGs at low redshifts still exhibit significant star formation. Such BCGs are in "cool-core" clusters, whose intra-cluster medium (ICM) has a temperature gradient such that materials can be funneled to the central region where the BCGs reside and presumably can fuel the observed star formation (e.g., O'Dea et al. 2005; Vikhlinin et al. 2007; Santos et al. 2008; Fogarty et al. 2015; see also Donahue et al. 2015 for recent discussions). However, it is unclear what fraction of BCGs still have ongoing star formation.

In this paper, we present a systematic study of star-forming BCGs, using the data from the Sloan Digital Sky Survey (SDSS; York et al. 2000) and the Wide-field Infrared Survey Explorer (WISE; Wright et al. 2010). We make use of the GMBCG catalog of Hao et al. (2010), which is the largest BCG catalog available to date, and select those BCGs that potentially have strong ongoing star formation activities based on their properties in the mid-IR bands of WISE. Our goal is to shed new light to the understanding of star-forming BCGs as a whole: how rare they are, how high their star formation rates (SFRs) can be, whether they have different properties in other aspects as compared to the vast majority of BCGs that are quiescent, and whether residing in "cool-core" clusters is a satisfactory explanation to their SFRs.

This paper is organized as follows. In Section 2, we briefly describe the data that we use to select star-forming BCGs. The details of the selection process is given in Section 3, and these are followed by Section 4 where we show various diagnostics to separate AGN activity from star formation. In Section 5, we analyze a small subsample of star-forming BCGs that have archival X-ray data that allow us to address various questions regarding their connection to cool-core clusters. We present a discussion of our findings in Section 6, and a summary in Section 7.

Throughout this paper, we adopt the concordant ΛCDM cosmological model of $H_0 = 70$ Mpc^{-1}km s^{-1}, $\Omega_M = 0.27$, and $\Omega_\Lambda = 0.73$. All magnitudes are in AB system unless otherwise noted.

2. DATA

The critical data sets used to select star-forming BCGs are the SDSS-based GMBCG catalog and the WISE all-sky survey data. In particular, we adopt the "unblurred" version of the WISE data (also known as "unWISE") of Lang (2014) for this study. A small number of such selected BCGs also have far-IR (FIR) data from

[†] email: jmr24f@mail.missouri.edu
[‡] email: yanha@missouri.edu

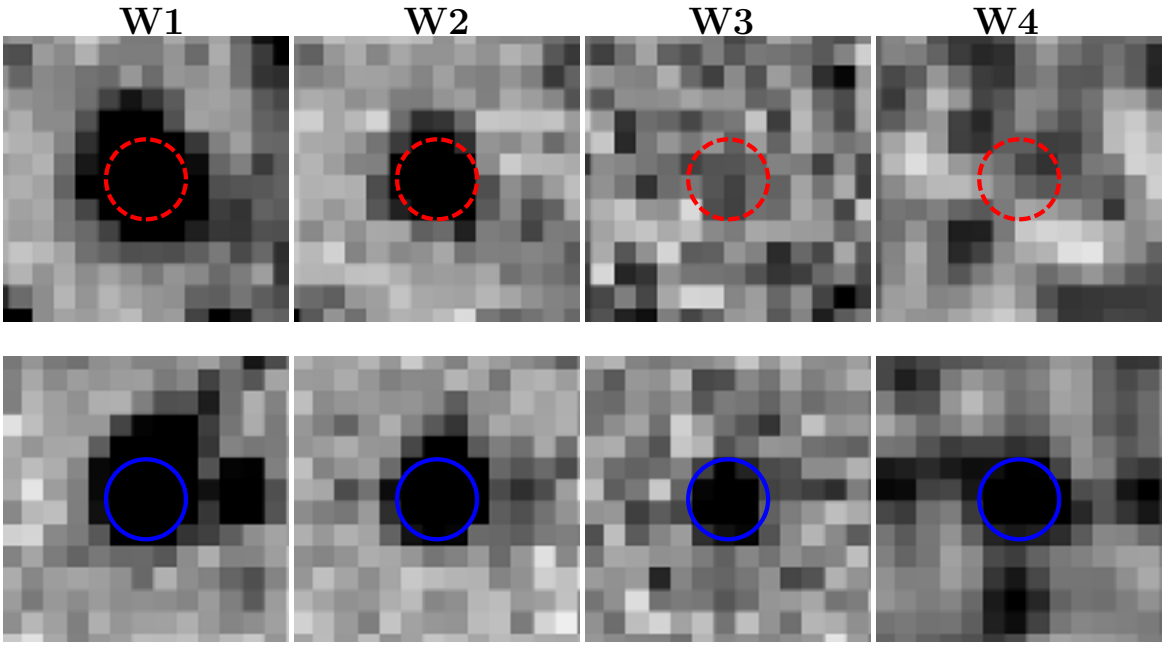

Figure 1. Examples showing WISE 4-band images of a BCG that is undetected in the W4 band (top) and one that is detected (bottom). These image cutouts are made from the unWISE products. The circles are centered on the reported SDSS positions, and are 10″ in radius.

Herschel or X-ray data from *Chandra*, which we used for further analysis. All these data are briefly described below.

2.1. *GMBCG Catalog*

The GMBCG Catalog (Hao et al. 2010) consists of 55,424 rich galaxy clusters found by using the Gaussian Mixture Brightest Cluster Galaxy (GMBCG) algorithm on the SDSS data in the seventh data release (DR7). This algorithm detects clusters by identifying the BCG and the red sequence galaxies in its vicinity and calculating the clustering strength, a measure of the surface density of cluster galaxies at the BCG position. Hao et al. (2010) apply this method to the Legacy Survey Area of SDSS DR7, which covers 7,300 deg^2 of the North Galactic Cap and 740 deg^2 from three stripes in the South Galactic Cap, and obtain their cluster catalog across the redshift range $0.1 \lesssim z \lesssim 0.55$.

This GMBCG catalog contains the positions of the identified BCGs along with their redshifts and photometry. The redshifts are either spectroscopic redshifts (∼20,000 objects) or photometric redshifts (see Hao et al. 2010 for details).

2.2. *WISE and unWISE*

The nominal WISE mission mapped the entire sky in 2010 in four near-to-mid-IR bands, namely, W1, W2, W3, and W4, whose central wavelengths are 3.4, 4.6, 12, and 22 μm, respectively. The spatial resolutions in these four bands are 6.1″, 6.4″, 6.5″, and 12.0″, respectively. The nominal 5σ limits in these bands are 0.068, 0.098, 0.86 and 5.4 mJy, respectively (Wright et al. 2010).

The offically released images of WISE ("AllWISE") were intentionally convolved by the point spread functions (PSFs) during the co-adding process. While this process is appropriate for isolated point sources, it reduces the resolution of the images and thus exacerbates the blending problem. To remedy this problem, unWISE[1] (Lang 2014) "un-blurs" these images to produce the final stacks that preserve the native spatial resolutions.

Along with the un-blurred images, unWISE also provides a catalog of WISE photometry based on "forced photometry" using ∼ 400 million SDSS DR10 objects as the morphological templates to fit the WISE source light profiles (Lang et al. 2014). Since the GMBCG catalog is based upon the same SDSS data (albeit in an earlier data release), all of our objects appear in the unWISE forced photometry catalog. Therefore, we adopted the unWISE images for visual verification and its forced photometry for quantitative analysis.

2.3. *Herschel data*

In order to further study the star formation properties of the selected BCGs, we also used the archival FIR data taken by the Spectral and Photometric Imaging Receiver (SPIRE; Griffin et al. 2010) on *Herschel* Space Observatory (Pilbratt et al. 2010). While only a small number of objects have these SPIRE data, they offer a valuable reference that we will detail in §4.3.

Specifically, we made use of the SPIRE three-band (250, 350 and 500 μm) photometry from the following *Herschel* very wide-field surveys whose SPIRE data are now publicly available, namely, the *Herschel* Multi-tiered Extragalactic Survey (HerMES; Oliver et al. 2012; Roseboom et al. 2010; Smith et al. 2012; Viero et al. 2013; Wang et al. 2014), the *Herschel* Stripe 82 Survey (HerS; Viero et al. 2014) and the *Herschel* Astrophysical Terahertz Large Area Survey (H-ATLAS; Eales et al. 2010; Valiante et al. 2016). Both HerMES and H-ATLAS have catalogs available that include flux measurements. For the HerS data, we measured the source flux on the SPIRE images using HIPE (Ott 2010) following the procedure for source extraction and photometry outlined in

[1] http://unwise.me

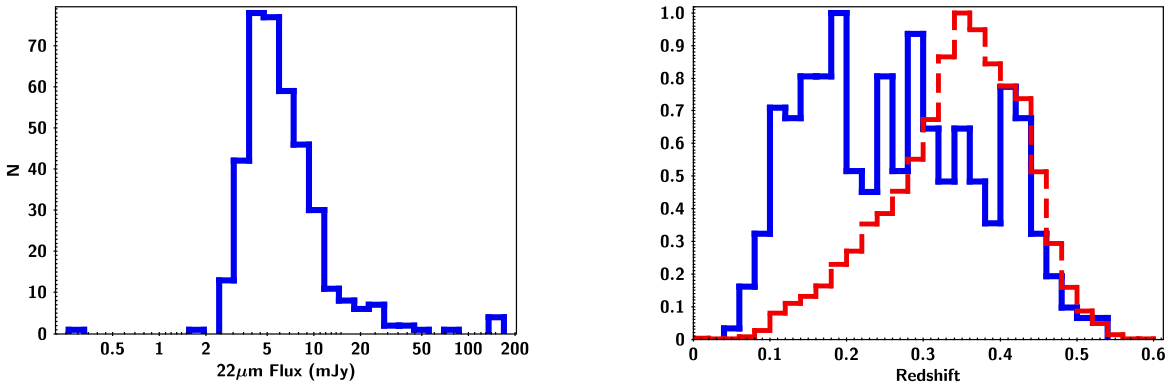

Figure 2. Left: W4 (22 µm) flux density distribution of the W4-detected BCGs (W4BCGs). Right: Normalized redshift distribution for the entire GMBCG catalog (red dashed line) and the subset of W4BCGs (blue solid line).

the SPIRE data manual[2]. In total, these surveys cover 340 deg^2.

2.4. *Chandra Data*

In order to investigate possible cool-core properties of our sample, X-ray data is necessary. Therefore, we used the public *Chandra* X-ray data provided by the Chandra Data Archive. Both Primary and Secondary products were retrieved for each available observation. These data provide a spatial resolution of 0.5″ and cover an energy range of 0.1-10 keV.

Standard data processing was carried out starting from the level 1 event files using `CIAO` 4.8.2 (Fruscione et al. 2006) with CALDB 4.7.0 of the *Chandra* Calibration Database. The reprocessing script *chandra_repro* was used to reprocess the data and create level 2 event files. When observations were taken in the VFAINT mode, the parameter *check_vf_pha* was set to "yes" in order to remove background events likely caused by cosmic rays. Background estimates were taken in the same field away from the central X-ray peak and clear of any other X-ray sources.

For X-ray spectra, we followed a procedure similar to that of Molendi et al. 2016 (hereafter Mol16). The X-ray spectra for the BCG were processed from the level 2 event files using *specextract* in `CIAO`. A 40 kpc region centered on the BCG was chosen for the extraction. There could be a complication in this analysis if the BCG is an X-ray AGN, in which case the X-ray spectrum might be dominated by the AGN rather than the heated ICM. To solve this potential problem, we performed a separate analysis by following Mol16 and masking the central region. Unlike in Mol16 where a circular region of 2″ in radius is masked, we chose to only mask out the inner 2 kpc of the BCG, as choosing a global value of 2″ would result in masking out the bulk of X-ray flux for some of our sources. Background spectra were also processed at up to three different regions away from the X-ray peak and any other X-ray sources.

3. SAMPLE OF BCGS WITH STRONG MID-IR EMISSION

We searched for BCGs with ongoing star formation by identifying those that have secure mid-IR detections in the WISE W4-band at 22 μm. This will reveal dust-embedded star formation in BCGs, and thus is complementary to the method that aims at identifying unobscured star formation through UV emissions, such as some of those reported by Donahue et al. (2015). Here we describe our sample in detail.

3.1. *Initial Selection*

To construct a catalog of possible sources that have W4 detection, the GMBCG catalog was cross-matched with the unWISE forced photometry catalog using a matching radius of 5″, which is slightly less than half the spatial resolution of W4. We further required that a matched object should have $S/N \geq 5$ in W4 as reported in the unWISE SDSS forced photometry catalog. This resulted in 1,323 BCGs in our initial sample.

To ensure the sample robustness, we visually inspected the images of all these initial candidates. We found that a large number of the reported W4-detections were actually false-positives due to various reasons, such as image defects, noise spikes, artifacts produced by a bright neighbor, etc. After rejecting these contaminators, 458 BCGs survived. As an example, Fig. 1 shows the WISE image stamps of one that is not detected in W4 and one with a real W4-detection.

3.2. *Sample Verification*

Obviously, W4-detected BCGs are only a small fraction of the entire GMBCG sample. Therefore, we must consider possible contamination to the GMBCG sample, or in other words, whether these W4-detected objects derived from the GMBCG sample are BCGs at all. To address this question, we further verified the legitimacy of these 458 candidate objects on a one-by-one basis. This verification was to decide whether a candidate is in a cluster environment, and if yes, whether it is the BCG of the cluster. Our intention was not to invent a new cluster finding algorithm, but to perform an independent "sanity check" on the claimed BCGs.

The verification consisted of two steps. First, we worked under the assumption that the photometric redshifts that the GMBCG catalog relies on are accurate enough for its purpose. We used the SDSS DR7 data, the same as what the GMBCG catalog is based. For each candidate BCG, we retrieved the objects within a

[2] http://herschel.esac.esa.int/hcss-doc-12.0/

$3'$ radius around it, and retained only those whose photometric redshifts (as reported in the SDSS DR7) were within ± 0.02 of the redshift of the candidate BCG (as quoted in the GMBCG catalog and is the same as in the SDSS DR7). The retained objects were considered as the members of the candidate cluster. This redshift range was adopted because it is the reported accuracy (1σ) of the SDSS DR7 photometric redshifts. We then constructed the i vs. $(g-r)$ color-magnitude diagram, and checked whether we could see a "ridge line" indicative of a red sequence. If a red sequence was seen, we checked whether the current candidate BCG was the correct identification of BCG, i.e., whether it was the brightest one (in i-band) among all members.

After this step, we confirmed that 383 objects survived. Among the 75 dubious cases, four could hardly be called clusters because they only had a few members (< 8), and thus must be rejected. These four sources were at the high-redshift end of the catalog. One other case was a misidentification, and actually must be part of Abell 1689 (whose BCG is already in the W4BCG sample) and thus must also be removed. The other 70 objects were in clusters with a clear red sequence, however they were in fact not the BCGs. Therefore, we identified the "new" BCG for each of these 70 cases by finding the brightest member, and conducted all the previous steps reported above on these "new" BCGs. Of all these 70 objects, only six have reliable W4 detections. We included these six objects into our sample, and thus our final sample consists of 389 objects in total.

3.3. *General Properties and Subdivision of the Final Sample*

Fig. 2 shows the distributions of their W4 flux densities and redshifts. At these redshifts, the W4 emissions are still in the rest-frame mid-IR, and must be originated from heated dust instead of stellar continuum. These W4-detected BCGs (hereafter "W4BCGs") comprise a special population at odd with the general picture of BCGs that they are old, passively evolving galaxies. Therefore, we aim to understand the nature of these exceptions.

In order to investigate whether the occurrence of W4BCG could be dependent of the cluster richness, we divide our final W4BCG sample into two categories based on the reported GMBCG cluster richness ("N_{gals}^{scaled}") in Hao et al. (2010). We adopt $N_{gals}^{scaled} = 15$ as the criterion, and refer to those clusters with $N_{gals}^{scaled} \geq 15$ as "rich" clusters and those with $N_{gals}^{scaled} < 15$ as "poor" clusters. The rich clusters are 28% of the entire GMBCG sample, while the poor clusters make of 72%. The corresponding W4BCGs are subsequently divided into the W4BCG-R (108 objects, or 27.8% of the total 389 W4BCGs) and the W4BCG-P (281 objects, or 72.2%) subsamples, respectively.

4. DATA ANALYSIS

There are two possible causes to the heated dust emissions of these W4BCGs in the mid-IR, namely, active ongoing star formation or AGN activities. In this section, we investigate which of these two mechanisms is the more probable cause.

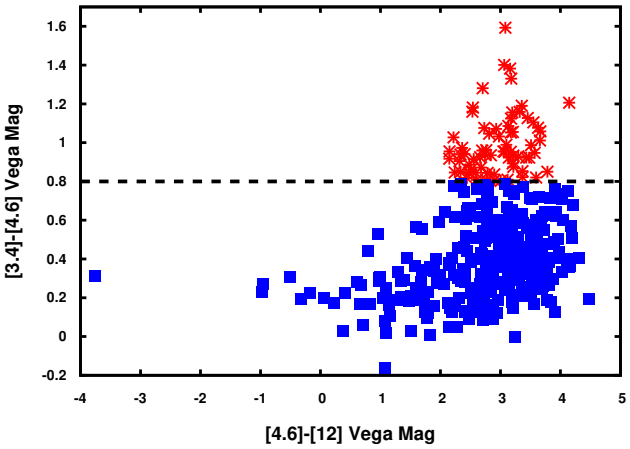

Figure 3. WISE color diagnostics of W4BCGs. The dashed line at $W1 - W2 = 0.8$ mag (Stern et al. 2012) separates AGN (red asterisks) and non-AGN (blue squares). Only 69 out of the total 389 W4BCGs are possible AGN hosts by this selection.

4.1. *Possible AGN Hosts*

To understand whether any of our W4BCGs could possibly host an AGN, we performed two diagnostics, which are based on the WISE color selection and the BPT diagram method, respectively. We note that being diagnosed as an AGN host by either method does not necessarily mean that the mid-IR emission in W4 must be dominated by AGN heating. However, if we do not find any AGN activity by either method, it is very plausible that the mid-IR emission is mainly driven by the heating of star formation.

4.1.1. *WISE Color Diagnostics*

Using a W1-W2 versus W2-W3 WISE color-color plot has been shown to be an effective method to identify AGN (Jarrett et al. 2011; Mateos et al. 2012; Stern et al. 2012; Assef et al. 2013). Furthermore, it has been demonstrated that a single color criterion of $W1 - W2 \geq 0.8$ mag (in Vega system) provides a robust selection of AGN (Stern et al. 2012; Assef et al. 2013). We adopted this latter method in our analysis, and the result is shown in Fig 3. We find that only 69 out of the total 389 W4BCGs and 12 of the 108 W4BCG-Rs satisfy this criterion (17.7% and 11.1% respectively), or in other words, most W4BCGs should be dominated by starbursts.

4.1.2. *BPT Diagram*

BPT diagrams are a set of diagnostic diagrams using emission lines to determine the ionization mechanism of nebular gas. The most commonly used diagram is [OIII]5007/Hβ versus [NII]6584/Hα (Baldwin, Phillips, & Terlevich 1981), which is what we used in our analysis. Various dividing curves have been proposed to separate AGN from star-forming galaxies (e.g. Kewley et al. 2001; Kauffmann et al. 2003a). The curve of Kauffmann et al. (2003a), which is shown in Eq. 1 below, is the most aggressive in selecting AGN, and hence we adopted this selection criterion in order to be conservative in attributing W4BCGs to starburst:

$$log([OIII]/H\beta) = 0.61/(log([NII]/H\alpha) - 0.05) + 1.3. \quad (1)$$

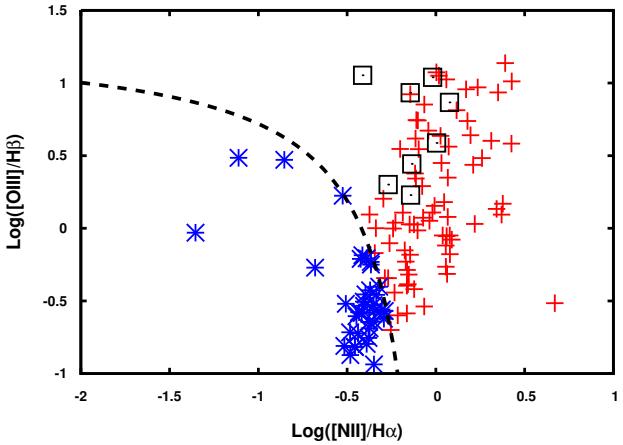

Figure 4. BPT diagnostics of W4BCGs. The dashed curve represents the criterion of Kauffman et al. (2003) that separates AGN-dominated objects (red pluses) and star-forming-dominated objects (blue asterisks). The black open squares (8 in total) indicate those that are also deemed to be AGN hosts based on the WISE color selection (see Fig. 3.)

For emission line measurements, we used the MPA-JHU(Max-Planck Institute for Astrophysics - John Hopkins University) "value-added" DR7 catalog of spectrum measurements (Brinchmann 2004; Kauffmann et al. 2003b; Tremonti et al. 2004) based on the SDSS DR7 data. A cross-match to the MPA-JHU catalog (within a radius of 5″ of the GMBCG reported position) resulted in 123 objects with emission line measurements for all four lines needed for the BPT diagnostic, which is shown in Fig 4. Within this subsample of 118 W4BCGs, 84 are deemed to host AGN (29 are W4BCG-R).

4.2. *Morphology*

The morphologies of the W4BCGs may provide additional information to reveal the nature of their mid-IR emissions. In particular, we are interested in understanding whether merger could be relevant, regardless of the exact heating source being AGN activities or star formation. For this purpose, the SDSS i' band images were examined. The W4BCGs were then divided into three different categories: "Merger", where a recent or ongoing merger is evident as shown by disturbed morphology; "Close Neighbor", where there is no clear sign of merger but there is at least one galaxy within 10″ (even though this could be due to projection by chance); and "Single", where there is no sign of merger and no other galaxies within 10″ to the SDSS depth. Some examples are shown in Fig. 5. We note that 10″ corresponds to 18–60 kpc at the redshifts of the W4BCGs.

The statistics are listed in Table 1, which shows that the majority of W4BCGs do not exhibit obvious merger properties. Therefore, it is safe to conclude that the mid-IR emission of a W4BCG is independent of whether it is interacting with others.

4.3. *Star Formation Rates*

The analysis above clearly shows that most W4BCGs are not AGN hosts, and hence their mid-IR emission can only come from dust heated by strong star formation. Again, this is contrary to the general picture that BCGs are "red-and-dead" galaxies that have ceased their star formation long ago. This also leads to the question whether the mid-IR emissions of those AGN-hosting W4BCGs are due to AGN heating at all, as our data currently available cannot provide an unambiguous answer. In this section, we attempt to derive the star formation rates of the W4BCGs as a whole, assuming that the AGN contribution to their mid-IR emissions is negligible. In our later discussion, we examine whether this assumption is reasonable.

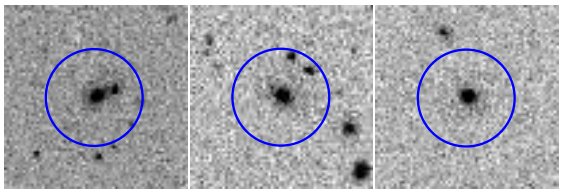

Figure 5. SDSS i' band images illustrating the different morphology subsets. Left: A BCG with obvious merger properties. Middle: A BCG with a neighbor within 10″ but no obvious merger properties. Right: A BCG with no other galaxies within a 10″ radius.

Table 1
Morphology of W4 detected BCGs based on SDSS i' images

Type	Count
Merger	69
Close Neighbor	145
Single	175

4.3.1. *SED Fitting*

A common method to derive IR-based SFR is to calculate the total IR luminosity (L_{IR}) over the conventional range of 8–1000 μm and then to infer the SFR by using the relation of Kennicutt (1998) as follows:

$$SFR[M_\odot/yr] = 1.0 \times 10^{-10} L_{IR}[L_\odot]. \quad (2)$$

We note that the coefficient in the above equation is after adjusting to a Chabrier (2003) initial mass function (IMF) and the derived SFR is a factor of 1.7 smaller than in case of using a Salpeter (1955) IMF.

L_{IR} can be calculated by fitting the spectral energy distributions (SEDs) to appropriate templates of dusty star forming galaxies (e.g., Chary & Elbaz 2001; Dale & Helou 2002; Siebenmorgen & Krügel 2007). In our case, W3 and W4 can be used for this purpose. We are also interested in the properties of the stellar populations in the W4BCGs, such as stellar mass and age, which can be derived by fitting the SEDs at the bluer wavelengths to stellar population synthesis models. Therefore, we utilized LePhare (Arnouts et al. 1999; Ilbert et al. 2006), which is capable of fitting both the stellar populations and the heated dust components at the same time.

Our input SEDs were constructed using the SDSS DR7 photometry in conjunction with the unWISE photometry (as described in §2.2) to cover the optical to mid-IR regime. The heated dust emission was fit to the template of Sibenmorgen & Krügel (2007; SK07), and the fit was confined to the W3 and W4 bands only. For the stellar component, the fit included the five SDSS bands as well as the W1 and W2 bands. LePhare treats the transition of stellar emission and heated dust emission in a consistent manner; i.e., the contribution of the dust emission template to the bands bluer than W3 (or that

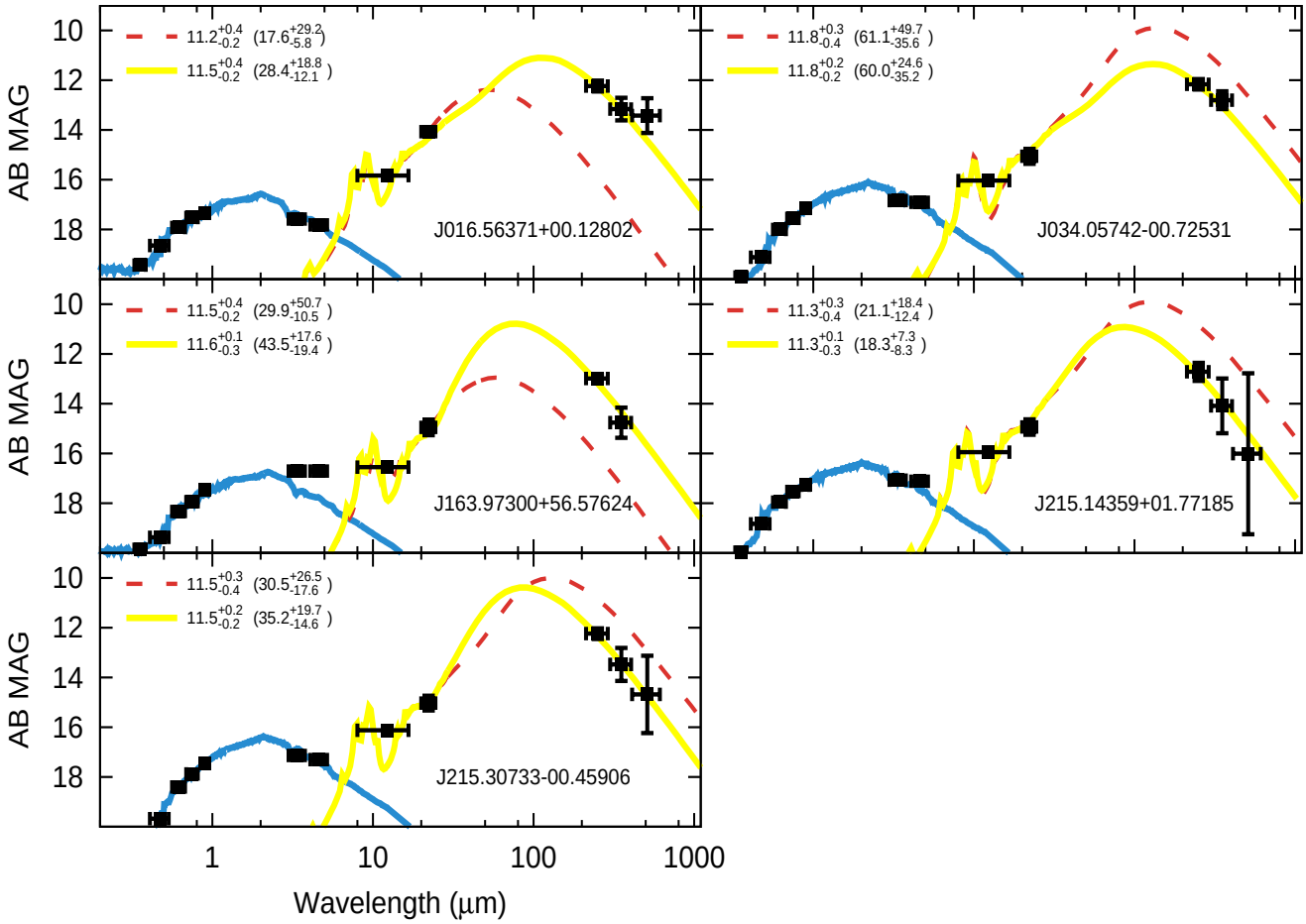

Figure 6. Spectral energy distributions of the subsample of five W4BCGs that have *Herschel* data. The fitting of their stellar populations (shown by the blue curve) is the same as in the other W4BCGs, which incorporates both the SDSS photometry in optical and W1 and W2 in near-IR (see text for details). Two fitting schemes in the mid-to-far-IR regime are shown: one only using WISE data (dashed red) and one including *Herschel* data (solid yellow). The blue curve shows the SED fitting results of the stellar populations, which incorporate the SDSS photometry in optical and the WISE near-IR photometry in W1 and W2. The $\log(L_{IR})$ value is displayed in the top left for each fitting along with the corresponding SFR (in $M_\odot$/yr) in parenthesis.

Table 2
Summary of the Subset with *Herschel* Data

GMBCG Catalog Name	250μm (mJy)	350μm (mJy)	500μm (mJy)	$\log(L_{IR}/L_\odot)$ No SPIRE	$SFR_{NoSPIRE}$ ($M_\odot$/yr)	$\log(L_{IR}/L_\odot)$ w/ SPIRE	SFR_{SPIRE} ($M_\odot$/yr)
W4BCG-R							
J034.05742-00.72531	49.57±5.92	27.54±5.40	–	$11.79^{+0.26}_{-0.38}$	$61.12^{+49.67}_{-35.60}$	$11.78^{+0.20}_{-0.23}$	$59.99^{+35.22}_{-24.56}$
W4BCG-P							
J016.56371+00.12802	46.39±5.84	19.81±4.81	15.50±5.42	$11.25^{+0.43}_{-0.17}$	$17.61^{+29.24}_{-5.82}$	$11.45^{+0.22}_{-0.24}$	$28.41^{+18.83}_{-12.15}$
J163.97300+56.57624	23.21±1.92	4.52±1.41	–	$11.48^{+0.43}_{-0.19}$	$29.88^{+50.69}_{-10.52}$	$11.64^{+0.15}_{-0.26}$	$43.51^{+17.55}_{-19.43}$
J215.14359+01.77185	29.79±5.93	8.43±4.15	1.43±1.23	$11.32^{+0.27}_{-0.39}$	$21.13^{+18.37}_{-12.44}$	$11.26^{+0.15}_{-0.26}$	$18.30^{+7.27}_{-8.32}$
J215.30733-00.45906	46.00±5.64	14.76±4.95	4.87±3.00	$11.48^{+0.27}_{-0.37}$	$30.52^{+26.51}_{-17.59}$	$11.55^{+0.19}_{-0.23}$	$35.19^{+19.68}_{-14.56}$

Note: *Herschel* SPIRE photometry are either adopted from the public data releases from the relevant teams when available (DR2 of HerMES and DR1 of H-ATLAS) or based on our own source extraction (for those objects in HerS) using HIPE (Ott 2010).

of the stellar emission template to the bands redder than W2), albeit small, is still considered during the simultaneous fit of the two components. The stellar component was fit to the stellar population synthesis models of Bruzual & Charlot (2003; hereafter BC03). We adopted the BC03 models of solar metallicity and the Chabrier IMF, and used a series of exponentially declining star formation histories with τ ranging from 1 Myr to 20 Gyr. We note that we chose solar metallicity because we do not have any constraint on the metallicities of these objects, and the solar metallicity is the most widely adopted value throughout the literature in such case. The models were allowed to be reddened by dust following the Calzetti's law (Calzetti 2001), with the reddening color excess value, E(B-V), allowed to vary over three ranges: from 0 up to 0.5 mag, from 0 up to 0.3 mag, and fix to zero (i.e., no reddening). While the W4BCGs have very dusty star-forming regions, their exposed stellar popu-

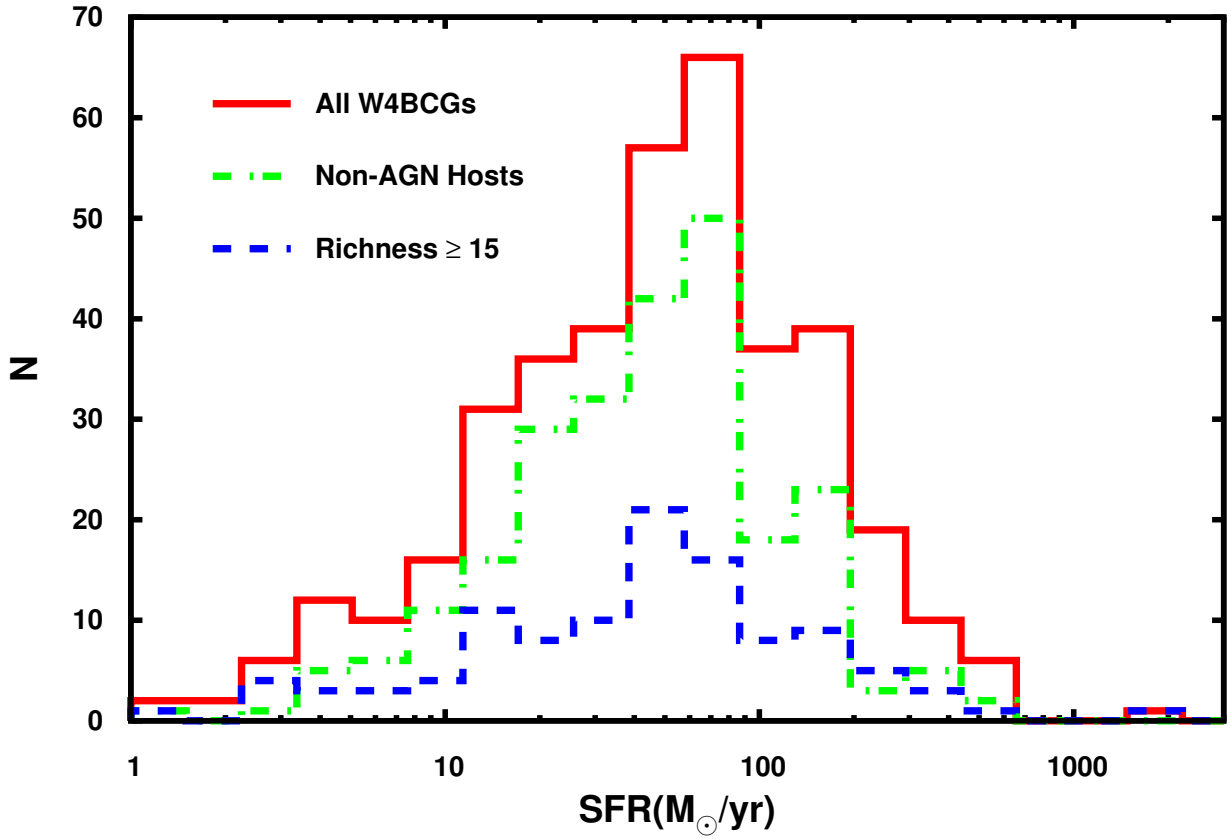

Figure 7. A histogram of the derived SFR for the entire W4BCGs sample (red solid line), the non-AGN host subset (green dot-dashed), and the subset with richness ≥15 (blue dashed line; regardless of hosting AGN or not).

lations as seen in optical-to-near-IR are not necessarily dusty. As the reddening parameter and the age of the stellar population are degenerated, we tested these three different choices to investigate the impact of different reddening values to the derived ages. Redshifts were fixed to those provided by the GMBCG Catalog.

4.3.2. *Far-IR Constraint from Herschel*

As W3 and W4 only sample a small mid-IR window of the entire rest-frame 8-1000 μm range, it could be a concern whether they can accurately "anchor" the fitting templates to derive L_{IR}. A large number of practices in the literature have shown that one or two mid-IR bands indeed can derive L_{IR} reasonably well (see e.g. Chary & Elbaz 2001; Magnelii et al. 2009; Elbaz et al. 2010; Dale et al. 2014), except that in the very high luminosity range such results tend to overestimate the true L_{IR} (see e.g., Elbaz et al. 2011 and the references therein). In order to check how well our derivation of L_{IR} above can be, we tested a few objects that also have FIR SPIRE data as described in §2.4, which samples the peak of the dust emissions and thus offers the most reliable derivation of L_{IR} to date.

Following the same procedure of Ma & Yan (2015), we found secure SPIRE counterparts within a matching radius of 3″ for five W4BCGs: 2 in HerS, 1 in HerMES, and 2 in H-ATLAS. A summary of the data is given in Table 2. We ran LePhare to fit the SEDs of these objects as before, but with the SPIRE photometry added. Fig. 6 shows their SED fitting results. For these five objects, we find that the derived median L_{IR} values with and without the inclusion of the SPIRE data differ by ∼0.1 dex on average and 0.3 dex at most. Therefore, we believe that using W3 and W4 photometry to derive total L_{IR} based on starburst templates (as in §4.3.1) is applicable.

4.3.3. *Results*

Applying Eq. 2 to our sample of 389 W4BCGs results in SFRs ranging from a few to ∼1000 $M_\odot/yr$ (Fig. 7). The median L_{IR} is 5×10^{11} $L_\odot$ (or SFR ∼50 $M_\odot/yr$), and 27% of the whole sample has $L_{IR} > 10^{12}$ $L_\odot$ (or SFR >100 $M_\odot/yr$). The statistics largely remain the same even if we only look at W4BCG-Rs or W4BCG-Ps, or if we remove any possible AGN hosts from the sample. Obviously, the W4BCGs are not "dead", i.e., they are not simply passively evolving like the BCG majority at low redshifts.

In addition to L_{IR}, SED fitting also derives stellar mass and age for each object. To check whether these W4BCGs have different stellar population properties as compared to the BCG majority, we performed SED fitting for all the non-W4BCGs from the entire GMBCG set in the same way as described in §4.3.1. The SEDs were based on the SDSS photometry and the unWISE photometry in W1 and W2. Fig. 8 compares the stellar mass and the age distributions of the W4BCGs to those of the non-W4BCGs. As expected from the reddening-age degeneracy, the ages of the W4BCGs show somewhat different trends with respect to the non-W4BCGs under different choices of allowed reddening range. This

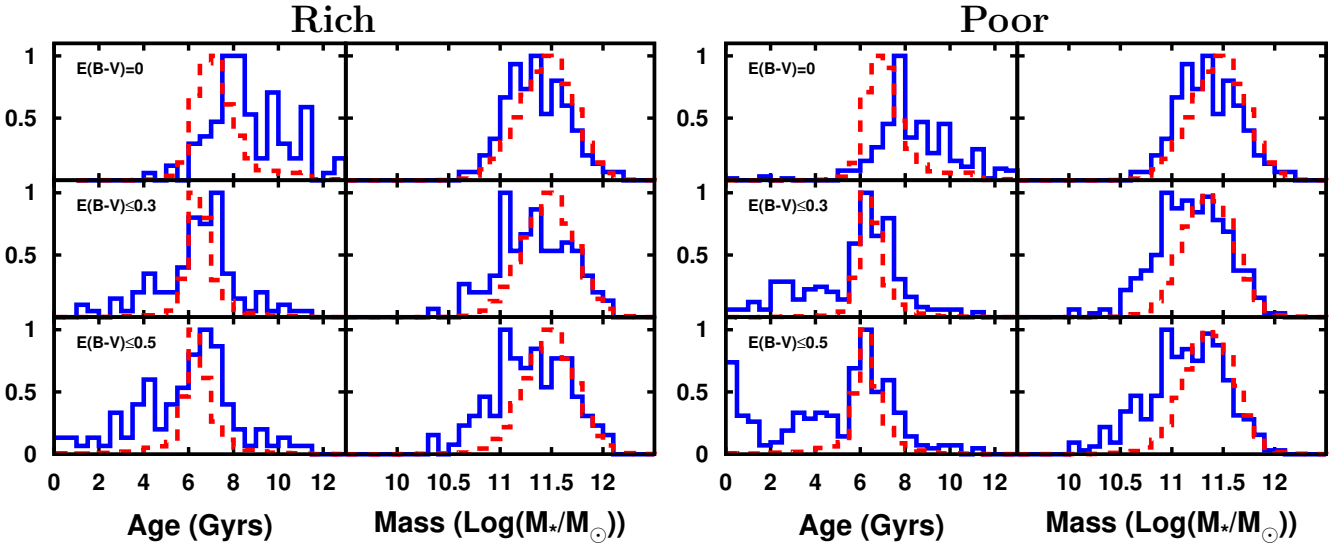

Figure 8. Left: Histogram distribution of the derived ages and masses for the "Rich" subset (richness ≥15) among W4BCGs (solid blue) and the GMBCG catalog (dashed red) for E(B-V) max values of: 0 (top), 0.3 (middle), and 0.5 (bottom). Right: Same as left except with the "Poor" subset (richness <15).

is further complicated by the fact that our SED fitting templates are fixed to solar metallicity. There is also an age-metallicity degeneracy in SED fitting, in the sense that adopting a lower metallicity could result in an older age. Therefore, no definite difference in trend can be claimed regarding the age comparison. The differences in stellar mass, on the other hand, show less variation in the trends under the three choices of allowed reddening ranges. Overall speaking, we believe that the W4BCGs do not show obvious differences as compared to the non-W4BCGs in mass and age of their exposed stellar populations.

5. COOL-CORE CLUSTERS

As mentioned in §1, it has been reported in the literature that some BCGs do exhibit ongoing star formation. While their SFR triggering mechanism is unclear, they are believed to reside in "cool-core" clusters (e.g. Molendi & Pizzolato 2001; O'Dea et al. 2005; Vikhlinin et al. 2007; Chen et al. 2007; Santos et al. 2008; Hudson et al. 2010; Donahue et al. 2015; McDonald et al. 2016; Molendi et al. 2016). Most of these previously reported star-forming BCGs in cool-core clusters have much lower SFR as compared to the bulk of our W4BCGs, with the most notable exception of the BCG in the Phoenix cluster at $z = 0.597$ (McDonald et al. 2012; Tozzi et al. 2015; Mittal et al. 2017), which has $SFR \sim 450\ M_{\odot}/yr$ (after scaling to the Chabrier IMF). In this section, we consider whether our W4BCGs reside in cool-core clusters (hereafter "CC clusters") as well, which can be determined by analyzing X-ray data.

5.1. *Archival Chandra Data*

We searched the *Chandra* archive and found that 10 W4BCGs have existing data. All observations were obtained using the ACIS instrument in either FAINT or VFAINT mode. Table 3 summarizes these data.

5.2. *X-ray c_{SB} Parameter*

Typically, a central X-ray surface brightness excess is a good indicator of a cool core (Fabian & Nulsen 1977). Following this idea, Santos et al. (2008) investigate the surface brightness concentration of galaxy clusters in the central region, and propose a parameter, c_{SB}, to distinguish between CC and non-CC clusters.

This parameter is defined as the ratio of the soft X-ray flux within 40 kpc and within 400 kpc (Santos et al. 2008):

$$c_{SB} = \frac{F_{r<40kpc}}{F_{r<400kpc}} \tag{3}$$

These radii are chosen because they result in the largest difference between CC and non-CC clusters. The value for c_{SB} can be divided into three different regimes (Vikhlinin et al. 2007; Santos et al. 2008): non-CC ($c_{SB} < 0.075$), moderate CC ($0.075 < c_{SB} < 0.155$), and strong CC ($c_{SB} > 0.155$). Following Santos et al. (2010), we adopted the 0.5-2.0 keV band for the soft X-ray flux measurement.

Fig. 9 shows the values of c_{SB} for all the sources with *Chandra* observations. As is quite apparent, the value for c_{SB} puts seven out of ten of these objects in the strong CC region, although two might have contamination due to AGN activity. However, there are three clusters not detected in X-ray at all, which we will discuss later in §5.4.

5.3. *X-ray Spectral Fitting*

For these seven CC clusters we further investigate their properties by carrying out X-ray spectral fitting. The spectra were fit using `XSPEC` 12.9.0 (Arnaud 1996) and a cooling flow model `mkcflow` (Mushotzky & Szymkowiak 1988) coupled with a single-temperature `mekal` model (Mewe et al. 1985, 1986; Kaastra 1992; Liedahl et al. 1995). We follow the same procedure outlined in §3.2 of Mol16 for the first method to find the spectral mass deposition rate. The minimum temperature for the `mkcflow` model was frozen to 0.15 keV, while the maximum temperature was frozen to 3.0 keV. The minimum tempera-

Table 3
Summary of Available Archival *Chandra* Data

GMBCG Catalog Name	ObsID	*Chandra* Target Name	RA(J2000)[a]	DEC(J2000)[a]	z[b]	Exptime (ks)	$F_{r<40kpc}$ $(erg/s/cm^2)$	$F_{r<400kpc}$ $(erg/s/cm^2)$
W4BCG-R								
J027.58864-10.09181	11711	MACS J0150.3-1005	1:50:21.27	-10:05:30.50	0.365	26.8	2.27E-13	8.60E-13
J125.25942+07.86314[c]	1647	RXJ0821	8:21:02.26	7:51:47.30	0.14*	9.4	4.21E-13	2.12E-12
–	17194	RXJ0821.0+0752	8:21:02.26	7:51:47.30	0.14*	29.2	4.04E-13	1.79E-12
–	17563	RXJ0821.0+0752	8:21:02.26	7:51:47.30	0.14*	37.3	4.26E-13	1.78E-12
J128.72875+55.57253[c]	1645	4C55.16	8:34:54.90	55:34:21.10	0.241	9.1	5.18E-13	1.98E-12
–	4940	4C55.16	8:34:54.90	55:34:21.10	0.241	96.0	7.41E-13	2.14E-12
J160.18541+39.95313	1652	ABELL 1068	10:40:44.50	39:57:11.30	0.138	26.8	1.61E-12	5.54E-12
J219.69392+06.50142	15376	J219.69392+06.50142	14:38:46.54	6:30:05.10	0.403	9.6	<1.81E-15	<6.92E-14
J355.91977+00.34170	5786	ZwCl 2341.1+0000	23:43:40.74	0:20:30.10	0.261	29.8	<3.72E-15	<2.60E-13
W4BCG-P								
J125.63314+05.95189	12730	3C198	8:22:31.95	5:57:06.80	0.082	8.0	<6.38E-15	<3.56E-13
J132.60301+37.78597	11576	6C0850+3747	8:50:24.72	37:47:09.50	0.33*	39.3	1.61E-13	2.43E-13
J133.71068+62.31389	16138	RXJ085451.0+621843	8:54:50.56	62:18:50.00	0.29*	17.7	4.80E-13	5.79E-13
J140.28593+45.64928	827	3C219	9:21:08.62	45:38:57.40	0.174	18.8	5.23E-13	7.78E-13

[a] As quoted from the GMBCG catalog
[b] Redshifts marked with an asterisk are photometric redshifts
[c] J125.25942+07.86314 was observed three times, and J128.72875+55.57253 was observed twice. These data were treated separately in our follow-up analysis.

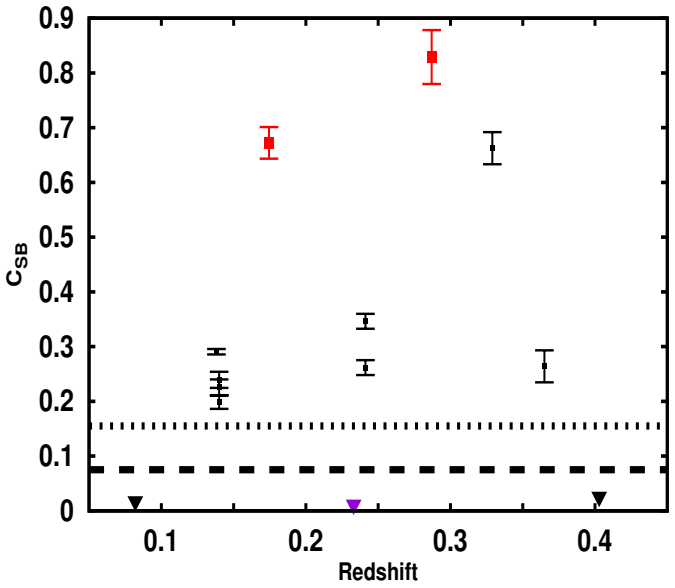

Figure 9. A plot of c_{SB} versus redshift of the 10 W4BCGs that have archival Chandra X-ray data. The dashed line at 0.075 separates non-cool-cores from moderate cool cores. The dot-dashed line at 0.155 separates moderate cool-cores from strong cool-cores. Possible AGN hosts are color coded according to identification method: BPT in blue, WISE color in red, and both in purple. The three data points at z=0.14 and the two at z=0.24 are for c_{SB} derived using different observations of the same object. The triangle shows the upper limit of the object that has no X-ray detection.

ture for the `mekal` model was set to 4.0 keV. The Galactic absorption was frozen to the value based on the radio map of Kalberla et al. (2005) at the position of the BCG. The `mkcflow` fitting outputs the mass deposition rate ($\dot{M}_{dep}$) in $M_\odot/yr$.

The fitting results are given in Table 4. Values with no error given represent fits that did not converge (i.e., error was larger than calculated value), and we quote the upper limit based upon the 95% confidence level. Five out of these seven have mass deposition rates falling short of the SFR estimate from L_{IR}. Even for the ones with $\dot{M}_{dep} > SFR$, it would require a very high efficiency ($\eta > 37$–86%) to convert mass into stars so that the observed SFR can be sustained by the cooling flow. Thus, it is unclear whether a possible cooling flow in these CC clusters can be responsible for the observed W4BCG star formation.

This result is in agreement with the recent observations of some BCGs in Mol16, where the mass deposition rate was found to be an order of magnitude lower than the estimated star formation rate. Mol16 provides some possible explanations for this phenomenon, which include an origin of the gas other than the ICM, a delay between cooling and star formation, and, most likely, gas cooling out of the X-ray phase in regions much larger than those measured. However, further investigation is beyond the scope of this paper.

5.4. *Lack of Cool-Core?*

As shown in the previous section, seven of these W4BCGs are consistent with current theory by residing in cool-core clusters. However, three W4BCG do not have X-ray detection and thus show no sign of being in a cool-core, which could contradict the currently accepted picture. For these objects, the upper limit of the soft X-ray flux within a 40 kpc aperture is no larger than 2×10^{-15} $erg\ s^{-1}cm^{-2}$ (for comparison, the detected sources have fluxes on the order of 10^{-13}–10^{-12} $erg\ s^{-1}cm^{-2}$). Here we discuss them briefly:

J219.69392+06.50142

This W4BCG is at z_{spec}=0.4029, which is the most distant one in the X-ray sample. However, its exposure time of only 9.6 ks puts it at the shallow end of observations. Deeper X-ray observations are needed before any conclusions can be reached regarding this particular object.

J355.91977+00.34170

The lack of X-ray detection at this position may be attributed to the peculiar environment that the cluster resides. This cluster is at z_{spec}=0.261 (GMBCG

Table 4
X-Ray Spectral Fitting Results

GMBCG Catalog Name	*Chandra* ObsID	Reduced χ^2	Mass Deposition Rate ($M_\odot$/yr)	Mass Deposition Rate Excluding 2kpc ($M_\odot$/yr)	$SFR_{L_{IR}}$ ($M_\odot$/yr)
W4BCG-R					
J027.58864-10.09181	11711	1.6	105.1†	126.9†	215.9^{+178}_{-125}
J125.25942+07.86314	1647	1.8	23.5±4.7	22.8±4.7	102.8^{+24}_{-76}
–	17194	1.9	23.0±3.8	20.4±3.7	102.8^{+24}_{-76}
–	17563	2.5	30.0±3.4	27.9±3.4	102.8^{+24}_{-76}
J128.72875+55.57253	1645	1.7	20.0†	19.1†	$43.3^{+18.9}_{-4}$
–	4940	4.0	17.8±8.3	24.0±6.8	$43.3^{+18.9}_{-4}$
J160.18541+39.95313	1652	3.6	36.7±5.3	37.4±5.2	118.7^{+137}_{-38}
W4BCG-P					
J132.60301+37.78597	11576	1.7	106.0±23.5	53.4±23.9	39.7^{+66}_{-14}
J133.71068+62.31389	16138	1.1	183.1±56.3	149.2±56.9	157.4^{+27}_{-70}
J140.28593+45.64928	827	1.8	–‡	2.2†	135.9^{+20}_{-60}

† These fitting results represent maximum values based upon 95% confidence.
‡ Fitting approached zero or null value.

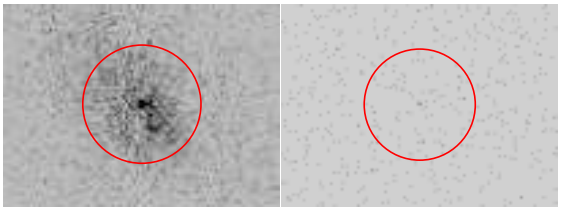

Figure 10. The left panel shows J128.72875+55.57253 detected in the *Chandra* data with an exposure time of 9 ks and z_{spec} = 0.24118, while the right panel shows J125.63314+05.95189 not detected in the *Chandra* data with an exposure time of 8 ks and z_{spec} = 0.081474. The circles are centered on the reported SDSS positions and are 40 kpc in size.

gives z_{ph}=0.23), and it is merging with a nearby cluster at z_{spec}=0.267 (z_{ph}=0.27 from GMBCG) that is 5.4′ away. The entire system is usually referred to as ZwCl 2341.1+0000, whose ICM is known to be disturbed and elongated in shape (van Weeren et al. 2009). While there is X-ray emission from the whole structure, the peak lies in between the two clusters and hence is offset from either BCGs. Under this circumstance, it might not be applicable to discuss the existence of a CC cluster.

J125.63314+05.95189

While the *Chandra* exposure at this position is only 8 ks, the short integration probably is not the reason for the non-detection because the object is very nearby (z_{spec}=0.0815[3]). In Fig. 10, we show that for another W4BCG with a similar exposure time yet higher redshift, there is still a clear X-ray detection. We do note that this particular W4BCG is identified as being in a low-richness or "poor" cluster.

Due to the small sample and the aforementioned complications, we conclude that deeper X-ray observations of more W4BCGs are needed in order to put the connection of starforming BCGs and cool-core clusters on a more solid ground.

[3] This BCG is at z_{spec}=0.0815 based on the SDSS DR7, however GMBCG accidentally does not use this value and keeps quoting z_{ph}=0.132 instead. Nevertheless, we verify that it indeed belongs to a cluster at z=0.08. It is surrounded by ∼12 red galaxies at z_{ph}=0.08 ± 0.02 that form a clear red sequence, and it is the brightest among all potential members.

6. DISCUSSION

While the common wisdom about BCGs at low redshifts is that they are quiescent galaxies, we have shown that the W4BCGs presented here are exceptions. In most cases, their W4 emissions are due to dust heated by strong star formation. Admittedly, such exceptions will not change the overall picture of BCGs because they are only a minority (W4BCGs accounting only ∼0.8% among the entire GMBCG catalog). However, it is important to understand why such exceptions can happen, because this can be related to the critical question in understanding the evolution of high-mass galaxies, namely, why most high-mass galaxies have their star formation processes quenched early in time.

We first note that the W4BCGs do not seem to have unusual environments. While it is widely believed that mergers could induce star formation, the W4BCGs are not predominantly mergers (see §4.2). Second, as compared to the non-W4BCGs, the W4BCGs as a whole have slightly less stellar mass and some of them can have younger ages. However, these differences are not significant and might be the results of the fitting model degeneracy rather than being real.

Third, the cooling-flow interpretation can only explain a small fraction of W4BCGs. Among ten of them that have archival X-ray data, only seven are detected. While these seven X-ray-detected W4BCGs are consistent with being residing in cool-core clusters, five of them have their mass deposition rates (from a cooling flow model) less than their inferred SFRs.

Therefore, our investigations thus far still do not seem to be leading to a universal mechanism that can explain why W4BCGs have high SFRs. Nevertheless, there might be one clue, which is in the redshift distribution of the W4BCGs (see Fig. 2). The high-redshift end ($z \gtrsim 0.4$) of this distribution follows that of the full GMBCG sample, which is not surprising. However, it stays relatively constant at lower redshifts, which is a feature not seen in the redshift distribution of the parent GMBCG sample. While it is still unclear how such a difference can be related to the existence of W4BCGs, it will be worth further study in the future.

7. CONCLUSION

In this paper, we present our systematic census of BCGs at low redshifts ($z < 0.55$) that are still actively forming stars[4]. We use the SDSS-based GMBCG catalog, which is the largest BCG catalog to date, and identify those that have strong mid-IR emissions by their prominent detections in the W4-band (22 μm) in the WISE all-sky survey. The full catalog of these W4BCGs is presented in Table 5, including their various properties as discussed in previous sections.

While some of the W4BCGs could be AGN hosts, the majority of them are not. Therefore, their strong W4 emissions should be powered by dust heating from star formation. Even for those that are possible AGN hosts, we show that their W4 emissions are still most likely due to star formation. Our W4BCGs have median SFR of $\sim$50 $M_{\odot}/yr$, and some have SFR as high as 500$-$1000 $M_{\odot}/yr$. Clearly, the W4BCGs are quite contrary to what is expected for BCGs at low redshifts, which are believed to be old, passively evolving galaxies (i.e., "red-and-dead"). There have been a number of studies reporting some low-redshift BCGs that still have non-negligible star formation, but their SFRs are lower than what we observe among these W4BCGs and/or have smaller sample sizes. Although such actively star-forming BCGs are only a minority among all BCGs, their very existence could have important implications to the evolution of very high mass galaxies.

Our investigations so far are not able to answer why these BCGs are still actively forming stars at such a late stage. The previous studies of low-redshift BCGs that are still not completely "dead" usually attribute the star formation triggering mechanism to the cooling flows in cool-core clusters. However, for the seven identified to be in cool-core clusters based upon X-ray data, the possible mass deposition rates due to a cooling flow fall significantly short to explain the observed SFRs, and thus the true triggering mechanism still remains a mystery. One possible clue to solve this problem could be that W4BCGs are different from the quiescent majority in their redshift distribution: their number is redshift independent as compared to the whole GMBCG sample. Further study of field galaxies will be necessary to shed new light to the understanding of this behavior.

We acknowledge the support of NASA's Astrophysics Data Analysis Program under grant number NNX15AM92G. This publication makes use of data products from the Wide-field Infrared Survey Explorer, which is a joint project of the University of California, Los Angeles, and the Jet Propulsion Laboratory/California Institute of Technology, funded by the National Aeronautics and Space Administration. We would also like to thank Zhiyuan Ma for his help with HIPE.

[4] During the revision of this paper, Bonavenutra et al. (2017) posted their paper on the study of star-forming BCGs, with the same main title as ours. The majority ($\sim$75%) of the star-forming BCGs in their sample, however, are at $z > 0.55$ and thus are beyond the redshift range of our W4BCGs. In this sense, the high SFRs observed in the W4BCGs are more difficult to understand because they are supposed to settle down already at such a late time of the universe.

REFERENCES

Arnaud, K. A. 1996, in Jacoby G. H., Barnes J., eds, ASP Conf. Ser. Vol. 101, Astronomical Data Analysis Software and Systems V. Astron. Soc. Pac., San Francisco, p. 17
Arnouts, S., Cristiani, S., Moscardini, L., et al. 1999, MNRAS, 310
Assef, R. J., Stern, D., Kochanek, C. S., et al. 2013, ApJ, 772
Baldwin, J. A., Phillips, M. M., & Terlevich, R. 1981, PASP, 93
Brinchmann, J. o. 2004, MNRAS, 351
Bruzual, G., & Charlot, S. 2003, MNRAS, 344
Calzetti, D. 2001, PASP, 113
Chabrier, G. 2003, PASP, 115
Chary, R., & Elbaz, D. 2001, ApJ, 556
Chen, Y., et al. 2007, A&A, 466
Cowie, L. L., Songaila, A., Hu, E. M., Cohen, J. G., et al. 1996, AJ, 112
Dale, D., & Helou, G. 2002, ApJ, 576
Dale, D. A., Helou, G., et al. 2014, ApJ, 784
De Lucia, G., et al. 2006, MNRAS, 366
Donahue, M., et al. 2015, ApJ, 805
Dubinski. 1998, ApJ, 502
Eales, S., et al. 2010, PASP, 122
Elbaz, D., et al. 2010, A&A, 518
—. 2011, A&A, 533
Fabian, A. C., & Nulsen, P. E. J. 1977, MNRAS, 180
Fogarty, K., et al. 2015, ApJ, 813
Fruscione, A., et al. 2006, SPIE, 6270
Griffin, M. J., et al. 2010, A&A, 518
Hao, J., McKay, T. A., Koester, B. P., et al. 2010, ApJS, 191
Hudson, D. S., Mittal, R., Reiprich, T. H., et al. 2010, A&A, 513
Ilbert, O., Arnouts, S., McCracekn, H. J., et al. 2006, A&A, 457
Jarrett, T. H., Cohen, M., et al. 2011, ApJ, 735
Kaastra, J. 1992, An X-Ray Spectral Code for Optically Thin Plasmas (Internal SRONLeiden Report, updated version 2.0)
Kalberla, P. M. W., Burton, W. B., Hartmann, D., et al. 2005, A&A, 440
Kauffmann, G., Heckman, T. M., Tremonti, C., et al. 2003a, MNRAS, 346
Kauffmann, G., et al. 2003b, MNRAS, 341
Kennicutt, R. C. 1998, ARAA, 36
Kewley, L. J., Dopita, M. A., Sutherland, R. S., et al. 2001, ApJ, 556
Lang, D. 2014, AJ, 147
Lang, D., Hogg, D. W., & Schlegel, D. J. 2014, Arxiv e-print
Liedahl, D. A., Osterheld, A. L., & Goldstein, W. H. 1995, ApJ, 438
Ma, Z., & Yan, H. 2015, ApJ, 811
Magnelii, B., Elbaz, D., Chary, R., et al. 2009, A&A, 496
Mateos, S., Alonso-Herrero, A., Carrera, F. J., et al. 2012, MNRAS, 426
McDonald, M., Bayliss, M., Benson, B. A., et al. 2012, Nature, 488
McDonald, M., et al. 2016, ApJ, 817
Mewe, R., Gronenschild, E. H. B. M., & van den Ooord, G. H. J. 1985, A&A, 62
Mewe, R., Lemen, J. R., & van den Ooord, G. H. J. 1986, A&A, 65
Mittal, R., et al. 2017, MNRAS, 465
Molendi, S., & Pizzolato, F. 2001, ApJ, 560
Molendi, S., Tozzi, P., et al. 2016, A&A, 595
Mushotzky, R. F., & Szymkowiak, A. E. a. 1988, in NATO ASIC Proc. 229: Cooling Flows in Clusters and Galaxies, ed. A. C. Fabian, 53-62
O'Dea, C., et al. 2005, ApJ, 681
Oliver, S., Bock, J., et al. 2012, MNRAS, 424
Ott, S. 2010, in ASP Conf. Ser. 434, Astronomical Data Analysis Software and Systems XIX, ed. Y. Mizumoto, K.-I. Morita, and M. Ohishi (San Francisco, CA: ASP), 139
Pilbratt, G. L., et al. 2010, A&A, 518
Roseboom, I. G., et al. 2010, MNRAS, 409
Rykoff, E. S., et al. 2014, ApJ, 785
Salpeter, E. E. 1955, ApJ, 121
Santos, J. S., Rosati, P., Tozzi, P., et al. 2008, A&A, 483

Santos, J. S., Tozzi, P., Rosati, P., & Böhringer, H. 2010, A&A, 521
Siebenmorgen, & Krügel. 2007, AA, 462
Smith, A. J., et al. 2012, MNRAS, 419
Stern, D., Assef, R. J., Benford, D. J., et al. 2012, ApJ, 753
Tozzi, P., Gastaldello, F., et al. 2015, A&A, 580
Tremonti, C. A., et al. 2004, ApJ, 613
Valiante, E., et al. 2016, MNRAS, 462
van Weeren, R. J., et al. 2009, A&A, 506
Viero, M. P., et al. 2013, ApJ, 772
—. 2014, ApJS, 210
Vikhlinin, A., Burenin, R., Forman, W. R., et al. 2007, in Heating versus Cooling in Galaxies and Clusters of Galaxies, ed. H. Böhringer, G. W. Pratt, A. Finoguenov, & P. Schuecker , 48
Wang, L., et al. 2014, MNRAS, 444
Wright, E. L., Eisenhardt, P. R. M., et al. 2010, ApJ, 140
York, D. G., Adelman, J., et al. 2000, AJ, 120

APPENDIX

W4BCGS IN REDMAPPER

While we focused on the GMBCG catalog for our search of W4BCGs, the same procedure can be applied to other cluster catalogs. One such catalog is that produced by the redMaPPer algorithm (Rykoff et al. 2014). Like the GMBCG catalog, the redMaPPer catalog was produced by the use of a cluster finding algorithm on SDSS data. However, redMaPPer utilized SDSS DR8 photometric data and different criteria for cluster identification. The redMaPPer catalog consists of 26,111 cluster candidates covering a redshift range of $0.08 < z < 0.55$, roughly half the size of the GMBCG catalog despite covering a larger area and similar redshift range. To check for possible overlap between the two, we cross-matched the catalogs using a radius of $400''$, which corresponds to $\sim$2 Mpc at the median redshift $z = 0.35$. There is a possible overlap of 14,386 cluster candidates between the redMaPPer and GMBCG catalog.

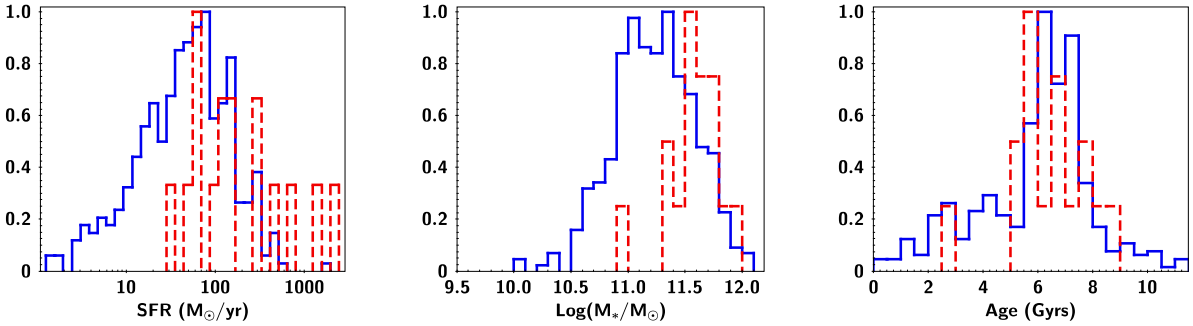

Figure 11. Comparison of the derived SFR (left), stellar mass (middle), and age (right) for the W4BCGs from the GMBCG catalog (solid blue) and the redMaPPer catalog (red dashed), following the same SED fitting procedure as in §4.3. The fit to the stellar population is based on E(B-V) up to 0.3 mag. Each graph is normalized for easy comparison.

Following the same procedure outlined in §3, we searched for BCGs in the redMaPPer catalog that had secure W4 detections. The final sample of W4BCGs in the redMaPPer consists of 16 candidates ($\sim$0.07% of the total catalog). We preformed the same SED analysis for these objects following the procedures in §4.3. Their L_{IR}-based SFR, as well as the stellar mass and the age of their stellar populations, are shown in the histograms in Fig. 11. For comparison, we also plot the distributions of the W4BCGs from the GMBCG catalog. Despite the small number of sources, it seems that redMaPPer W4BCGs have slightly higher masses and SFRs as compared to the GMBCG sample. However, the fact remains that these W4BCGs exhibit a high amount of star formation based upon their L_{IR}.

Table 5
Photometry and Derived Properties for W4BCGs

GMBCG Catalog Name	RA(J2000)†	DEC(J2000)†	z_{phot}†	z_{spec}†	Richness†	u	g	r	i	z	W1	W2	W3	W4	$Log(L_{IR}/L_\odot)$	SFR($M_\odot$/yr)	Age(Gyr)	Log($M^*/M_\odot$)	AGN
GMBCG J000.12121+15.71478	0.12121387	15.71477557	0.11±0.03	0.115441	8	19.42±0.07	17.48±0.01	16.48±0	15.98±0	15.61±0.01	15.59±0	15.98±0.01	15.3±0.06	14.49±0.19	$10.94^{+0.29}_{-0.37}$	$8.71^{+8.19}_{-4.97}$	$7.4^{+1.1}_{-3.49}$	$10.94^{+0.17}_{-0.06}$	BPT
GMBCG J001.48978+15.69867	1.48977949	15.69867485	0.24±0.02	0.218624	10	21.13±0.34	18.88±0.02	17.44±0.01	16.87±0.01	16.49±0.02	16.33±0.01	16.48±0.01	15.57±0.08	14.63±0.2	$11.56^{+0.27}_{-0.39}$	$36.4^{+31.58}_{-21.49}$	$7.5^{+2.12}_{-1.42}$	$11.5^{+0.09}_{-0.06}$	BPT
GMBCG J002.18580+00.08110	2.1857991	0.08110011	0.38±0.04	0.0	10	21.5±0.55	20.54±0.07	18.87±0.02	18.31±0.02	17.73±0.05	16.59±0.01	16.34±0.01	14.97±0.06	13.82±0.12	$12.43^{+0.25}_{-0.36}$	$266.44^{+211.86}_{-150.8}$	$6.57^{+1.74}_{-2.73}$	$11.67^{+0.1}_{-0.1}$	WISE
GMBCG J002.89046+15.21398	2.89045783	15.21398079	0.3±0.03	0.0	9	19.98±0.1	19.23±0.02	18.39±0.01	18.09±0.01	17.65±0.04	16.29±0	15.85±0.01	14.96±0.04	14.74±0.21	$12.39^{+0.07}_{-0.23}$	$247.17^{+45.65}_{-101.79}$	$1.67^{+0.44}_{-0.37}$	$10.74^{+0.06}_{-0.08}$	WISE
GMBCG J007.75699-09.61500	7.75699353	-9.61499813	0.16±0.04	0.0	8	20.84±0.28	19.21±0.02	18.13±0.01	17.48±0.01	17.07±0.04	16.87±0.01	17±0.02	14.64±0.03	13.25±0.06	$11.72^{+0.27}_{-0.39}$	$51.96^{+44}_{-30.61}$	$8.86^{+2.22}_{-1.6}$	$11.05^{+0.08}_{-0.08}$	NONE
GMBCG J011.86695-00.60513	11.86695358	-0.60513368	0.42±0.02	0.429752	24	22.35±1.09	20.66±0.08	18.84±0.02	18.11±0.02	17.7±0.05	17.27±0.02	17.36±0.04	17.5±1.26	13.92±0.15	$12.1^{+0.41}_{-0.15}$	$125.63^{+195.36}_{-37.47}$	$6.45^{+1.78}_{-2.34}$	$11.64^{+0.07}_{-0.11}$	NONE
GMBCG J015.05143+14.84481	15.05143029	14.8448104	0.38±0.07	0.0	8	21.72±0.3	20.81±0.05	19.35±0.02	18.72±0.02	18.2±0.05	16.98±0.01	16.7±0.01	15.87±0.08	14.72±0.17	$12.06^{+0.26}_{-0.35}$	$115.74^{+94.68}_{-63.92}$	$7.12^{+1.25}_{-1.62}$	$11.53^{+0.09}_{-0.09}$	WISE
GMBCG J027.06772+00.32915	27.06772378	0.32915166	0.15±0.02	0.0918369	11	18.16±0.03	16.72±0	15.86±0	15.43±0	15.17±0.01	15.09±0	15.27±0	14.81±0.03	14.04±0.09	$10.85^{+0.3}_{-0.35}$	$7.06^{+7.01}_{-3.92}$	$6.5^{+0.77}_{-0.83}$	$11.22^{+0.06}_{-0.27}$	NONE
GMBCG J027.24559-00.70620	27.24558949	-0.7062	0.35±0.02	0.0	14	22.49±0.7	20.65±0.04	18.93±0.02	18.31±0.01	17.93±0.03	17.28±0.01	17.74±0.03	18.24±0.6	14.38±0.11	$11.39^{+0.29}_{-0.16}$	$24.6^{+22.82}_{-7.75}$	$6.32^{+1.86}_{-2.46}$	$11.36^{+0.09}_{-0.12}$	NONE
GMBCG J027.58864-10.09181	27.58863802	-10.09180529	0.31±0.08	0.365	16	19.57±0.18	18.49±0.03	17.16±0.01	16.62±0.01	16.14±0.03	15.61±0	16.03±0.01	15.01±0.05	14±0.12	$12.33^{+0.26}_{-0.37}$	$215.92^{+177.99}_{-124.74}$	$6.98^{+1.39}_{-2.2}$	$12.05^{+0.08}_{-0.1}$	BPT
GMBCG J027.86875+14.38572	27.86875171	14.38572344	0.35±0.1	0.0	9	22.07±0.28	21.15±0.06	19.86±0.03	19.23±0.03	18.94±0.06	17.9±0.02	17.97±0.04	16.24±0.09	15±0.19	$11.83^{+0.28}_{-0.34}$	$67.33^{+61.73}_{-36.2}$	$6.38^{+1.91}_{-2.09}$	$11^{+0.09}_{-0.1}$	NONE
GMBCG J029.17012-00.37641	29.17012063	-0.37640939	0.36±0.09	0.0	12	21.34±0.29	20.63±0.06	19.48±0.04	18.96±0.03	18.51±0.07	17.78±0.02	17.49±0.03	15.9±0.07	14.65±0.15	$12.01^{+0.27}_{-0.35}$	$103.04^{+86.68}_{-56.68}$	$6.08^{+1.97}_{-2.31}$	$11.08^{+0.1}_{-0.11}$	WISE
GMBCG J029.56746+00.00350	29.56746057	0.0034958	0.42±0.02	0.0	20	23.48±1.2	21.99±0.12	20.26±0.04	19.54±0.03	19.09±0.09	18.35±0.03	18.84±0.09	18.51±0.71	15.01±0.19	$11.4^{+0.39}_{-0.18}$	$25.04^{+35.9}_{-8.49}$	$6.17^{+1.8}_{-2.63}$	$11.09^{+0.09}_{-0.14}$	NONE
GMBCG J029.97041-08.20800	29.97040719	-8.20800187	0.34±0.03	0.346697	9	22.8±1.55	20.29±0.05	18.63±0.02	18±0.02	17.51±0.05	17±0.01	17.35±0.03	-99±-99	14.59±0.16	$11.9^{+0.36}_{-0.27}$	$79.67^{+104.11}_{-36.88}$	$6.59^{+1.74}_{-2.45}$	$11.52^{+0.09}_{-0.13}$	NONE
GMBCG J034.05742-00.72531	34.05742358	-0.72531111	0.31±0.07	0.0	15	19.91±0.14	19.12±0.02	18±0.01	17.55±0.01	17.14±0.03	16.85±0.01	16.93±0.02	15.97±0.07	15.07±0.2	$11.79^{+0.26}_{-0.38}$	$61.12^{+49.67}_{-35.6}$	$6.44^{+2.05}_{-2.26}$	$11.3^{+0.08}_{-0.09}$	NONE
GMBCG J038.44672-08.84924	38.44672304	-8.84923564	0.28±0.02	0.0	18	22.23±1.77	19.02±0.03	17.5±0.01	16.96±0.01	16.48±0.03	16.36±0.01	16.77±0.02	18.2±0.74	14.83±0.2	$11.12^{+0.44}_{-0.18}$	$13.33^{+23.17}_{-4.51}$	$7.58^{+1.62}_{-1.83}$	$11.75^{+0.08}_{-0.13}$	NONE
GMBCG J039.77836-07.69936	39.77836437	-7.69935863	0.39±0.07	0.0	9	25.05±2.79	20.98±0.09	19.68±0.05	18.9±0.04	18.48±0.09	17.76±0.02	18.09±0.05	16.36±0.09	15.1±0.19	$11.88^{+0.29}_{-0.32}$	$75.16^{+71.7}_{-38.9}$	$6.49^{+1.79}_{-2.68}$	$11.28^{+0.1}_{-0.14}$	NONE
GMBCG J044.83916+00.30161	44.83916234	0.30160525	0.14±0.02	0.13802	13	18.77±0.09	17.56±0.01	16.82±0.01	16.45±0.01	16.15±0.02	16.25±0.01	16.58±0.02	14.87±0.03	14.59±0.17	$11.5^{+0.11}_{-0.56}$	$31.91^{+9.04}_{-23.2}$	$5.11^{+3.71}_{-2.62}$	$10.81^{+0.16}_{-0.15}$	NONE
GMBCG J048.94591-07.99395	48.94590677	-7.99395005	0.24±0.07	0.274238	12	19.47±0.1	18.45±0.01	17.54±0.01	17.2±0.01	16.84±0.03	16.39±0	16.17±0.01	14.64±0.02	14.15±0.12	$12.43^{+0.04}_{-0.19}$	$271.33^{+28.93}_{-95.98}$	$2.35^{+0.97}_{-0.62}$	$11.07^{+0.09}_{-0.08}$	BOTH
GMBCG J055.26483-05.56434	55.26483489	-5.56434196	0.45±0.05	0.0	9	22.76±0.82	21.49±0.09	19.93±0.04	19.21±0.03	18.51±0.06	16.06±0	15.52±0	14.81±0.04	13.87±0.1	$12.69^{+0.23}_{-0.38}$	$493.4^{+351.68}_{-286.82}$	$7.28^{+0.96}_{-1.25}$	$11.71^{+0.09}_{-0.12}$	WISE
GMBCG J112.54887+42.00126	112.54886592	42.00126089	0.41±0.07	0.0	12	21.46±0.3	20.77±0.05	19.93±0.04	19.37±0.03	18.94±0.08	17.72±0.02	17.89±0.04	16.75±0.2	14.58±0.18	$11.74^{+0.41}_{-0.17}$	$55.39^{+87.11}_{-17.93}$	$5.53^{+1.67}_{-1.69}$	$11.06^{+0.09}_{-0.11}$	NONE
GMBCG J113.43436+38.87798	113.43435675	38.87798154	0.18±0.02	0.0	9	20.48±0.18	18.73±0.02	17.6±0.01	17.09±0.01	16.76±0.02	16.75±0.01	16.76±0.02	14.9±0.04	13.92±0.09	$11.86^{+0.11}_{-0.53}$	$73^{+20.16}_{-51.53}$	$6.65^{+2.82}_{-3.03}$	$11.05^{+0.12}_{-0.13}$	NONE
GMBCG J114.20870+39.33200	114.2086979	39.33200399	0.18±0.03	0.116268	11	19.09±0.08	17.95±0.01	17.16±0.01	16.73±0.01	16.52±0.02	16.75±0.01	16.66±0.02	14.53±0.03	13.14±0.05	$11.44^{+0.26}_{-0.39}$	$27.27^{+22.79}_{-16.13}$	$6.6^{+2.3}_{-1.77}$	$10.67^{+0.08}_{-0.27}$	BPT
GMBCG J115.36870+44.40880	115.36869909	44.40880028	0.16±0.02	0.132188	14	18.43±0.06	16.84±0.01	15.83±0	15.38±0	15.07±0.01	15.19±0	15.18±0	13.83±0.02	12.86±0.04	$11.93^{+0.09}_{-0.58}$	$84.7^{+20.28}_{-62.61}$	$7.34^{+1.58}_{-0.88}$	$11.63^{+0.05}_{-0.15}$	BPT
GMBCG J118.43924+12.64781	118.43924374	12.6478053	0.19±0.03	0.196569	15	19.79±0.07	18.31±0.01	17.27±0.01	16.78±0.01	16.58±0.02	16.36±0.01	16.58±0.02	14.87±0.04	13.55±0.08	$11.8^{+0.28}_{-0.38}$	$62.85^{+55.54}_{-36.67}$	$4.38^{+3.92}_{-1.95}$	$11.1^{+0.07}_{-0.22}$	BPT
GMBCG J122.41201+34.92700	122.412007888163	34.9270038726458	0.17±0.04	0.0825257	15	17.59±0.01	16.47±0	15.63±0.01	15.23±0	14.9±0	14.87±0	15.17±0	15.12±0.05	14.39±0.15	$10.41^{+0.42}_{-0.21}$	$2.59^{+4.26}_{-0.99}$	$6.31^{+0.51}_{-0.48}$	$11.4^{+0.03}_{-0.03}$	BPT
GMBCG J122.51706+41.27283	122.517057625448	41.2728302106215	0.2±0.04	0.133547	9	18.75±0.03	17.47±0	16.49±0.01	16.09±0	15.76±0.01	15.71±0	16.23±0.01	16.27±0.13	14.26±0.13	$10.75^{+0.42}_{-0.19}$	$5.61^{+9.07}_{-1.98}$	$8.27^{+0.81}_{-0.86}$	$11.32^{+0.05}_{-0.17}$	NONE
GMBCG J123.77273+07.09622	123.772726566836	7.09622106064503	0.12±0.03	0.0	10	18.02±0.02	16.97±0.01	16.41±0	16.02±0.01	15.85±0.01	15.74±0	15.98±0.01	13.71±0.01	13.19±0.06	$11.79^{+0.09}_{-0.59}$	$61.8^{+14.83}_{-45.91}$	$2.28^{+0.45}_{-0.4}$	$10.37^{+0.07}_{-0.05}$	NONE
GMBCG J124.12529+34.58306	124.125285691121	34.5830553582585	0.42±0.1	0.0	12	21.24±0.28	20.43±0.06	19.21±0.03	18.56±0.02	18.27±0.06	17.79±0.02	18.04±0.05	16.69±0.18	14.61±0.17	$11.79^{+0.42}_{-0.17}$	$61.83^{+99.12}_{-20.12}$	$6.74^{+1.47}_{-2.58}$	$11.29^{+0.08}_{-0.1}$	NONE
GMBCG J125.03628+56.72644	125.036284701265	56.726436006056	0.12±0.03	0.0807631	9	17.41±0.02	16.12±0	15.39±0	14.95±0	14.69±0	14.49±0	14.79±0	12.6±0	11.73±0.01	$11.3^{+0.03}_{-0.03}$	$19.94^{+1.29}_{-1.21}$	$5.76^{+2.18}_{-1.59}$	$11.01^{+0.05}_{-0.05}$	NONE
GMBCG J125.25942+07.86314	125.25942181613	7.86313797474906	0.14±0.02	0.0	24	17.98±0.03	16.71±0	15.94±0	15.48±0	15.23±0.01	15.05±0	15.44±0.01	13.83±0.02	12.8±0.04	$12.01^{+0.09}_{-0.58}$	$102.85^{+23.57}_{-75.82}$	$6.02^{+1.85}_{-1.7}$	$11.24^{+0.15}_{-0.07}$	NONE
GMBCG J125.33837+16.12444	125.338367115871	16.1244373982432	0.12±0.02	0.126844	8	19.01±0.05	17.79±0.01	17.1±0.01	16.7±0.01	16.46±0.01	16.47±0.01	16.84±0.02	14.88±0.04	14.16±0.13	$11.34^{+0.24}_{-0.42}$	$22.05^{+16.4}_{-13.66}$	$3.87^{+0.81}_{-1.36}$	$10.55^{+0.06}_{-0.05}$	NONE
GMBCG J126.54276+15.86042	126.542762757289	15.8604177369356	0.19±0.03	0.0	13	18.85±0.03	18.4±0.01	17.64±0.01	17.12±0.01	17±0.01	16.41±0.01	16.32±0.01	15.36±0.06	14.32±0.15	$11.55^{+0.26}_{-0.4}$	$35.3^{+28.39}_{-21.33}$	$8.81^{+1.02}_{-0.93}$	$11.06^{+0.04}_{-0.04}$	NONE
GMBCG J126.74500+53.21243	126.744995027599	53.2124278025339	0.11±0.01	0.117597	18	18.17±0.06	16.14±0	15.14±0.01	14.69±0	14.33±0	14.37±0	14.85±0.01	14.45±0.04	13.87±0.14	$11.12^{+0.31}_{-0.33}$	$13.05^{+13.74}_{-7.01}$	$4.66^{+0.61}_{-0.45}$	$11.32^{+0.05}_{-0.04}$	BPT
GMBCG J127.03216+08.62914	127.032164094954	8.62914486906813	0.43±0.1	0.0	15	21.59±0.17	20.91±0.04	19.8±0.02	19.15±0.02	18.75±0.04	17.02±0.01	16.71±0.01	15.37±0.08	14.17±0.17	$12.38^{+0.29}_{-0.31}$	$242.49^{+225.78}_{-124.65}$	$7.08^{+1.07}_{-1.5}$	$11.35^{+0.06}_{-0.07}$	WISE
GMBCG J127.52713+14.76496	127.527132473944	14.7649592089859	0.3±0.04	0.0	9	19.14±0.06	18.69±0.02	18±0.01	17.64±0.01	17.28±0.03	16.96±0.01	17.09±0.03	15.38±0.06	14.71±0.2	$12.02^{+0.24}_{-0.41}$	$105.49^{+76.27}_{-64.03}$	$0.96^{+1.38}_{-0.16}$	$10.74^{+0.09}_{-0.06}$	NONE
GMBCG J128.45608+47.50471	128.456075979887	47.5047107411214	0.46±0.12	0.0	18	20.89±0.19	20.47±0.05	19.31±0.03	18.61±0.02	18.26±0.06	16.32±0	16.04±0.01	15.32±0.05	14.25±0.12	$12.49^{+0.26}_{-0.35}$	$312.54^{+255.01}_{-172.13}$	$7.06^{+1.12}_{-1.8}$	$11.71^{+0.06}_{-0.09}$	WISE
GMBCG J128.51842+13.71544	128.518423629677	13.71543671725	0.19±0.02	0.179865	10	20.2±0.15	18.49±0.01	17.32±0.01	16.77±0.01	16.44±0.01	16.24±0.01	16.26±0.01	15.85±0.2	14.48±0.21	$11.13^{+0.43}_{-0.21}$	$13.59^{+23.32}_{-5.3}$	$7.31^{+2.98}_{-3.43}$	$11.31^{+0.1}_{-0.05}$	BPT
GMBCG J128.72875+55.57253	128.728748440917	55.5725303361728	0.2±0.03	0.241181	17	19.63±0.18	17.93±0.01	16.73±0.01	16.11±0.01	15.86±0.02	15.76±0	16.12±0.01	15.13±0.05	12.96±0.04	$11.64^{+0.16}_{-0.04}$	$43.32^{+18.89}_{-3.67}$	$7.95^{+0.69}_{-0.63}$	$11.85^{+0.04}_{-0.04}$	BPT
GMBCG J129.17324+03.01820	129.173244962775	3.01820149333377	0.45±0.03	0.0	13	22.33±0.94	21.32±0.09	19.71±0.03	18.92±0.02	18.41±0.08	18.04±0.03	18.84±0.11	19.6±2.74	14.09±0.11	$11.68^{+0.37}_{-0.17}$	$48.31^{+64.23}_{-15.4}$	$6^{+1.77}_{-2.44}$	$11.3^{+0.07}_{-0.15}$	NONE
GMBCG J130.08931+17.24245	130.089305109374	17.242450327423	0.1±0.03	0.059579	8	17.8±0.02	16.61±0	15.98±0	15.59±0	15.38±0.01	15.2±0	15.5±0.01	14.01±0.03	14.04±0.16	$10.4^{+0.04}_{-0.04}$	$2.53^{+0.27}_{-0.2}$	$4.73^{+0.7}_{-0.79}$	$10^{+0.04}_{-0.04}$	BPT
GMBCG J130.54583+59.92378	130.545833209581	59.9237839102679	0.15±0.03	0.12812	12	18.32±0.03	16.84±0	15.96±0	15.5±0	15.21±0.01	14.99±0	15.34±0	13.61±0.01	13.47±0.05	$11.77^{+0.05}_{-0.61}$	$59.31^{+7.82}_{-44.72}$	$2.57^{+0.29}_{-0.23}$	$11.39^{+0.04}_{-0.14}$	NONE
GMBCG J130.97171+09.84038	130.971712696306	9.84037989028271	0.34±0.08	0.0	9	20.98±0.18	20.14±0.03	18.61±0.01	18.05±0.01	17.62±0.02	17.28±0.01	17.61±0.03	-99±-99	14.64±0.17	$11.88^{+0.35}_{-0.29}$	$75.37^{+92.43}_{-36.29}$	$7.1^{+1.64}_{-2.01}$	$11.43^{+0.09}_{-0.09}$	NONE
GMBCG J131.94463+23.03120	131.944634932858	23.0311980313457	0.35±0.11	0.0	14	21.85±0.45	20.59±0.05	19.39±0.03	18.66±0.02	18.2±0.06	16.85±0.01	16.96±0.02	15.61±0.25	14.14±0.15	$11.97^{+0.44}_{-0.18}$	$92.47^{+162.15}_{-31.38}$	$7.5^{+1.08}_{-1.49}$	$11.42^{+0.07}_{-0.09}$	NONE
GMBCG J132.09946+43.80267	132.09945628613	43.8026657148125	0.16±0.01	0.152366	11	19.67±0.09	17.52±0	16.39±0.01	15.92±0	15.64±0.01	15.65±0	16.12±0.01	17.73±0.47	14.41±0.16	$10.77^{+0.43}_{-0.19}$	$5.82^{+9.73}_{-2.08}$	$5.51^{+0.66}_{-2.04}$	$11.41^{+0.05}_{-0.08}$	BPT
GMBCG J132.61454+52.27889	132.614538186751	52.2788861995261	0.41±0.05	0.0	11	22.03±0.34	21.22±0.06	19.7±0.03	19.04±0.02	18.62±0.05	17.3±0.01	16.61±0.01	15.27±0.04	14.29±0.12	$12.4^{+0.24}_{-0.38}$	$252.29^{+189.69}_{-146.61}$	$6.51^{+1.57}_{-1.99}$	$11.45^{+0.08}_{-0.12}$	WISE
GMBCG J132.96057+39.82724	132.960567769331	39.8272393226648	0.35±0.03	0.345035	22	21.58±0.53	19.73±0.03	18.06±0.02	17.42±0.01	17.07±0.02	16.38±0.01	16.93±0.03	16.06±0.13	14.61±0.21	$11.72^{+0.42}_{-0.19}$	$53.04^{+88.02}_{-18.62}$	$6.41^{+1.84}_{-2.44}$	$11.7^{+0.09}_{-0.1}$	NONE
GMBCG J133.31805+41.40923	133.318053383366	41.4092349195037	0.17±0.03	0.133226	10	19.17±0.04	18.02±0	17.22±0.01	16.75±0	16.56±0.01	16.52±0.01	16.86±0.02	15.58±0.06	14.36±0.14	$11.11^{+0.27}_{-0.38}$	$12.76^{+11.12}_{-7.42}$	$5.75^{+1.11}_{-2.67}$	$10.94^{+0.08}_{-0.15}$	BPT
GMBCG J133.71068+62.31389	133.710675780926	62.3138892763371	0.29±0.05	0.0	11	19.09±0.04	18.65±0.01	17.99±0.01	17.62±0.01	17.31±0.01	16.19±0	15.95±0	15.31±0.04	14.64±0.13	$12.2^{+0.07}_{-0.26}$	$157.36^{+27.35}_{-70.04}$	$0.96^{+0.12}_{-0.1}$	$10.74^{+0.05}_{-0.04}$	WISE
GMBCG J134.10410+04.16905	134.104103659888	4.16905462271393	0.28±0.03	0.0	10	23.72±2.36	20.13±0.03	18.66±0.02	18.07±0.01	17.66±0.03	17.34±0.02	17.78±0.04	18.58±1.26	14.58±0.2	$11.1^{+0.43}_{-0.18}$	$12.7^{+21.39}_{-4.24}$	$7.4^{+1.37}_{-1.95}$	$11.31^{+0.08}_{-0.09}$	NONE
GMBCG J134.81077+14.43933	134.810766758989	14.4393323466222	0.41±0.06	0.0	10	22.86±0.67	21.75±0.09	20.22±0.04	19.48±0.03	19.06±0.07	18.03±0.02	18.07±0.05	15.87±0.08	14.47±0.14	$12.01^{+0.41}_{-0.18}$	$103.35^{+164.57}_{-35.13}$	$6.77^{+1.41}_{-2.81}$	$11.2^{+0.09}_{-0.1}$	NONE
GMBCG J135.66011+17.63098	135.660109294574	17.6309768188307	0.2±0.02	0.164037	8	19.3±0.06	17.9±0.01	16.88±0.01	16.37±0.01	16.09±0.01	15.6±0	15.63±0.01	15.05±0.06	14.03±0.13	$11.48^{+0.27}_{-0.39}$	$30.28^{+26.29}_{-18.08}$	$4.02^{+2.45}_{-1.54}$	$11.33^{+0.1}_{-0.07}$	BPT
GMBCG J135.73803+27.02423	135.738026696358	27.0242347317556	0.42±0.03	0.0	30	21.38±0.45	20.7±0.07	19.07±0.03	18.34±0.02	17.93±0.05	16.59±0.01	16.54±0.02	15.52±0.07	14.66±0.19	$12.29^{+0.27}_{-0.35}$	$192.97^{+163.23}_{-107.31}$	$6.66^{+1.53}_{-2.81}$	$11.76^{+0.09}_{-0.1}$	NONE
GMBCG J136.04140+34.22219	136.041396626264	34.2221866685943	0.48±0.09	0.0	15	21.73±0.39	21.11±0.09	19.93±0.05	19.19±0.04	18.81±0.09	17.73±0.02	17.87±0.04	15.74±0.08	14.75±0.22	$12.37^{+0.27}_{-0.33}$	$232.92^{+195.93}_{-123.7}$	$5.86^{+1.78}_{-2.49}$	$11.3^{+0.1}_{-0.12}$	NONE
GMBCG J136.13329+57.30211	136.133290986086	57.3021123351345	0.28±0.03	0.0	8	19.49±0.05	18.8±0.01	17.97±0.01	17.57±0.01	17.2±0.02	16.77±0.01	16.82±0.01	15.27±0.04	14.94±0.21	$12.12^{+0.08}_{-0.44}$	$133.08^{+26.81}_{-84.79}$	$2.85^{+1.14}_{-0.54}$	$10.9^{+0.09}_{-0.05}$	NONE
GMBCG J137.17288+61.00169	137.172881824142	61.0016911370256	0.35±0.05	0.0	12	20.46±0.11	19.89±0.02	18.87±0.02	18.39±0.01	17.91±0.04	16.42±0	16.12±0.01	15.62±0.05	14.39±0.11	$12.07^{+0.28}_{-0.35}$	$117.95^{+106.28}_{-64.74}$	$6.39^{+1.46}_{-1.35}$	$11.21^{+0.08}_{-0.08}$	WISE
GMBCG J137.23314+31.16090	137.233141058342	31.1608957019611	0.31±0.02	0.313533	16	22.6±0.78	20.03±0.04	18.47±0.01	17.84±0.01	17.54±0.03	17.03±0.01	17.48±0.04	19.63±3.29	14.41±0.17	$11.22^{+0.42}_{-0.17}$	$16.63^{+27.15}_{-5.51}$	$6.86^{+1.83}_{-2.3}$	$11.39^{+0.07}_{-0.09}$	NONE
GMBCG J137.45253+10.94288	137.452534451653	10.9428802941904	0.16±0.03	0.164306	19	18.73±0.09	17.32±0.01	16.41±0.01	15.98±0.01	15.81±0.02	15.72±0.01	15.85±0.01	14.79±0.06	13.96±0.14	$11.6^{+0.25}_{-0.4}$	$39.98^{+31.57}_{-24.18}$	$3.77^{+3.14}_{-2.53}$	$11.22^{+0.13}_{-0.12}$	BPT
GMBCG J137.63596+41.04753	137.635964116445	41.0475327184696	0.48±0.08	0.0	20	21.35±0.22	20.48±0.03	19.22±0.02	18.48±0.01	18.06±0.03	16.83±0.01	16.52±0.01	15.65±0.07	14.76±0.18	$12.36^{+0.25}_{-0.35}$	$229.77^{+179.2}_{-125.97}$	$6.04^{+1.61}_{-1.92}$	$11.7^{+0.06}_{-0.1}$	WISE
GMBCG J137.99779+59.50252	137.997790001713	59.5025206498211	0.23±0.04	0.0	9	17.69±0.01	17.43±0.01	16.68±0.01	16.15±0	15.93±0.01	15.45±0	15.53±0.01	14.6±0.03	13.9±0.1	$12.21^{+0.07}_{-0.27}$	$162.07^{+29.05}_{-74.89}$	10	11.58	NONE
GMBCG J138.72789+05.55243	138.727889276118	5.55242909843523	0.18±0.03	0.195994	17	18.63±0.05	17.59±0.01	16.89±0.01	16.5±0	16.31±0.02	16.27±0.01	16.56±0.02	14.61±0.03	14.38±0.14	$12.05^{+0.06}_{-0.21}$	$112.43^{+17.34}_{-42.51}$	$3.82^{+4.22}_{-1.53}$	$10.88^{+0.11}_{-0.1}$	NONE
GMBCG J139.21642+52.64121	139.21641628926	52.6412142213301	0.27±0.06	0.190389	16	18.39±0.02	17.57±0	16.68±0.01	16.32±0	15.98±0.01	15.84±0	15.92±0.01	16.17±0.1	14.53±0.15	$11.06^{+0.45}_{-0.18}$	$11.57^{+21.27}_{-3.94}$	$6.59^{+2.2}_{-1.88}$	$11.41^{+0.06}_{-0.06}$	BPT
GMBCG J140.28593+45.64928	140.285925333149	45.649278453841	0.21±0.03	0.174485	8	19.11±0.05	17.82±0	16.69±0.01	16.22±0	15.95±0.01	15.15±0	14.94±0	14.19±0.02	13.27±0.06	$12.13^{+0.06}_{-0.25}$	$135.86^{+20.02}_{-60.16}$	$7.88^{+0.73}_{-0.67}$	$11.6^{+0.04}_{-0.04}$	WISE
GMBCG J140.82888+29.76941	140.828877469209	29.7694076793216	0.39±0.07	0.0	11	20.69±0.17	20.12±0.04	19.48±0.03	18.99±0.03	18.25±0.04	17.93±0.02	18.14±0.06	16±0.1	14.52±0.2	$11.92^{+0.41}_{-0.19}$	$82.28^{+129.07}_{-29.02}$	$5.64^{+1.93}_{-3.29}$	$10.88^{+0.11}_{-0.16}$	NONE
GMBCG J141.59072+62.46469	141.590718896807	62.4646931596678	0.11±0.02	0.12634	9	18.93±0.07	17.32±0.01	16.45±0	16.04±0	15.75±0.01	15.78±0	16.23±0.01	15.4±0.05	14.95±0.21	$10.96^{+0.27}_{-0.4}$	$9.19^{+7.95}_{-5.49}$	$4.34^{+2.57}_{-0.6}$	$10.99^{+0.09}_{-0.06}$	BPT
GMBCG J143.35190+06.97592	143.351897556082	6.9759245772116	0.19±0.02	0.0	8	20.08±0.12	18.74±0.02	17.75±0.01	17.25±0.01	16.92±0.03	16.68±0.01	16.91±0.02	15.12±0.05	14.08±0.12	$11.68^{+0.24}_{-0.42}$	$48.26^{+36.23}_{-30.03}$	$6.47^{+2.69}_{-2.52}$	$10.99^{+0.13}_{-0.14}$	NONE
GMBCG J145.91519+08.93535	145.91518899381	8.93534998424573	0.1±0.03	0.103973	11	18.06±0.03	16.87±0.01	16.23±0	15.86±0	15.59±0.01	15.67±0	16.12±0.01	14.17±0.02	13.91±0.11	$10.93^{+0.59}_{-0.06}$	$8.52^{+24.81}_{-1.12}$	$4.02^{+0.65}_{-1.07}$	$10.51^{+0.09}_{-0.05}$	NONE
GMBCG J145.99552+04.28192	145.995520564657	4.28191745024208	0.29±0.09	0.0	10	19.91±0.2	19.13±0.02	18.01±0.02	17.57±0.01	17.25±0.05	16.65±0.01	16.81±0.02	15.62±0.08	14.54±0.19	$11.88^{+0.27}_{-0.37}$	$75.11^{+66.11}_{-42.97}$	$5.6^{+2.09}_{-2.32}$	$11.31^{+0.09}_{-0.11}$	NONE
GMBCG J147.22126+27.98813	147.221264746376	27.9881295516909	0.41±0.09	0.0	16	21.68±0.29	20.95±0.07	19.69±0.03	19.08±0.03	18.74±0.07	17.82±0.02	17.33±0.03	15.71±0.08	14.49±0.17	$12.21^{+0.26}_{-0.34}$	$163.08^{+136.56}_{-87.87}$	$6.06^{+1.85}_{-2.42}$	$11.2^{+0.09}_{-0.11}$	WISE
GMBCG J148.38032+22.74570	148.380320659692	22.7456989645336	0.17±0.02	0.20488	15	19.52±0.08	18.17±0.01	17.25±0.01	16.81±0.01	16.5±0.02	16.47±0.01	16.68±0.02	15.02±0.05	14.56±0.18	$11.91^{+0.08}_{-0.49}$	$80.91^{+17.02}_{-54.94}$	$4.98^{+2.85}_{-2.68}$	$11.14^{+0.09}_{-0.14}$	BPT
GMBCG J149.74544+21.13741	149.745443703615	21.1374109487258	0.29±0.03	0.0	17	19.55±0.07	18.95±0.01	18.21±0.01	17.88±0.01	17.51±0.04	17.29±0.01	17.42±0.03	15.65±0.07	13.79±0.08	$11.66^{+0.28}_{-0.15}$	$45.98^{+41.68}_{-13.77}$	$1.07^{+1.61}_{-0.21}$	$10.68^{+0.09}_{-0.07}$	NONE
GMBCG J151.66740+21.67074	151.66739864	21.67074124	0.19±0.01	0.189074	19	19.62±0.16	17.46±0.01	16.21±0	15.7±0	15.34±0.01	15.19±0	15.43±0.01	15.82±0.16	14.06±0.18	$11.22^{+0.45}_{-0.18}$	$16.63^{+30.61}_{-5.69}$	$5.01^{+2.37}_{-0.69}$	$11.62^{+0.06}_{-0.06}$	BPT
GMBCG J151.86216+29.50568	151.86215965	29.50568309	0.15±0.03	0.116862	15	19.18±0.07	17.55±0.01	16.61±0	16.12±0	15.85±0.01	15.79±0.01	16.11±0.01	15.73±0.12	13.92±0.15	$10.78^{+0.43}_{-0.19}$	$6.05^{+10.13}_{-2.17}$	$4.18^{+4.03}_{-0.45}$	$10.68^{+0.43}_{-0.05}$	NONE
GMBCG J151.96927+27.50322	151.9692698	27.50322434	0.15±0.02	0.148337	9	18.31±0.03	16.97±0	16.12±0	15.71±0	15.42±0.01	15.39±0	15.74±0.01	14.27±0.02	14.1±0.12	$11.79^{+0.07}_{-0.48}$	$61.01^{+10.79}_{-40.71}$	$3.49^{+4.02}_{-0.48}$	$11.19^{+0.05}_{-0.05}$	NONE
GMBCG J152.05418+12.99533	152.05418172	12.99532823	0.47±0.02	0.0	8	22.52±0.98	21.04±0.09	19.44±0.03	18.59±0.03	18.19±0.08	17±0.01	17.46±0.04	17.17±0.34	14.4±0.15	$11.9^{+0.4}_{-0.16}$	$79.51^{+120.16}_{-24.87}$	$6.15^{+1.58}_{-2.52}$	$11.65^{+0.08}_{-0.14}$	NONE
GMBCG J152.23915+56.43633	152.23914718	56.43632872	0.27±0.07	0.0	21	21.24±0.21	20.09±0.03	18.86±0.02	18.29±0.02	17.87±0.03	17.46±0.01	17.72±0.03	16.53±0.13	14.91±0.2	$11.31^{+0.44}_{-0.18}$	$20.27^{+35.15}_{-6.95}$	$7.08^{+1.87}_{-2.05}$	$11.05^{+0.1}_{-0.1}$	NONE
GMBCG J153.24029+17.50484	153.24028518	17.50484024	0.12±0.02	0.115981	9	18.55±0.06	16.77±0.01	15.81±0	15.37±0	15.03±0.01	15.16±0	15.66±0.01	14.84±0.05	14.39±0.19	$11.05^{+0.28}_{-0.38}$	$11.35^{+10.09}_{-6.56}$	$7.64^{+1.15}_{-1.05}$	$11.11^{+0.05}_{-0.05}$	BPT
GMBCG J153.57351+47.87017	153.57351363	47.87017286	0.29±0.04	0.0	11	19.03±0.04	18.38±0.01	17.5±0.01	17.17±0.01	16.85±0.02	16.75±0.01	16.87±0.02	15.1±0.04	14.86±0.19	$12.26^{+0.05}_{-0.24}$	$183.23^{+21.7}_{-78.06}$	$4.32^{+2.19}_{-2.08}$	$11.15^{+0.12}_{-0.12}$	NONE
GMBCG J154.11671+46.51435	154.11671456	46.51435331	0.15±0.04	0.0	8	17.56±0.01	17.04±0	16.5±0	16.09±0	15.91±0.01	15.43±0	15.35±0	14.42±0.03	14.02±0.11	$11.82^{+0.06}_{-0.27}$	$66.74^{+10.26}_{-30.75}$	8	11.02	NONE
GMBCG J154.28803+39.96277	154.2880316	39.96276587	0.24±0.03	0.0	12	21.16±0.16	19.87±0.02	18.68±0.01	18.21±0.01	17.87±0.02	17.57±0.02	17.82±0.04	16.72±0.17	14.77±0.18	$11.13^{+0.44}_{-0.18}$	$13.4^{+23.37}_{-4.53}$	$7.14^{+2.02}_{-3.22}$	$10.93^{+0.14}_{-0.14}$	NONE

† As quoted from the GMBCG catalog
Note: All photometry is in AB magnitude.

Circum-galactic medium in the halo of quasars

Ottolina R. [1,*], **Falomo R.** [2], **Treves A.** [1], **Uslenghi M.** [3], **Kotilainen J.K.** [4], **Scarpa R.** [5] **and Farina E.P.** [6]

[1] *DISAT-Università degli Studi dell'Insubria, Como, Italy*
[2] *INAF-Osservatorio astronomico di Padova, Italy*
[3] *INAF/IASF -Milano, Italy*
[4] *Finnish Centre for Astronomy with ESO (FINCA), Finland*
[5] *Istituto de astrofisica de Canarias, Spain*
[6] *Max-Planck-Institut für Astronomie, Heidelberg, Germany*

Correspondence*:
Via Valleggio 11, COMO 22100 ITALY
r.ottolina@uninsubria.it

ABSTRACT

The properties of circum-galactic gas in the halo of quasar host galaxies are investigated analyzing Mg II 2800 and C IV 1540 absorption-line systems along the line of sight close to quasars. We used optical spectroscopy of closely aligned pairs of quasars (projected distance $\leq$ 200 kpc, but at very different redshift) obtained at the VLT and Gran Telescopio Canarias to investigate the distribution of the absorbing gas for a sample of quasars at z$\sim$1. Absorption systems of EW $\geq$ 0.3 Å associated with the foreground quasars are revealed up to 200 kpc from the centre of the host galaxy, showing that the structure of the absorbing gas is patchy with a covering fraction quickly decreasing beyond 100 kpc. In this contribution we use optical and near-IR images obtained at VLT to investigate the relations between the properties of the circum-galactic medium of the host galaxies and of the large scale galaxy environments of the foreground quasars.

Keywords: quasar, quasar environment, quasar pair, quasar spectra, galaxy around quasar

1 INTRODUCTION

The standard model for the origin of the extreme luminosity of quasars considers that a supermassive black hole shines as a quasar when intense mass inflow takes place, possibly as a consequence of tidal forces in dissipative events (e.g., [1]). In this scenario, the circum-galactic medium of quasar host galaxies is expected to be populated by streams, cool gas clouds and tidal debris, as commonly observed in interacting galaxies (e.g. [2],[3]). Moreover the gas of the circum-galactic medium could be metal enriched by supernova-driven winds triggered by starbursts events associated to the mergers or by quasar-driven outflows of gas (e.g., [4], [5]).

One of the effective ways to study the circum-galactic medium of galaxies at high redshift is to investigate the absorption features that they imprint in the spectra of quasars. In particular, projected quasar pairs (figure 1 left) are ideal observational tools for this purpose, since the light of the very bright source in the background ($z \equiv z_B$) goes through the extended halo of the foreground ($z \equiv z_F < z_B$) object (e.g. [6], [7]).

This can be evidenced by absorption lines at the foreground redshift: an example is reported in figure 1 right.

In our previous works we studied 49 quasar pairs ([7],[8],[9]). We used the optical spectroscopy of close pairs (projected distance $\leq$ 200 kpc) obtained at the ESO-VLT and Gran Telescopio Canarias (GTC) to investigate the distribution of the absorbing gas at 100-200 kpc projected distance from the quasar studying the presence of Mg II or C IV absorption lines at the redshift of foreground quasar. In order to characterize the structure of circum-galactic medium of the foreground quasar host galaxy we estimated the covering fraction of Mg II or C IV as a function of the projected distance. We assumed a threshold in equivalent width of 0.3 Å, then we subdivided the projected distance in bins. For each bin we computed the covering fraction as the ratio between the number of systems with Mg II or C IV absorption lines greater than the threshold and the total number of observed systems. Our previous results ([7],[8],[9]) indicate that 22 spectra exhibit absorption lines of foreground quasar in the background quasar: 15 Mg II and 7 C IV. We found that the detected Mg II absorption systems of EW $>$ 0.3 Å associated with the foreground quasars are revealed up to $\sim$200 kpc from the centre of the host galaxy. The structure of absorbing gas is patchy with covering fraction of the gas that quickly decreases beyond 100 kpc. This is illustrated in figure 2 left. A similar behavior is present in absorption systems with C IV doublet (figure 2 right).

In this paper we analyze optical and NIR images of foreground quasars in order to investigated their closed environments and their host galaxies.

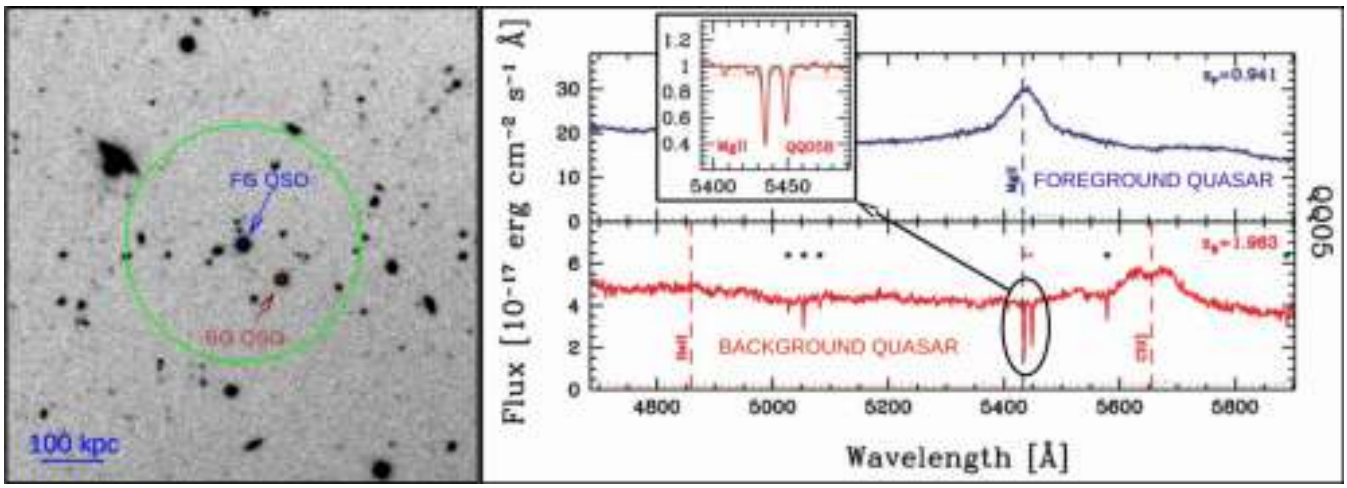

Figure 1. Image of projected quasar pair Q0059-2702. Blue and red arrows indicate the foreground quasar and the background one. Green circle shows the projected distance of 200 kpc from the foreground quasar. *Right*: VLT spectra of quasar pair Q0059-2702. The blue and red solid lines refer to foreground quasar and background quasar, respectively. The insert shows the zoom of Mg II absorptions at the same redshift of foreground quasar.

2 SAMPLE AND OBSERVATIONS

The selection procedure of our quasar pair projected sample is reported in detail in [7] and [8]. Here we summarize briefly the main criteria of our choice: i) visibility from telescope location; ii) foreground quasar redshift must be selected in order that Mg II doublet falls in GRISM wavelength range; iii) projected distance at foreground redshift $\leq$ 200 kpc; iv) line-of-sight velocity difference $\geq$ 5000 km s^{-1} to avoid

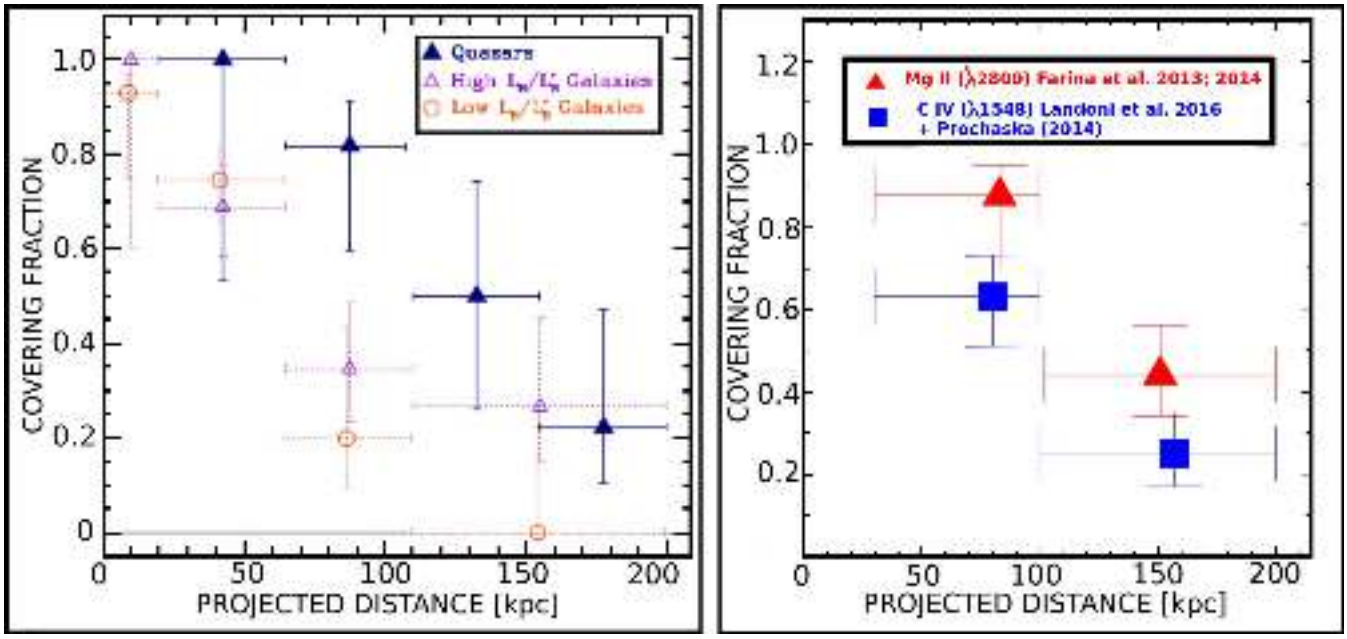

Figure 2. Comparison between quasars [8] and galaxies [10] of covering fraction of transversal absorption system of Mg II as a function of the projected distance. *Right*: Comparison of covering fraction of quasar halo for Mg II (red triangles) and C IV (blue squares) absorption lines. The covering fraction of Mg II is systematically higher than that of C IV.

physical pairs; v) background quasar must be brighter than $m_V \sim 21$ to ensure good spectra signal-to-noise ratio.

We acquired optical images at FORS2@VLT with the I BESS filter for the object with z$\leq$1 and the Z GUNN filter otherwise, and near-IR images at HAWK-I@VLT with H filter for a total of 24 quasar projected pairs (4 targets have only optical images, 8 ones have only NIR images and 12 objects have images in both bands.). With this configuration we explore galaxies at the redshift of the target in the B band in the rest frame. For a subsample of object reported in table 1 we present here 8 deep high quality I-band images (seeing $\sim$0.5 arcsec).

QSO_B (1)	z_B (2)	QSO_F (3)	z_F (4)	pd [kpc] (5)	Mg II (6)	ovdens (7)
J003823.6-291259	2.699	J003823.74-291311.8	0.793	91	no	no
LQAC 015-026 011	1.963	J010204.12-264600.0	0.941	84	yes	no
J013500.09-004113.4	1.259	J013458.77-004129.0	1.003	176	yes	yes
J014630.95+001531.6	1.019	J014630.14+001521.3	0.923	125	yes	yes
J021553.71+010953.9	2.215	J021552.53+011000.1	0.875	145	no	yes
J022158.83-001052.5	3.213	J022158.77-001044.3	1.036	66	yes	yes
[HB89] 2225-403	2.398	J222850.49-400825.7	0.931	78	yes	no
J225902.37+003221.7	1.456	J225902.87+003243.7	0.868	183	no	no

Table 1. List of targets observed in I band. Column (1) and (3) give the name of background and foreground quasars respectively while (2) and (4) give their redshifts. Column (5) reports the projected distances at the redshift of the foreground quasar. Column (6) and (7) are labels for the presence of Mg II absorption lines and of an overdensity of galaxies around the foreground quasar.

3 ANALYSIS

We performed the analysis of optical images in order to characterize the close environment of foreground quasar. We used the software SEXTRACTOR [11] to identify all objects in the frame over a given magnitude limit and to distinguish galaxy-like objects from star-like ones (galaxies have CLASS_STAR < 0.5 and stars have CLASS_STAR > 0.5). Then we evaluated the overdensity of galaxies around the foreground quasar calculating the ratio of number of galaxies per arcminute square to background estimated at distances greater than 500 kpc.

The near-IR images have been analyzed using the software package AIDA (Astronomical Image Decomposition Analysis, [12]). From this analysis of the near-IR images we are able to characterize the properties of the foreground quasars host galaxy via 2-d model fitting, assuming that they are the result of the superposition of two components: the nucleus, described by the local PSF, and the host galaxy, modeled by a Sersic function convolved with the proper PSF.

4 PRELIMINARY RESULTS

Based on our deep optical images of quasars we are able to characterize the galaxy environment up to I$\sim$ 23.5 which is more than 2 magnitudes deeper than SDSS images (see figure 3 left). This allows to investigate the galaxy environment down to about 3 magnitude fainter than M*. We find that for 4 cases there is a clear galaxy overdensity around the foreground quasar while in the another 4 cases there is no evidence that quasars live in a group of galaxies (see figure 3 and table 1). In 3 quasars that exhibit overdensity there is also a detection of Mg II absorption systems at the same redshift of foreground quasar in the circum-galactic medium. In the cases of no galaxy overdensity Mg II absorption lines are detected in 2 objects. The small sample, investigated till now, does not permit us to draw firm conclusions on the relationship between galaxy environments and presence of cold gas in the intergalactic medium. We are completing the analysis of the full sample and extending it with other targets from ongoing observations at GTC.

Till now we analyzed 11 out of the 20 foreground quasars with NIR images. For 9 ($\sim$ 80%) the host galaxy is well resolved. In one case the detection of the host galaxy is marginal and only for one image no evidence of the host galaxy is found. The rest frame absolute magnitude in I band of the resolved host galaxies ranges from -22.5 to -24.9, with a median value of -23.7. These results are comparable to those reference to other quasars at similar redshift [13].

5 ACKNOWLEDGMENT

EPF acknowledge funding through the ERC grant ‘Cosmic Dawn’.

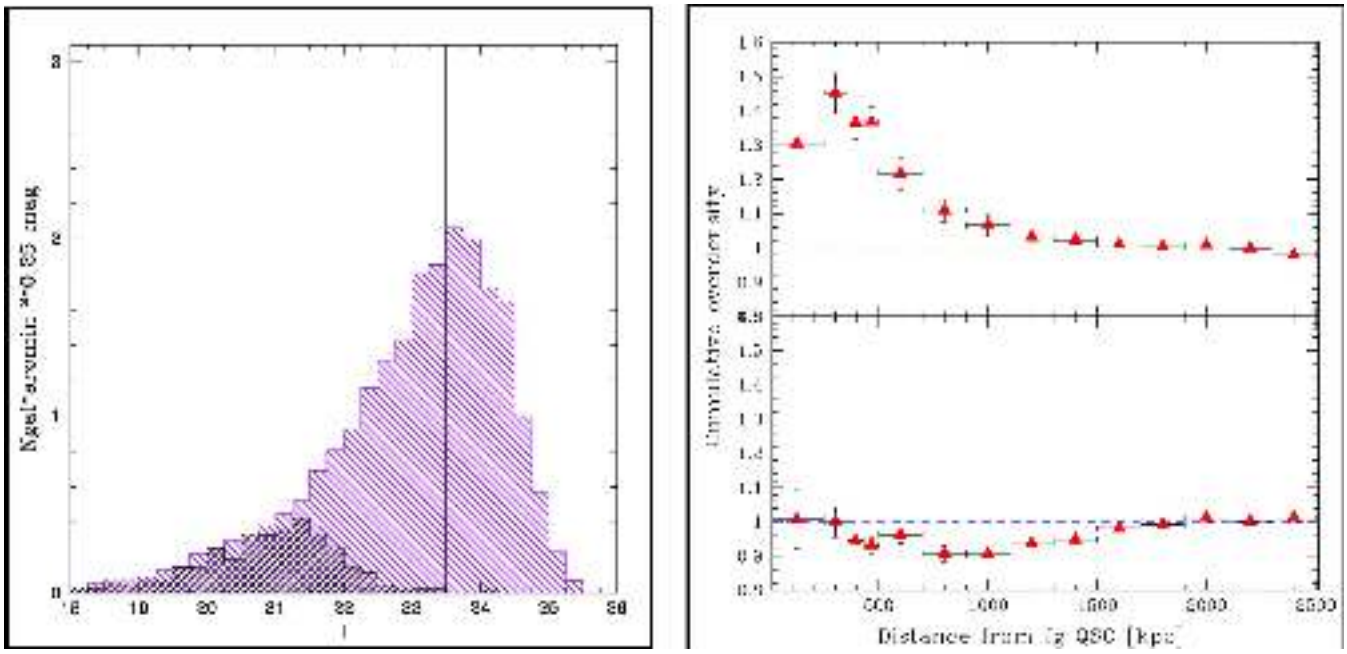

Figure 3. *Left*: Average surface number density of galaxies vs I magnitude of 8 quasar pair fields obtained at VLT FORS2. The vertical line marks the adopted threshold magnitude for the environment study. For comparison the black histogram shows the similar distribution based on the SDSS analysis of 5 fields. *Right*: Average cumulative overdensity of galaxies around quasars (see table 1). Only half of quasars exhibits a clear galaxy overdensity (upper panel) while the other half does not show any overdensity (lower panel).

REFERENCES

[1] Di Matteo T, Springel V, Hernquist L. Energy input from quasars regulates the growth and activity of black holes and their host galaxies. *Nature* **433** (2005) 604–607. doi:10.1038/nature03335.

[2] Sulentic JW, Rosado M, Dultzin-Hacyan D, Verdes-Montenegro L, Trinchieri G, Xu C, et al. A Multiwavelength Study of Stephan's Quintet. *AJ* **122** (2001) 2993–3016. doi:10.1086/324455.

[3] Cortese L, Gavazzi G, Boselli A, Franzetti P, Kennicutt RC, O'Neil K, et al. Witnessing galaxy preprocessing in the local Universe: the case of a star-bursting group falling into Abell 1367. *A&A* **453** (2006) 847–861. doi:10.1051/0004-6361:20064873.

[4] Steidel CC, Erb DK, Shapley AE, Pettini M, Reddy N, Bogosavljević M, et al. The Structure and Kinematics of the Circumgalactic Medium from Far-ultraviolet Spectra of z ˜= 2-3 Galaxies. *ApJ* **717** (2010) 289–322. doi:10.1088/0004-637X/717/1/289.

[5] Shen Y, Ménard B. On the Link between Associated Mg II Absorbers and Star Formation in Quasar Hosts. *ApJ* **748** (2012) 131. doi:10.1088/0004-637X/748/2/131.

[6] Hennawi JF, Prochaska JX, Burles S, Strauss MA, Richards GT, Schlegel DJ, et al. Quasars Probing Quasars. I. Optically Thick Absorbers near Luminous Quasars. *ApJ* **651** (2006) 61–83. doi:10.1086/507069.

[7] Farina EP, Falomo R, Decarli R, Treves A, Kotilainen JK. On the cool gaseous haloes of quasars. *MNRAS* **429** (2013) 1267–1277. doi:10.1093/mnras/sts410.

[8] Farina EP, Falomo R, Scarpa R, Decarli R, Treves A, Kotilainen JK. The extent of the Mg II absorbing circumgalactic medium of quasars. *MNRAS* **441** (2014) 886–899. doi:10.1093/mnras/stu585.

[9] Landoni M, Falomo R, Treves A, Scarpa R, Farina EP. Circumgalactic medium of quasars: C IV absorption systems. *MNRAS* **457** (2016) 267–271. doi:10.1093/mnras/stv2964.

[10] Nielsen NM, Churchill CW, Kacprzak GG. MAGIICAT II. General Characteristics of the Mg II Absorbing Circumgalactic Medium. *ApJ* **776** (2013) 115. doi:10.1088/0004-637X/776/2/115.

[11] Bertin E, Arnouts S. SExtractor: Software for source extraction. *A&ASupp* **117** (1996) 393–404. doi:10.1051/aas:1996164.

[12] Uslenghi M, Falomo R. AIDA: Astronomical Image Decomposition and Analysis. Gesù VD, Lo Bosco G, Maccarone MC, editors, *Modelling and Simulation in Science* (2008), 313.

[13] Sanghvi J, Kotilainen JK, Falomo R, Decarli R, Karhunen K, Uslenghi M. The black hole-host galaxy relation for very low mass quasars. *MNRAS* **445** (2014) 1261–1268. doi:10.1093/mnras/stu1822.